MASTERARBEIT / MASTER'S THESIS

Titel der Masterarbeit / Title of the Master's Thesis

Coupled hydro-mechanical 2-D modelling of underground hydrogen storage in a carbonate aquifer at Hontomín, Spain - Effect of reservoir permeability type (constant versus strain-dependent) on storage capacity

verfasst von / submitted by

Pablo Pacios Prado

angestrebter akademischer Grad / in partial fulfilment of the requirements for the degree of

Master of Science (MSc)

Wien, 2021/ Vienna 2021

Studienkennzahl lt. Studienblatt / degree programme code as it appears on the student record sheet:	UA 066 815
Studienrichtung lt. Studienblatt / degree programme as it appears on the student record sheet:	Masterstudium Erdwissenschaften
Betreut von / Supervisor:	Univ.-Prof. Dr. Thilo Hofmann

Acknowledgment

I would like to thank Victor Vilarrasa and Juan Alcalde a lot for their detailed and warm-hearted support and guidance. Your great experiences and your joy to share it with me always helped me when I struggled with my work.

I would also like to give a special thanks to Prof. Dr. Thilo Hofmann that he willingly accepted to be my supervisor, although the main focus of this work is not settled in the field of hydrogeology. Your commitment to this work and your openness to new topics helped me to write my master thesis in a field I am very interested in.

I also want to thank Oscar Fernandez very much for his short but kind and comprehensive support with his great expertise.

Finally, I want to thank my beloved partner Sarah a lot. Thank you for your help and love during this time and also before. You always encouraged me when I felt down and showed a lot of understanding and patience when I needed it most. As I know that rocks are not your greatest passion, in return, I promise I will never talk about reservoirs again…
unless we are dancing to “Reservoir” from Metronomy ;)

Abstract

In order to mitigate climate change, different storage options for large amounts of energy from renewable energies will be needed in the near future. Underground hydrogen storage (UHS) of *green hydrogen* (H_2 produced renewable energy) is a promising option to accomplish this task. UHS has been, however, scarcely investigated in saline aquifers, although these structures are abundant and have large storage capacities. Therefore, this work investigates the effect of the permeability type (constant vs. strain-dependent) / reservoir type (porous vs. naturally fractured) on the storage capacity of an UHS in a carbonate saline aquifer. The storage capacity was assumed to be limited either by fault slip or caprock fracturing. Numerical modeling of two hydro-mechanical 2-D UHS scenarios were performed. Both models only differed in the permeability type (constant vs. strain-dependent) of the reservoir, representing a porous and a fractured reservoir, respectively. Their geometry and hydro-mechanical properties were inspired by the storage structure of the CO_2 storage pilot plant at *Hontomín (*Spain). A subsequent fault stability analysis was carried out for both models. Our results showed that the maximum stored amount of H_2 was limited by the risk of fault slip of the same fault in both models. The storage capacity of the porous reservoir (M2) was 46% higher than the fractured one (M1), as liquid pressure and, thus, fault instability tended to increase more in model M1. This was because the variable heterogeneous permeability distribution in model M1 worked as a semi barrier against spreading of liquid pressure increase during the UHS. However, liquid pressure and the accompanying fault instability were higher at far distant faults in model M2. On the other hand, these values were lower at far distant faults than at faults located closer to the injection well in both models. Therefore, it was concluded that the hydrogen storage capacity and the suitability of a porous reservoir tends to be higher than that of a fractured reservoir for an UHS. Just in rare cases the opposite could be possible, if all faults close to the injection well are stable during the UHS but a far distant fault is critically stressed. Though, the difference in storage capacity between both reservoir types is very site-specific and a range in which these difference lies could not be detected within this work. This could, however, be the target of future investigations.

Kurzfassung

Um den Klimawandel abzumildern werden in der nahen Zukunft verschiedene Speicheroptionen für eine große Menge von Energie, gewonnen aus erneuerbaren Energien, gebraucht werden. Unterirdische Wasserstoffspeicherung (UWS) von *grünem Wasserstoff* (H_2 produziert aus erneuerbarer Energie) scheint eine vielversprechende Option zu sein, um diese Aufgabe zu bewältigen. UWS ist jedoch in salzhaltigen Aquiferen kaum untersucht, obwohl diese Strukturen großräumig vorhanden sind und große Speicherkapazität besitzen. Daher untersucht diese Arbeit den Effekt von der Art der Permeabilität (konstant gegen dehnungsabhängig) / Art des Speichergesteins (porös gegen natürlich geklüftet) auf die Speicherkapazität einer UWS´s in einem karbonatischen salzhaltigen Aquifer. Es wurde davon ausgegangen, dass die Speicherkapazität entweder durch das Rutschen einer Störung oder durch das Aufbrechen der isolierenden Gesteinseinheit begrenzt ist. Hydromechanische 2-D Modellierungen zweier UWS Szenarien in einem karbonatigen Aquifer wurden durchgeführt. Beide Modellierungen unterschieden sich nur in der Art der Permeabilität des Speichergesteins (konstant gegen dehnungsabhängig). Ihre Geometrie und hydromechanischen Eigenschaften waren angelehnt an die Speicherstruktur der CO_2-Speicherpilotanlage bei *Hontomín* (Spanien). Eine anschließende Störungsstabilitätsanalyse wurde anhand beider Modellen durchgeführt. Unsere Ergebnisse haben gezeigt, dass die maximale Menge an speicherbaren H_2 durch das Risiko einer Rutschung der selben Störung in beiden Modellen begrenzt war. Die Speicherkapazität des porösen Speichergesteins (M2) war 46% höher, als die des geklüfteten Speichergesteins (M1), da der Flüssigkeitsdruck und somit die Instabilität an Störungen in dem Modell M1 tendenziell stärker zunahm. Dies lag daran, da die unstatische heterogene Permeabilitätsverteilung im Modell M1 als eine Halbbarriere gegen die Ausbreitung des Anstieges des Flüssigkeitsdrucks während der UWS wirkte. Flüssigkeitsdruck und die damit einhergehende Instabilität an Störungen waren jedoch an weit entfernten Störungen in dem Modell M2 höher. Diese Werte waren aber andererseits in beiden Modellen an weit entfernten Störungen niedriger als an Störungen, die näher an dem Injektionsbrunnen lagen. Deshalb wurde geschlussfolgert, dass die Speicherkapazität für Wasserstoff und die damit einhergehende Tauglichkeit für eine UWS eines porösen Speichergesteins dazu tendiert, höher zu sein als von einem geklüfteten Speichergestein. Nur in seltenen Fällen könnte dies andersherum sein, nämlich wenn alle Störungen in der Nähe des Injektionsbrunnens während der UWS stabil sind, aber eine weite entfernte Störung kritisch gespannt ist. Wie stark sich allerdings die Speicherkapazität zwischen beiden Speichergesteinstypen unterscheidet ist sehr standortspezifisch und ein Bereich, in dem diese Unterschiede liegen könnten, konnte und sollte mit dieser Arbeit nicht ermittelt werden. Dies könnte allerdings das Ziel zukünftiger Untersuchungen sein.

List of Figures

List of Tables

List of Abbreviations

CO_2 Carbon dioxide

GCS Geologic carbon dioxide storage

H_2 Hydrogen

M1 Model with fractured reservoir containing a strain-dependent permeability

M2 Model with porous reservoir containing a constant permeability

$M2_{low}$ Model with porous reservoir and same amount of stored H_2 as in M1

$M2_{high}$ Model with porous reservoir and maximum possible amount of H_2 stored

S_H Horizontal stress along in z-direction

S_h Horizontal stress in x-direction

S_v Vertical stress

UGS Underground gas storage

UHS Underground hydrogen storage

Contents

1 Introduction

Mitigating global warming might be the most important challenge of our time. Global rise in temperature and its negative consequences are already having a worldwide impact on ecosystems and livelihoods and will do so in the future even more (Allen et al., 2018). Anthropogenic emission of greenhouse gases, particularly CO_2, need to be reduced dramatically to mitigate global warming (Fawzy et al., 2020). Unfortunately, the efforts to combat global warming in an adequate way are not implemented extensively and fast enough. As declared by the Secretary-General of the United Nations, António Guterres, “Climate Change is moving faster than we are” (Allen et al., 2018).
This is a concerning situation considering as the Earth System may be close to a tipping point that could trigger an irreversible domino-like pathway towards significantly hotter conditions. That would result in a so-called Hothouse Earth pathway, where the impact on society would be immense and certainly disruptive. Although it is not clear where exactly those tipping points lie, it is suggested that the risk of triggering tipping cascades could be high at a 2°C temperature increase in comparison to pre-industrial conditions (Steffen et al., 2018). Though it is still possible to limit warming to 1.5°C, drastic actions are required to do so (Allen et al., 2018; Tollefson, 2018). To still achieve this objective a broad portfolio of mitigation techniques and strategies have to be applied worldwide and in an effective way (Allen et al., 2018; Steffen et al., 2018).

One critical factor that must be addressed to reach the ambitious decarbonization goals is the transition of the energy sector into low or even zero carbon emissions systems, with the use of sustainable and renewable energy sources. Fortunately, this energy system transition is in progress in many places and sectors around the world (Allen et al., 2018) as renewable energy generation had been rising sharply in the last decades (ourworldindata.org/renewable-energy). However, most of these renewable energy technologies have a major disadvantage related to their inherent seasonal variability (e.g. wind and solar intensity is fluctuating by nature, Crotognio et al., 2010) and geographical extent (e.g. hydropower requires important and limited water resources and it is also seasonally variable). This unsteadiness causes alternating periods of surplus (i. e. renewable energy production > energy demand) and deficit (i.e. energy demand > renewable energy production) (Heide et al., 2011). At times of deficit, the demanded energy is obtained partly via CO_2 emitting sources (Crotognio et al., 2010; European Commission 2013). At periods of renewable energy surplus, produced energy and potential energy that could be produced is generally lost. This imbalance of energy supply from renewable energies could be compensated by storing surplus energy at periods of excess and used later in times of demand (European Commission 2013; Heide et al., 2011). This workflow would enhance the effectiveness of renewable energies, decrease the emission of greenhouse gases and combat climate change. Though, long-term storage of large energy amounts is still a challenge (Crotognio et al., 2010)

A proposed technique is the conversion of surplus renewable electric energy to chemical energy and its temporary storage (Fig.1) (Sáinz-García, 2017). The conversion is done by running electrolysis with surplus renewable energy and thereby separating water into oxygen (O_2) and hydrogen (H_2) (Van Renssen, 2020). The resulting hydrogen fuel is a suitable energy vector, as it has a high energy density, and can be used in several ways like for re-electrification, methanation (Panfilov, 2016), fueling vehicles or used for industrial processes. Moreover, its production is free of greenhouse gases, for which reason it is called *green hydrogen* (Van Renssen, 2020).

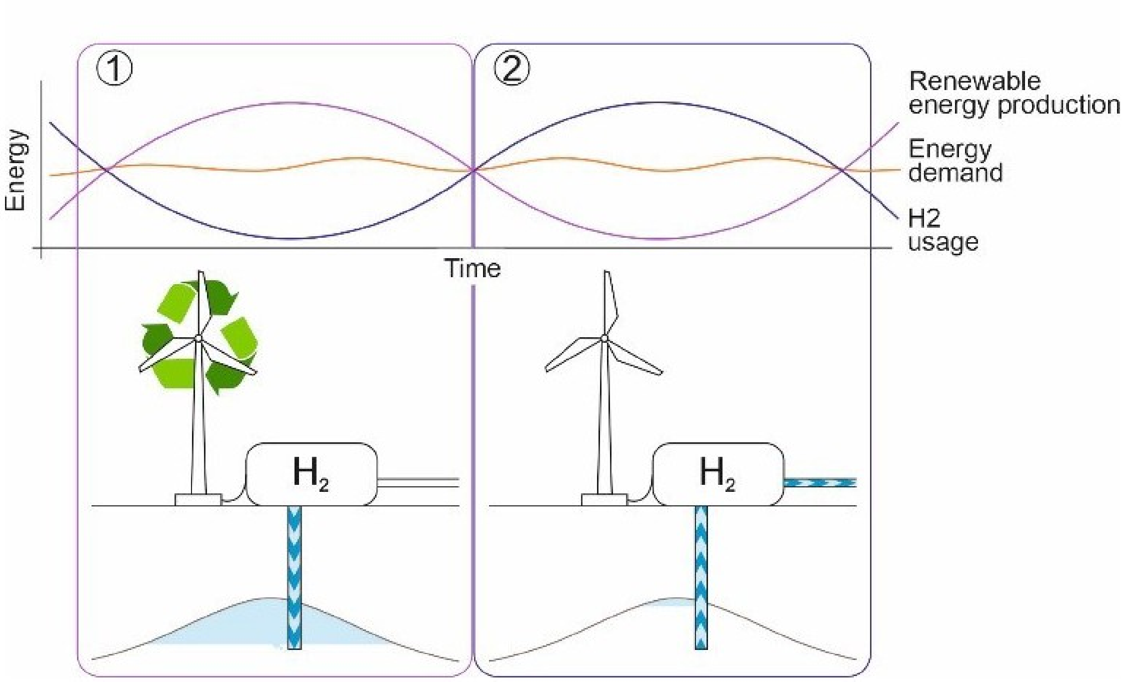

Fig. 1 Cycle of Green hydrogen production, storage (1) and use (2) in times of renewable energy excess (1) or deficit (2)*; Heinemann et al., 2021*

However, in order to stabilize the imbalance of renewable energy production at a large scale, large volume of hydrogen will need to be stored for renewable scarcity periods (Crotognio et al., 2010; Heide et al., 2011). Surface tanks are not suited to challenge this task as they have a very limited capacity and the investment costs are quite high for a large scale project (Andersson & Grönkvist, 2019). Underground hydrogen storage (UHS) instead (Fig.1), can provide a cheaper storage option for hydrogen, with a significantly lower footprint, high-security standards (Kruck et al., 2013) and is most likely the only option to store the required large amounts of hydrogen (Crotogino et al., 2010). Generally, there are three promising types of underground hydrogen storage sites that do have different characteristics: depleted oil- and gas fields, artificially diluted salt caverns and saline aquifers (Fig.2) (Kruck et al., 2013). Though salt caverns are the most employed UHS options, their geographical availability is limited (Panfilov, 2016; Kruck et al., 2013). In Europe, for example, potential large salt cavern fields are only present mainly in North Germany, Denmark, the Netherlands and Great Britain (Heide et al., 2011). However, if hydrogen is to be used broadly to decarbonize the energy system, alternative storage mediums have to be investigated. In particular, UHS in deep saline aquifers can be a suitable option as they are widespread (Allen et al., 2018; Tarkowski, 2019) and do offer more storage capacity than salt caverns (Panfilov, 2016). Furthermore, they are not needed for other benefits like agriculture or human consumption (Allen et al., 2018). Although storage in saline aquifers presents the highest costs of the three geologic storage options, they could present an alternative for storing sites where suited salt deposits and depleted oil- and gas fields are non-existent (Tarkowski, 2019).

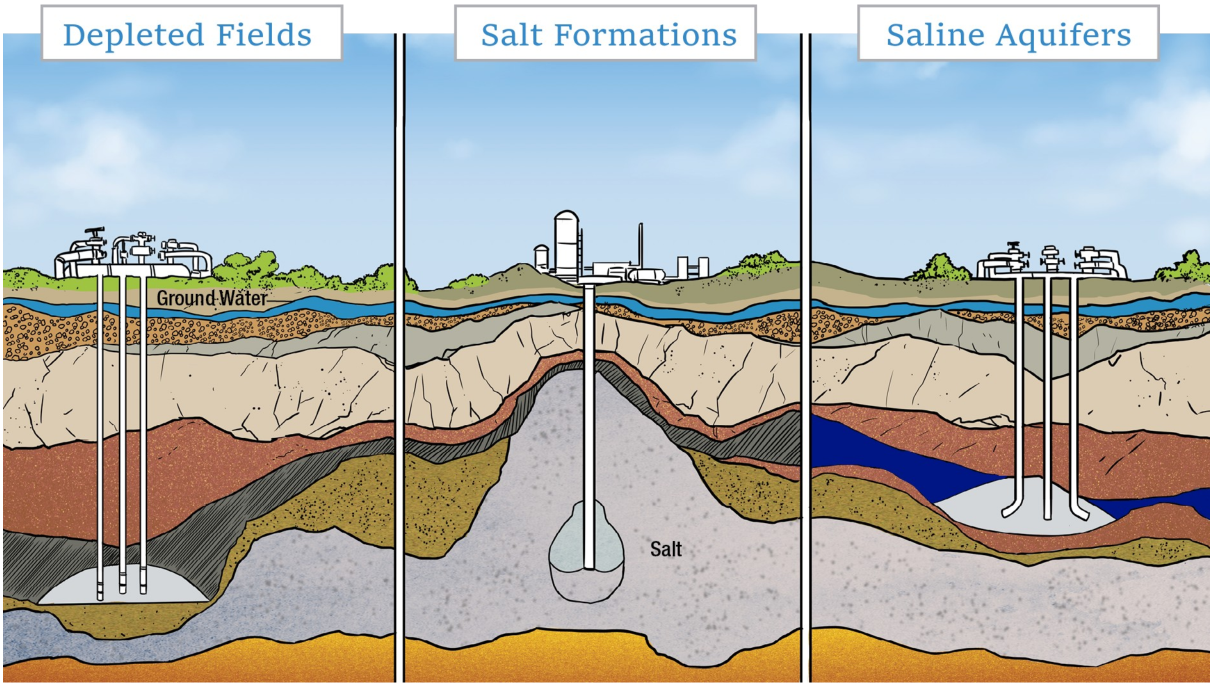

Fig. 2 Three different types of UHS: Depleted oil- and gas fields, artificially diluted salt caverns and saline aquifers; modified from danaenergy.com

2 State of Knowledge

2.1 Geological Structure & Injection Cycle for Underground Gas Storage

Since there is almost no experience with UHS in saline aquifers (Panfilov, 2016), underground gas storage (UGS) or geological CO_2 storage (GCS) can be used as analogues to try to understand the processes occurring during the cyclical or long term storage of hydrogen in the subsurface (Kruck et al., 2013; Sáinz-García et al., 2017; IEA, 2019). A suitable gas storage site in a deep saline aquifer consists of the water-containing reservoir formation with high porosity and permeability, and hence high storage capacity and injectivity, sealed by a high-entry pressure and low-permeable caprock formation/sealing unit on top (Bachu, 2000; Falzolgher & Altieri, 2005; Metz et al., 2005; ul Abedin 2015; Sunjay et al., 2019). In addition, a sealing base unit beneath the reservoir is also beneficial, as it protects pressure spreading to the critically stressed crystalline basement (Vilarrasa & Carrera 2015). Common reservoir rocks include sandstones or carbonate formations. Rock formations that can act as suitable seals include salt, shale or anhydrite (Kruck et al., 2013). To prevent gas migration out of the reservoir, the whole formation has to form a geological trap (preferably an anticline) that allows the accumulation of the fluids in the reservoir (Falzolgher & Altieri, 2005). A gas storage cycle consists of a gas injection, optionally a resting phase and finally a production of gas (Plaat 2009; Kruck et al., 2013).

During the injection phase, gas is injected into the reservoir's pore space by means of one or several wells. The water or brine inside of the aquifer's pore space is then pushed downwards laterally and the original fluid pressure in the reservoir will consequently increase (Kruck et al., 2013). This increase can be measured as the bottom hole pressure (BHP) at the injection well (de Dios et al., 2021). Due to the density contrast between gas and fluid, the gas accumulates beneath the highest sealing layer (Falzolgher & Altieri, 2005). The larger the reservoir and the higher its permeability, the lower the increase in pressure in the reservoir. Furthermore, an open aquifer accumulates less pressure than a compartmentalized one (Kruck et al., 2013; Bachu et al., 2015), as fluid pressure increases as it reaches a less permeable boundary (Vilarrasa et al., 2010). At a closed aquifer space for gas is created by compression of the rock and water (Bachu et al., 2015). Furthermore, if the permeability of the caprock is not too low, fluid flow of the water into the caprock can occur, leading to pressure dissipation. At the same time, the capillary entry pressure of the caprock hinders the gas flowing through this unit (Birkholzer, 2009). It is worth to mention that not all water will be displaced by the gas and some residual water may be trapped in microscopic structures (Carden & Paterson, 1979).

At the production phase, the stored gas is pumped out of the reservoir. As a result, pressure at the well drops and the higher pressure far away from the reservoir pushes back the gas into the well (Kruck et al., 2013). The extension of the gas plume declines at its outer boundary and the gas-water interface is upconing. It is important that the gas saturation of the plume is high enough to avoid extraction of water (Sáinz-García, 2017).

After the full recovery of the gas during the withdrawal operations, some gas still remains inside the reservoir and cannot be recovered (Kruck et al., 2013). Therefore, before storing the gas of interest (working gas), a cheaper gas (cushion gas) is injected to reduce the expense produced by the gas lost in these operations. The cushion gas may remain unrecoverable while the working gas can be extracted during a normal withdrawal phase (naturalgas.org). A further benefit of cushion gas is the maintenance of reasonable pressure and withdrawal rates (Lord 2009).

2.2 Uncertainties on Hydrogen Behaviour under Reservoir Conditions

Although knowledge and experience of UGS can be transferred to UHS, there exist some uncertainties about hydrogen flow in brine at reservoir conditions, arising from its high diffusivity and its low viscosity that results in high mobility (Fig.3). These properties make hydrogen a less convenient gas for displacing the resident fluid of the reservoir (Heinemann et al., 2021).

There are also some concerns about the high diffusivity of hydrogen. It could result in a higher risk of hydrogen leakage through the caprock. Yet, a saturated caprock should inhibit almost completely a leakage of hydrogen (Panfilov, 2016). An exemplary calculation of Carden & Paterson (1979) shows that hydrogen losses due to diffusion are around 2%. According to the more recent work of Amid et al. (2016), diffusion and leakage losses taken together could be even beneath 0.1%. The diffusion coefficient of hydrogen under reservoir conditions is still scarcely studied (Panfilov, 2016), but could be a dominant factor during a resting phase (Feldmann et al., 2016).

Hydrogen has a very low solubility in water even though at reservoir pressures ranging, for example, from 10-20 MPa, the molar fraction of hydrogen to water is around 0.1 to 0.2% (Ziparo et al., 2011). Therefore, anticipated losses of solved hydrogen in water should be very low. Carden & Paterson (1979) suggest a number of around 2% of hydrogen that could be lost in residual water, which could decline for every storage cycle.

Although it is beyond the scope of this work, it is worth mentioning that hydrogen can further get lost through biodegradation by microorganisms. This is especially the case for hydrogen storage in aquifers. It is not clear how large these losses are, they could range from low to very high and seem to depend much on the individual characteristics of each storage site (Panfilov, 2010; Kruck et al., 2013; Thaysen et al., 2020).

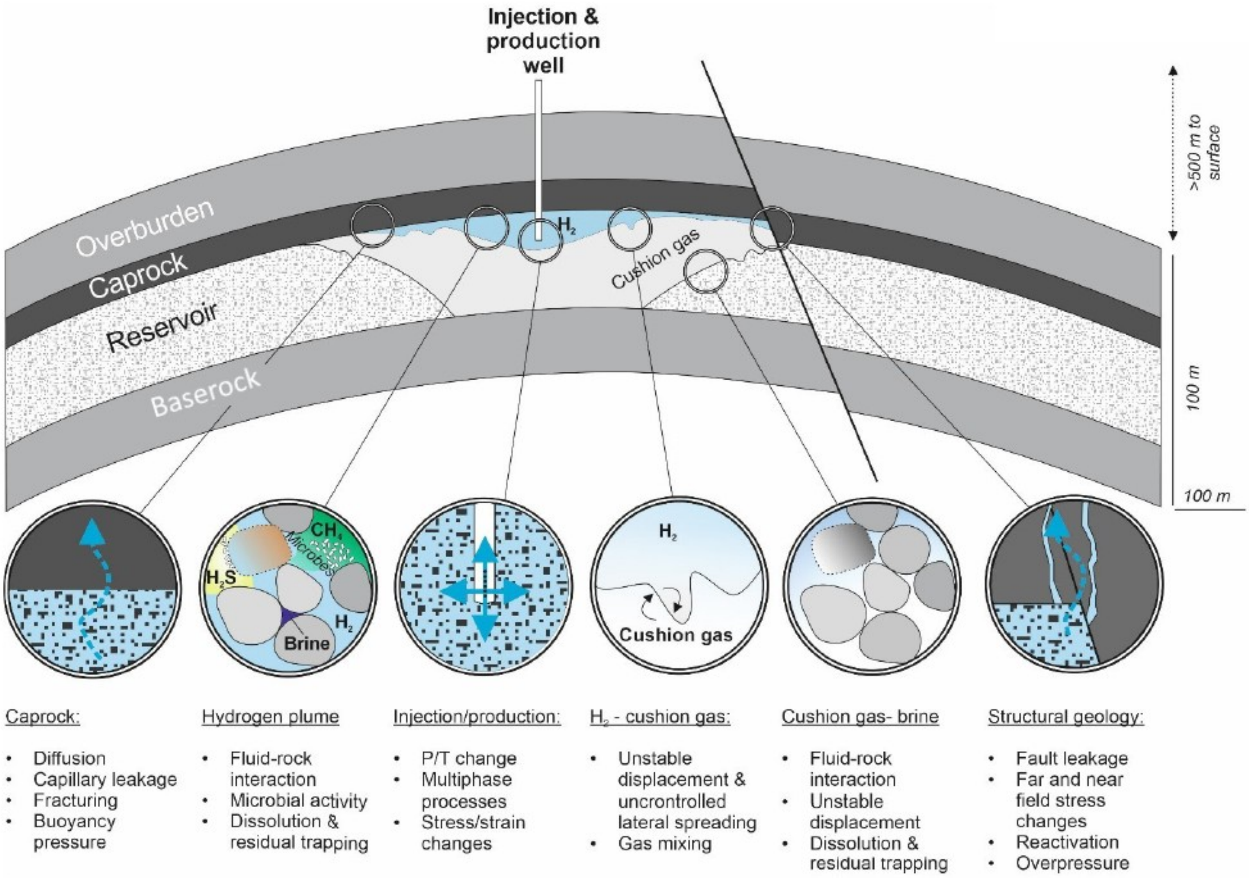

Fig. 3 Scheme of hydrogen storage in a reservoir located in an anticlinal structure; uncertainties about the behaviour of hydrogen in such a reservoir are listed below; the horizontal and vertical dimensions of the storage structure are presented to obtain an idea about the spatial dimensions of such an UHS; modified ffrom Heinemann et al., 2021

2.3 Induced Seismicity

Besides the uncertain behaviour of hydrogen under reservoir conditions, there are other risks related to UHS in saline aquifers, such as gas leakage along faults (Tarkowski, 2019) and induced seismicity (Vilarrasa et al., 2019). Induced seismicity is a topic of concern in all subsurface operations related to the injection or production of fluids and gases as it can damage infrastructure and, if felt, lead to public concern about the project (Ellsworth, 2013). In some cases, this induced seismicity has led to the closure of the storage project, with subsequent economic losses associated (e.g. Deichmann et al., 2009; Ruiz-Barajas et al., 2017). Thus, induced seismicity has to be understood and prevented in UHS as it can threaten the project.

The stress state starting from several tens of meters depth at intraplate regions is mainly compressive (Zoback, 2007), and thus it can be concluded that reservoirs are also dominated by a compressive regime and do therefore store elastic energy. Human activities, like UHS, cause changes in the stress state of a reservoir and can lead, if not done adequately, to the activation of critically stressed faults or caprock failure that eventually diminishes its sealing capacity (Suckale, 2009; Oldenburg, 2012; Zoback & Gorelick, 2012). One critical research question for any UHS project is therefore to accurately determine the pressure and stress range of each reservoir that represents a safety range in which the risk of fault activation or damaging the integrity of the caprock are avoided.

The effective normal stress and frictional resistance hold a fault together. As long as their product results in a stronger stress than the shear stress/tangential stress acting on that fault, it will remain locked (Ellsworth, 2013). The pore pressure (p) in the reservoir increases by injecting a gas or liquid into a formation, reducing the effective stress (Vilarrasa et al., 2019). In turn, pressure build-up induces poro-mechanical stress changes that alter the initial stress state. A fault becomes unstable and slides if the increased pore pressure and associated stress changes bring the stress state to failure conditions (King Hubbert & Rubey, 1959). This can be explained by:

$$\tau > \mu\,(\sigma_n - P) + \tau_O \qquad \text{(Verdon \& Strok, 2016)}$$

where τ is the shear stress resistance, μ is the friction coefficient, σ_n is the normal stress acting on the fault, P is the pore pressure and τ_O is the cohesion. If the shear stress acting on the fault plane is lower than τ, the fault remains stable, but if it becomes equal to τ, the fault is in failure conditions and will slip.

Not only can rock failure occur in shear mode, which may induce relatively large seismic events, but also in tensile mode (Jaeger et al., 2009), which only induces microseismicity not perceivable on the ground surface. Tensile failure occurs when pore pressure exceeds the least principal stress and the tensile strength of the rock (Barton et al., 2009). When tensile failure occurs, a hydraulic fracture is formed (Zoback, 2007). While some fracturing of the reservoir rock in UHS can be beneficial to enhance reservoir permeability, fracturing the caprock instead is not desired as it diminishes its sealing capacity and gas leakage could occur (Vilarrasa et al., 2013). Another effect that could diminish the caprock sealing capacity is the expansion of the aquifer due to the rising gas pressure. As the aquifer expands the caprock deforms and shear failure is eventually induced in the caprock (Yamamoto et al., 2013; Verdon & Stork, 2016). According to modelling experiences, this risk is reduced if the aquifer is stiff and consequently deforms less (Yamamoto et al., 2013).

Besides these two failing mechanisms, other factors do also have an impact on the magnitude of induced earthquakes. Larger faults have generally the potential to induce large earthquakes when reactivated (Ellsworth, 2013). Additionally, injection in deep reservoirs could also cause stronger earthquakes because injection occurs closer to the crystalline basement (Verdon & Stork, 2016), which tends to present higher deviatory stresses than the overlying sediments (Vilarrasa & Carrera, 2015). Also, when a hydraulic connection between reservoir and basement is present, earthquakes are favoured (Fan et al., 2019). Though, impermeable thus not hydraulic conductive faults are more likely to slip (Vilarrasa et al., 2016; Wu et al., 2021).

Once an induced earthquake occurs, it is not guaranteed that the risks of further induced seismicity disappear after injection is stopped. Post-injection earthquakes are common, and their magnitudes are often higher than by seismicity induced during injection (e.g. Deichmann & Giardini, 2009; Keranen et al., 2013; Cesca et al., 2014). Post-injection seismicity can be partly explained by pressure diffusion (Hsieh & Bredehoeft, 1981), though their higher magnitude seems to be caused by complex coupled processes, summarized by Vilarrasa et al. (2019). A detailed geological analysis of potential storage sites is thus strongly required as a preselection to identify and analyse the possible hazards (Tarkowski, 2019).

Therefore, this thesis will deal with analysing the risk of induced seismicity (fault slip or caprock fracturing) for hydrogen injection in a saline aquifer reservoir at Hontomín (Spain), which was formerly used as a GCS pilot site. The analysis will be conducted by hydro-mechanical modelling of an UHS.

2.4 Geology at Hontomín

The Hontomín structure, lying in North Spain, Burgos, is located in the south-east of the *Plataforma Burgalesa* (Fig.4), which is enclosed in the south-west of the Mesozoic Basque Cantabrian Basin (Alcalde et al., 2014). The *Plataforma Burgalesa* is constrained by the Ubierna Fault System to the south and by the *Sierra de Cantabria Thrust* to the north (Tavani et al., 2012). Three main phases that presumably affected the structure of Hontomín after the Triassic are proposed by Alcalde et al. (2014). During the first one, N-S fractures were generated during the Lias at a local scale by the initial stages of diapirism of the Hontomín structure. The second stage took place during Late Jurassic-Early Cretaceous by a regional N-S extension creating E-W normal faults. A regional compression caused by the Alpine Orogeny induced the third phase, where some faults were reactivated and inverted.

Nowadays there exists a local and a regional active tectonic strain shear field. One field contains a S_{Hmax} striking 50°E, the other field contains a S_{Hmax} tending to 150° E direction. Therefore, strike-slip faults striking N-S, NNE-SSW and NNW-SSE are affected by nowadays tectonics and could be potentially reactivated. In addition to that, a further extensional tectonic field with a N-S trend exposes right-lateral faults striking NNW-NNE and normal faults trending N-S to a further risk of activation (Pérez-López et al., 2020). On a larger scale, the western part of the Basque Cantabrian Basin could be dominated by a right-lateral transpressive active tectonic (Tavani et al., 2011), meaning that Hontomín could be located also in a transpressive regime.

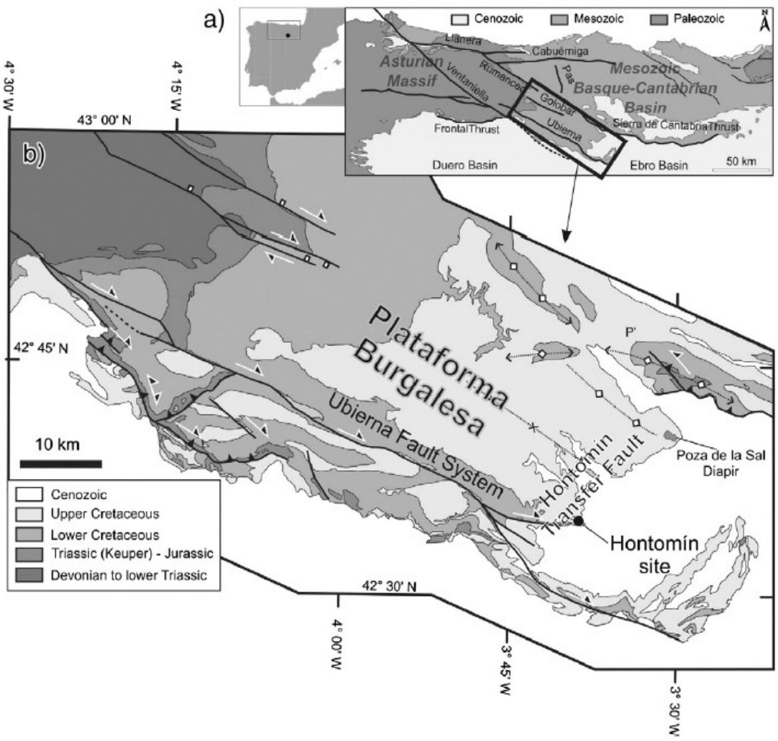

Fig. 4 (a) Location of the storage structure used for our models at the Iberian Peninsula and geologic map of the Asturian Massif and the Mesozoic Basque-Cantabrian Basin; (b) Zoomed to the southern part of the Mesozoic Basque-Cantabrian Basin including the Plataforma Burgalesa and the Hontomín site; Alcalde et al., 2014

A broad portfolio of investigation techniques was conducted to obtain information about the reservoir of Hontomín and its surrounding rocks. At two constructed wells, hydraulic characterization tests (Kovacs et al., 2015; de Dios et al., 2017), well logs and leak off tests were performed (de Dios et al., 2021; de Dios et al., 2017). Also, laboratory scale analyses were carried out with the borehole cores (de Dios et al., 2017). Furthermore, a reflection seismic campaign (Alcalde et al., 2013), a microgravity analysis (Andrés et al., 2016) and magnetotelluric measurements and modelling (Ogaya et al., 2014) were conducted. All these characterization experiments provide a comprehensive overview of the characteristics of the Hontomín structure.

The sedimentary formations of the Hontomín structure are located over a Palaeozoic basement (Vera et al., 2004). The storage structure consists of a reservoir and its base- and caprock. All these units are sediments from the Jurassic (Fig. 5a) presenting a structural dome with a size of 5×3 km (Fig. 5b) (Alcalde et al., 2014; Ortiz et al., 2015). The core of the dome consists of Keuper evaporites (Vera et al., 2004; Andrés et al., 2016). The base unit is composed of anhydrite and has probably a constant thickness of 100m (Alcalde et al., 2014; Andrés et al., 2016). The reservoir is a saline aquifer consisting of the *Sopeña Formation*, having an average thickness of about 80m. This formation is built of tidal developed dolomites at its bottom and limestone lias originating from a carbonate ramp at its top. The reservoir´s depth ranges from around 1450 m at the top of the dome to about 2287 m at the flanks (Alcalde et al., 2013; Alcalde et al., 2014). The main seal/caprock of the structure is composed of a marly lias, sedimented at a hemipelagic ramp, having an average thickness of 129.5m (Alcalde et al., 2014). The overburden on top of the target structure is Jurassic to Tertiary in age and consists of clastic or biogenic sediments, some of them working as a secondary seal (Vera et al., 2004; Alcalde et al., 2014).

The characteristics of each unit are quite different. The anhydrite formation has a very low porosity of 0.03% (Alcalde et al., 2014) and no fractures (Le Gallo & de Dios, 2018). In contrast, in the reservoir unit, a high amount of natural fractures are present. The reservoir can be considered as a dual permeability medium, as matrix permeability is very low but fracture permeability is much higher. Hence, permeability is strongly dominated by fractures, as fluid is transported almost exclusively through them. Nonetheless, the initial permeability of the whole reservoir is still low and beneath the required value for an attractive reservoir. However, the reservoir permeability is most likely not constant. Indeed, several brine injection tests at the two wells showed that if pressure in the reservoir builds up, permeability is enhanced. This can be explained by an elastic extension of the natural fractures due to pressure increase (Ortiz et al., 2015; de Dios et al., 2017; de Dios et al., 2021). Yet, the relationship between pressure increase and permeability enhancement is not clearly defined. Also, there is a significant heterogeneity in permeability in the vertical direction (de Dios et al., 2017) and probably also horizontally, as permeability analysis revealed different values at the two injection wells (Ortiz et al., 2015). Furthermore, different possible analyses of the injection tests result in different modelled permeabilities to fit the results of the injection tests (Ortiz et al., 2015). Howsoever, Ortiz et al. (2015) suggest the following constant values to describe the reservoir: a permeability of $1.5 \cdot 10^{-16}$ m^2 (Well 1) and $1.9 \cdot 10^{-15}$ m^2 (Well 2) at low BHP and a permeability of $1.2 \cdot 10^{-15}$ m^2 (Well 1) and $1.8 \cdot 10^{-15}$ m^2 (Well 2) at high BHP. However, it is not mentioned why these values are suggested. Some other analyses support a potential permeability increase up to $5.3 \cdot 10^{-15}$ m^2 (de Dios et al., 2017) or even $6.9 \cdot 10^{-15}$ m^2 (Ortiz et al., 2015). When the injection is finished, fractures do probably close again and permeability decreases again to the initial values (de Dios et al., 2017). A heterogeneity in the reservoir can also be seen in terms of porosity. It ranges from about 3% up to 18%, according to well logs (Alcalde et al., 2014) and from 0.2 to 16% according to laboratory analyses of the cores (de Dios et al., 2017). Yet, its average of 14% porosity represents a good value for a reservoir (de Dios et al., 2021). At the main seal/caprock no significant fractures have been detected (de Dios et al., 2017). Furthermore, it has a low porosity of 3.7% (Alcalde et al., 2014) and a low permeability of $9.8 \cdot 10^{-19}$ m^2, which characterizes the unit as a suitable caprock (de Dios et al., 2021).

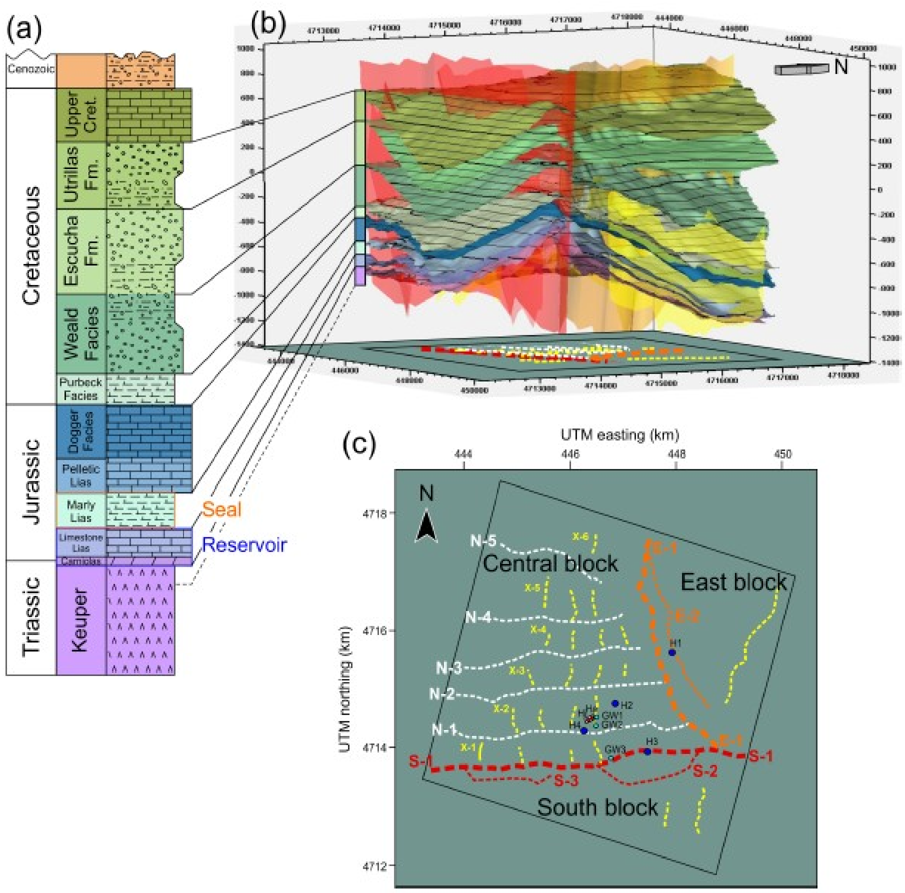

Fig. 5 (a) Geologic formations of the storage structure; (b) 3-D geometry of the storage structure with included faults (E-fault = red, S-fault = orange, X-faults = yellow); (c) Top view at the storage structure with all detected faults from Alcalde et al., 2014; Ogaya et al., 2016

Several leak-off tests revealed the pressure threshold for the reservoir and caprock at which fracking occurs (de Dios et al., 2017). The mean threshold values are 7 MPa bar for the caprock and 6-7.5 MPa for the reservoir formation. De Dios et al. (2017) concluded that, due to the occurrence of micro-seismicity, a bottom hole pressure of 22 MP at the two constructed wells should not be exceeded.

The existence of various faults subdivides the base, caprock and reservoir (Alcalde et al., 2014), without the sealing capacity of the caprock being diminished (de Dios et al., 2017; de Dios et al., 2021). According to their formation history, correlating with one of the three phases mentioned above, the faults can be separated into three different types. A set of small N-S faults (X-faults) crossing the base unit and reservoir, a set of longer extending E-W faults (N-faults) crossing the whole storage structure, and two big faults in the east and south (E-fault & S-fault) crossing both the storage structure and the overburden. The E- and S-faults compartmentalize the whole structure into a central block, a southern block and an eastern block (Fig.5 c) (Alcalde et al., 2014). These faults are eventually continuing into the basement (Andrés et al., 2016). This could mean a higher risk for induced earthquakes if they are hydraulically connected to the basement (Fan et al., 2019). Indeed, magnetotelluric measurements revealed a probable conductive fluid circulation at the S-fault and its region (Ogaya et al., 2014). Therefore, reactivation of the S-fault due to overpressure should be inhibited, as it could provoke a relatively large magnitude earthquake. Fortunately, nowadays tectonic studies indicate that the S-fault and also the N-faults are not critically stressed (Pérez-López et al., 2020). However, as there exists an active extensional N-S trending field, all N-S trending faults accumulate tectonic deformation and could act as normal faults (Pérez-López et al., 2020). This means that there could exist a higher risk for normal X-faults and also the big E-fault to slip. Hence, these faults have to be handled with care. It is not clear whether the E-fault is hydraulically connected to the basement, as it lays outside of the magnetotelluric model. Low resistivity in the eastern part of the model could indicate low resistivity of this fault and its region (Ogaya et al., 2014). Although, it is slightly speculated, this could mean that the E-fault is not hydraulically connected to the basement, thus the risk of hydrogen leakage and fault activation with high magnitude seismicity at this fault could be low. If the S-fault is permeable and the E-fault is low permeable this would mean, that the reservoir at Hontomín is half compartmentalized. The permeability of all other faults is not known but will be considered in this work as permeable inside of the reservoir and low permeable outside of it.

2.5 Previous Models of Hontomín

While modelling experiences of hydrogen injection into porous sandstone exist (e.g. Feldmann et al., 2016; Pfeiffer et al., 2016; Sáinz-García, 2017), none has been found for a fractured carbonate aquifer. To the best of our knowledge, no hydro-mechanical modelling of a hydrogen storage cycle inside of a compartmentalized fractured aquifer has been done before.

At Hontomín itself, the CO_2 injection into the storage formation has been modelled in two research studies. The first model is described in Le Gallo & de Dios (2018) and de Dios et al. (2019), and presents a complex and detailed geometry of the structure at Hontomín. It was modelled with GEM^{TM} using a three-dimensional dual permeability and porosity model containing spatially separated matrix and fractures for each unit and considers temperature effects and multiphase flow hysteresis. A whole fracture system with different properties than the rock matrix was modelled in a stochastic way with input data from field and laboratory tests. A constant permeability value for the fractures was approximated by an automated flow capacity calibration (Le Gallo & de Dios, 2018). CO_2 injection was performed in two modes, a constant flow rate mode and a constant injection pressure mode. The injection took place through a vertical well over the whole thickness of the reservoir with an injection rate of 2 kg/s for 8 hours and 2.2-1.7 kg/s for 24 hours for each mode, respectively. This should represent approximately an amount of 58 to 168 tonnes (1.3E^6 to 3.8E^6 mol) of injected CO_2.

Modelling results showed that the CO_2 plume did spread 80 m around the well (Fig. 6b). While pressure increased considerably within the plume, it rapidly dropped away from it (Fig. 6 a). Outside of the CO_2 plume, pressure just increased slightly around 3.5% compared to pre-injection pressure (Fig.2). The CO_2 saturation (Fig. 6b) lied around 0.62 at the inner part of the plume and 0.35 at its outer parts (de Dios et al., 2019). The abrupt changes in pressure increase and gas saturation in figures 2 and 3 should derive from a coarse meshing around the well.

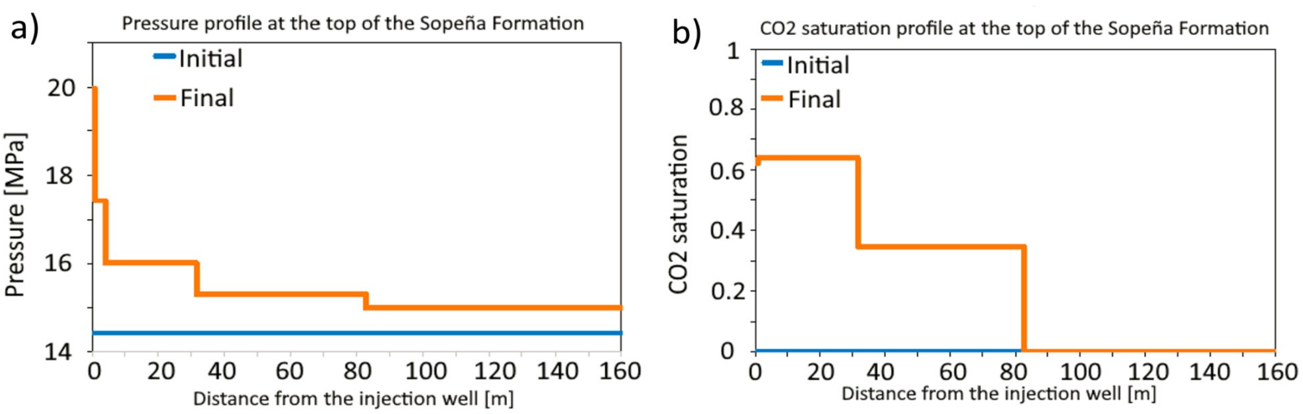

Fig. 6 (a) Pressure increase in the reservoir (b) Gas saturation in the plume; mod. de Dios et al., 2017

A second work from Sohal et al. (2021) dealt with investigating the effect of geological heterogeneities on reservoir storage capacity in the fractured carbonate aquifer of Hontomín. Therefore, long-term CO_2 storage (200 years) was simulated with the help of several three-dimensional models containing five different geological units with different properties and eight faults. The reservoir was modelled as a dual-porosity and dual permeability model, containing both matrix and fractures. Both permeability and porosity of all units were attributed as constant. Afterwards, a sensitivity study was realized with a scenario-based modelling approach. A base model with a homogeneous distribution of the parameters was created and compared to the other models, that were heterogeneous to varying degrees. Thereby, Sohal et al. (2021) investigated the effect in the storage capacity of the reservoir produced by heterogeneity of the porosity and permeability of the matrix or fractures and of the transmissivity of the faults. In each heterogeneous model, only the reservoir and just one parameter were attributed with some kind of spatial heterogeneity. The parameters of the homogenous model were history matched with well test brine- and water-alternating well test data. The heterogeneity was applied to the reservoir by giving different values of the investigated parameter to different locations, but always within realistic limits. The mean values of a parameter in all heterogeneous models were the same as in the homogenous model, but their standard deviation was higher. Thereby, more heterogeneity correlated with a higher standard deviation. The dependent variable, storage capacity, was measured with the help of the shut-in pressure. In all models, the same amount of 300,000 tonnes (~ $6.8E^9$ mol) of CO_2 was injected. It was assumed that for a reservoir with less storage capacity, the shut-in pressure will increase more and thus this parameter was considered as an adequate candidate to represent indirectly the different storage capacity of the models.

Modelling results of Sohal et al. (2021) showed that heterogeneity in permeability is positively correlated with a higher pressure build-up and with less storativity (Fig. 7 & 8). Furthermore, the shut-in pressure increase was inversely proportional to the permeability. The transmissivity of the faults instead seemed to have just a minor impact on reservoir capacity as shut-in pressure was just slightly increased in models with non-transmissive faults compared to models with transmissive faults. Only the transmissivity of the Ubierna fault (S-fault) and the R4- and R5-faults (far distant faults, not included in this work) had an impact on the shut-in pressure. The transmissivity of all other faults did not limit the reservoir storage capacity. Modelling results also indicated that the heterogeneous models correlated with more gas saturation from the top to the bottom layers compared to the homogenous base model.

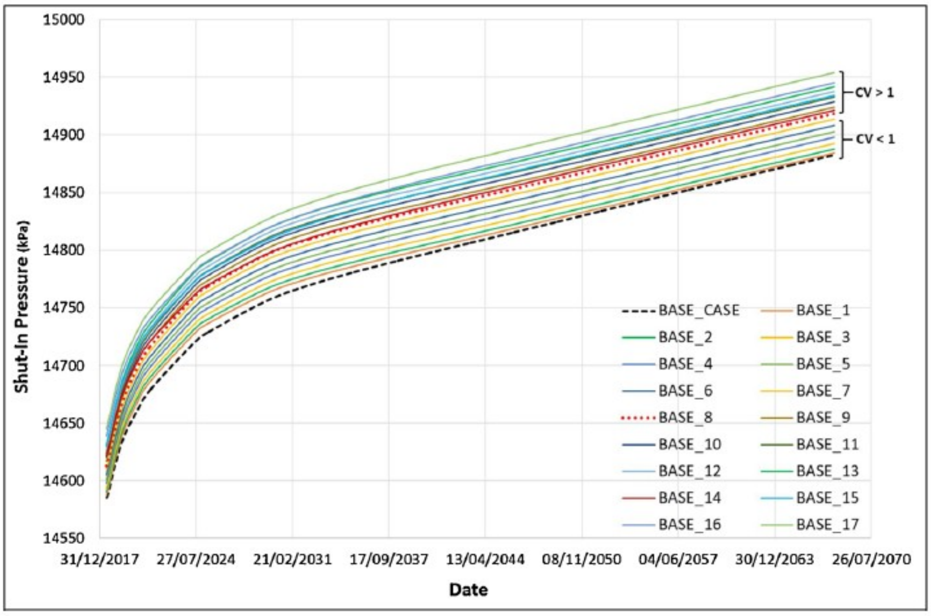

Fig.7 Pressure increase over time depending on heterogeneity in permeability. The higher CV the more heterogeneity; Sohal et al., 2021

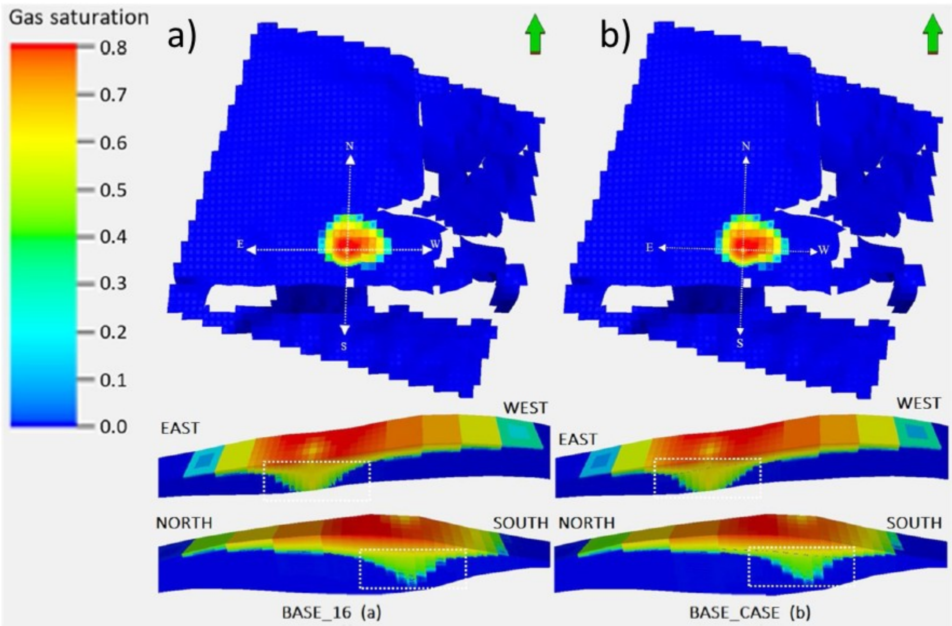

Fig.8 Gas saturation result in the homogeneous base model (b) and model with a heterogeneous permeability (a); Sohal et al., 2021

While the models of both works are quite complex and comprise a discrete fracture network, they do not include some aspects that could also be important. First, the dynamic elastic nature of the fractures, and thus, the increase of permeability together with pressure increase is missing. Yet, integrating a variable permeability in a model can be necessary to characterize a dynamic reservoir (Shi et al., 2019). Furthermore, no geomechanical coupling was considered in both works. Hence, the models do not include fault nor caprock stability analysis. However, fault slip and caprock fracturing can be a limiting factor to the storage capacity of a reservoir (Szulczewski et al., 2012). This means that Sohal et al. (2021) do not include an upper boundary to the storage capacity. They could be assuming that fault slip is not a limiting factor to storage capacity in their models, as just a slight shut-in pressure increase is modelled if all faults were not transmissive. However, neither Le Gallo and de Dios (2018) nor Sohal et al. (2021) includes the set of X- and N-faults detected in the seismic images by Alcalde et al. (2014). These faults could have a major impact on storage capacity also if they are transmissive as they already represent a zone of weakness and they are partly close to the injection point where pressure tends to increase significantly. Furthermore, they just observed shut-pressure increase at the injection well and not at the faults. Yet, a pressure increase at the faults could induce fault slip. Finally, both works, are modelling the injection of CO_2. However, the storage of H_2 could behave differently in some important aspects, like plume spreading, gas saturation or amount of storable gas. As these elements are missing, this work will involve modelling efforts intended to fill these knowledge gaps.

3 Aims & Hypothesis

In this scientific work modelling of an UHS in the semi compartmentalized carbonate aquifer of Hontomín is presented. Thereby, the effect of the permeability type on the aquifer's storage capacity is investigated. The permeability type is either constant or strain-dependent, representing a porous or fractured reservoir, respectively. Along the way, other interesting aspects resulting from the modelling outcomes are also discussed, as the UHS topic in such reservoirs is very novel. Two coupled hydro-mechanical two-dimensional models of an UHS are set up for this aim. These models advance and complement the work of Sohal et al (2021) by including heterogeneity in the from of a strain-dependent variable permeability and by integrating the set of X- and N- faults detected by Alcalde et al. (2014). The first model M1 has a reservoir with strain-dependent permeability (heterogeneous model / fractured reservoir) and the other model M2 has a reservoir with constant permeability (homogeneous model / porous reservoir). All faults besides the E-fault are transmissive inside the reservoir. Changes during the injection and resting phase of liquid pressure, gas pressure, gas saturation degree and stresses are included in both models. Consequently, a fault stability analysis is carried out for both models and all faults. The storage capacity is defined by the amount of H_2 that can be injected where, according to the analysis, fault slip is inhibited and where liquid pressure in the caprock does not exceed the threshold of fracturing.

Model M1 does represent the storage structure at Hontomín as realistic as possible with the existing data. As the Hontomín structure has already been used as a CO_2 storage pilot plant and is thus relatively well characterized, it was considered a good pilot site to investigate general questions on the novel field of UHS. In addition, results can be compared somewhat to the previous work of de Dios et al (2019) and Sohal et al (2021). However, due to the different modelling approaches and behaviour of CO_2 and H_2, it is expected that our modelling results will differ to some extent from their results. Furthermore, this work will also help to determine the suitability of both a porous- and a naturally fractured carbonate reservoir like at Hontomín for an UHS.

Based on the state of knowledge, we generated the following hypothesis: There is no significant effect of the permeability type on storativity; hence both reservoirs types have a similar storativity.

As more heterogeneity in permeability is correlated with a slightly higher pressure build-up (Sohal et al., 2021), a higher pressure increase could be expected in model M1 compared to model M2. However, at the same time, pressure increase is inversely proportional to permeability (Sohal et al., 2021). This could mean that the strain-dependency of the permeability compensates for higher pressure. Strain depends on pressure build-up. Thus, the more pressure is built up, the more permeability is created, which results again in lower pressures. Therefore, it is expected that both models M1 and M2 (variable vs. constant permeability) present a similar amount of pressure increase. This implies that both reservoir types, which differ just in the type of permeability, have a similar likelihood for fault slip or caprock fracturing, and thus a similar storativity.

The effect of the type of permeability on storativity is tested by comparing both models and their maximum amount of storable H_2 to each other. Thereby, the caprock fracturing- and fault stability analyses are necessary to detect the storage limit of the reservoirs.

4 Material & Methods

The modelled structure is a gentle dome of around 2.8 km, with six faults crossing the structure and subdividing it into several blocks that do have a vertical offset to each other. The reservoir of the structure is either naturally fractured or porous. Two models (M1, M2) of the structure were built that just differed from each other in the aspect that the reservoir was attributed with a strain-dependent (M1) or a constant permeability (M2). The models were calculated with the algorithm CODE_BRIGHT (Olivella et al., 1996; Olivella et al., 1994) using the program GiD, a pre- and post-processor for numerical problems. CODE_BIRGHT is a finite element code that solves numerically coupled hydro-thermo-mechanical problems including governing equations and constitutive laws. In this work, only hydro-mechanical analyses with constant temperature were calculated. The balance equations that were solved included the equilibrium of stresses and mass balance of the liquid- and gaseous phase. Dissolution of gas into the liquid phase was allowed. A gravity of -9.81 m/s^2 was applied to the whole model.

4.1 Geometry

Both models, M1 and M2, had the same geometry. It consisted of a 2.9 x 0.6 km sized two-dimensional model, modified from the profile α-α´ showed in Alcalde et al. (2014) and crossing the storage structure from SW to NE (Fig.6). The models included the storage structure, i.e., the base unit, the reservoir and the caprock, and further some of the overburden and the Keuper unit beneath the base. The upper part of the models lied in a depth of 1.73 km and the remaining overburden was not included.

Both the seismic image (Alcalde et al., 2014) and the corresponding magnetotelluric image (Ogaya et al., 2016) from the α-α´ profile were used for modelling a detailed geometry (Fig.9 & 10). Using both images was necessary, as the image from Ogaya et al. (2016) was depth converted but interpolated at the fault´s area, whereas, the image from Alcalde et al. (2014) was not interpolated but also not depth converted. The image of Ogaya et al. (2016) was imported to AutoCAD and scaled to its real size in meters. The units of interest on the image were digitized with the tool *spline line*. The geometry of the units was approximated with the image of Alcalde et al. (2014) close to the faults. Given that the base of the anhydrite unit is not interpreted in both images, but the thickness of the unit is known (Andrés et al. 2016), the base of the anhydrite was modelled 100 m beneath the base of the reservoir. The Keuper unit was modelled at the lower part of the model beneath the storage structure. At the *Hontomín* site, there are several different units above the caprock forming the overburden of the target structure. As these units were not important in the modelling work, they were merged into a single layer, called “top unit”.

Since the thickness of the fault zones is unknown it was approximated from the fault offsets. The correlation between fault zone thicknesses (y) and fault offsets (x) of multiple siliciclastic [1] and carbonate rocks [2] is described in Torabi et al. (2019).

$y = 0.054x^{0.6}$ [1]

$y = 0.1x^{1.1}$ [2]

As the faults in *Hontomín* do cross both types of rocks, an average formula of these two regression lines [3] was calculated.

$y = 0.07x^{0.8}$ [3]

With formula [3] and the fault’s offset, the corresponding fault thicknesses were derived. As it is suggested that some faults, but manly the E-fault and S-fault, have been inverted (Alcalde et al. 2014) their original offsets should have been bigger than their current ones. Therefore, as a rough approximation the calculated thickness of the X- and N-faults was multiplied by 1.25 and the E- and S- faults by 1.5. Used fault thicknesses can be seen in table 1 in the appendix.

All drawn structures were exported as igs-files and imported to GID. At the top of the reservoir’s dome, an injection well was placed three meters beneath the base of the caprock (Fig.11). The well was considered as a 1 km long horizontal well (not visible z-direction) with a diameter of 1 meter.

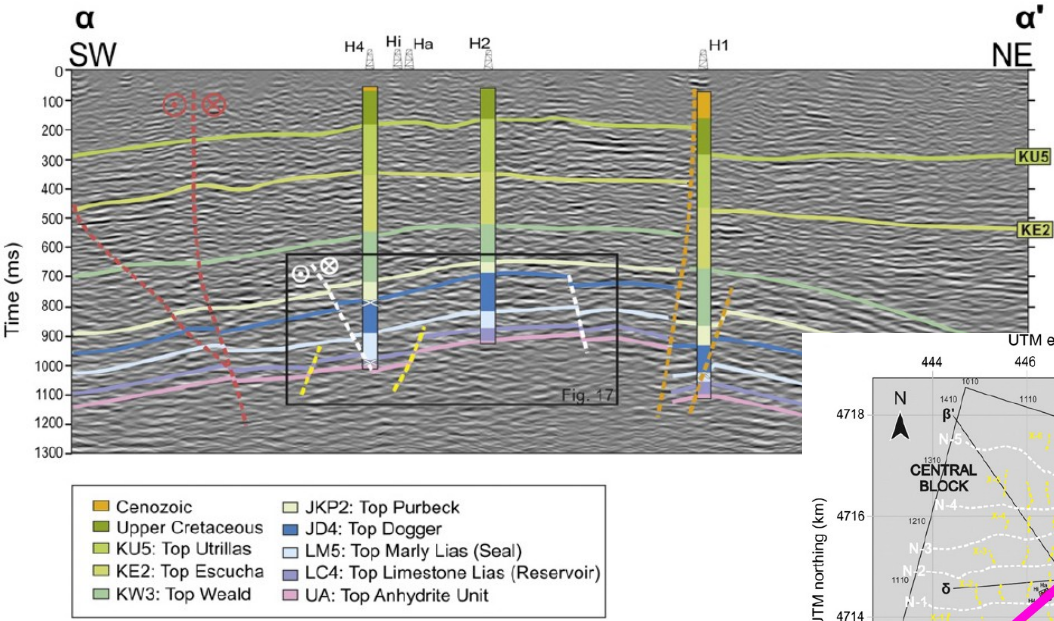

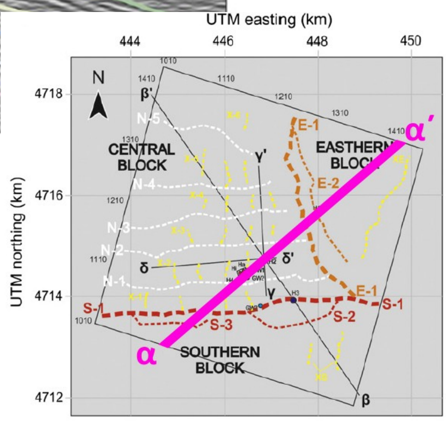

Fig. 9 Seismic Profile α-α´ (pink) and top view image) with all detected faults by Alcalde et al. (2014)

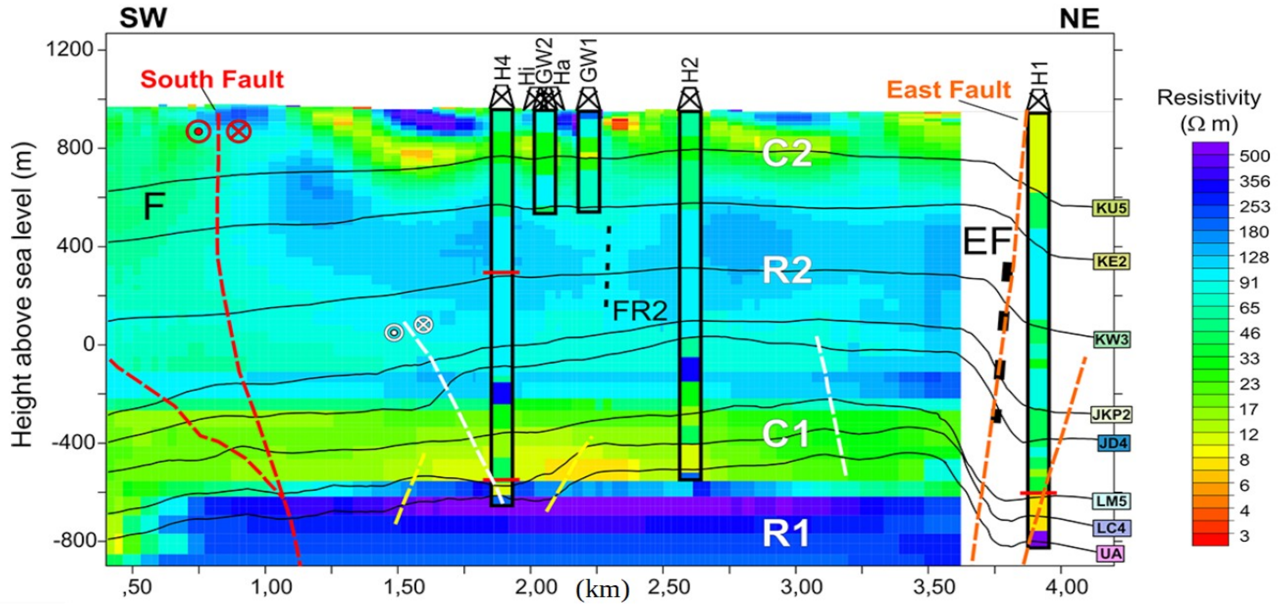

Fig. 10 Magnetotelluric Profile from Ogaya et al. (2016)

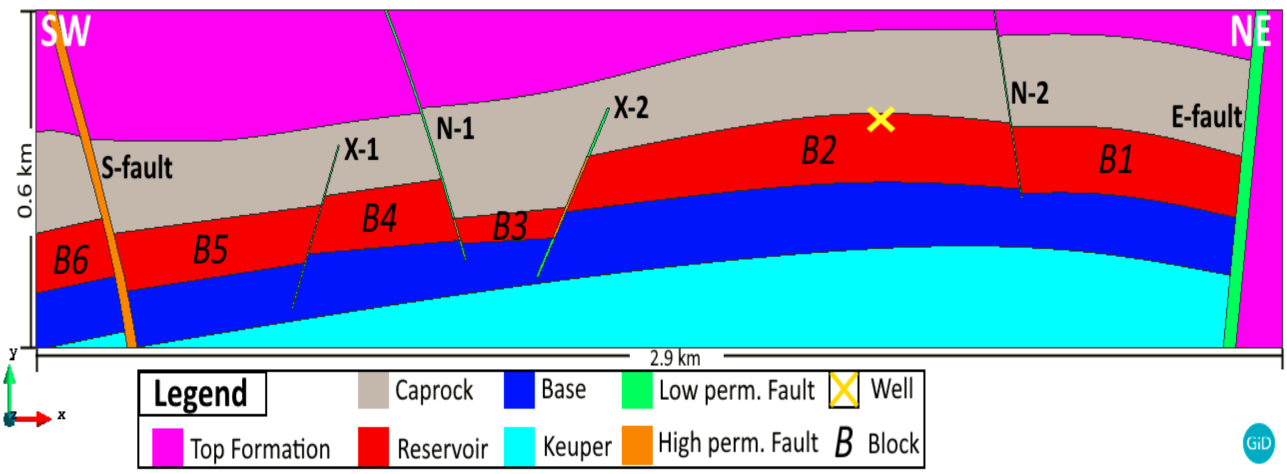

Fig. 11 Geometry of both models including all fault names and the blocks (B) the reservoir is subdivided by

4.2 Materials

All units and boundary conditions were, when possible, populated with realistic parameters from *Hontomín* obtained from the literature. If some parameters were unknown, their value was either taken from other examples from literature or assumed (personal elicitation). Hereinafter, only the three target units (i.e. base, reservoir and caprock) are discussed. The parameters of the units are summarized in tables 2 and 3.

4.2.1 Properties of Units

All properties were the same in both models except for the permeability of the reservoir. All units of the models were considered as homogeneous. Also, the natural fractures in the reservoir in model M1 were not modelled separately, due to their high density, small aperture and unknown spatial distribution. Therefore, the reservoir was not represented as a spatially separated dual permeability medium. Instead, it was modelled as a homogeneous porous medium, with a spatial variable permeability depending on the strain for model M1 and with a constant permeability for model M2. All other units were given a constant permeability in both models. The base- and caprock around the reservoir were parametrized as low permeable (Le Gallo & de Dios, 2018; Davila et al., 2016). The mechanical properties of the caprock and reservoir units were defined by the average Young´s modulus derived from laboratory scale analysis (de Dios et al., 2017) and the Poisson´s ratio, which was assumed to be 0.3 for all units. The caprock was more deformable than the reservoir and base unit, which were rather stiff. An average value for the porosity of the units was obtained from the well logs (Alcalde et al., 2014). The solid density was calculated with the help of the density and porosity log, assuming that all pores are completely filled with water

$$p_{total} = \Phi\, p_{water} + (1-\Phi)\, p_{solid} \qquad [4]$$

p_{total} = *Total density measured by well log*
p_{water} = *Density of water*
p_{solid} = *Density of solid material*
Φ = *Porosity measured by well log*

The models were considered as isothermal with a constant temperature of 44.86 C°, which represents the average temperature measured in the reservoir at *Hontomín* (de Dios et al., 2017). The gas phase density was defined by the molecular mass of H_2. By giving Henry´s constant a very high value, H_2 was considered as practically insoluble. As diffusion of H_2 under reservoir conditions is unknown, diffusion was set on default ($1.1\cdot10^{-4}$ m^2/s). The viscosity for H_2 at 50° C was used ($9.2343\cdot10^{-12}$ MPa·s).

The Keuper unit was characterized as a salt formation. The parameters for the top unit were calculated using the average parameters of the units that lie above the storage formation.

As modelling results from Ogaya et al. (2014) indicate the E-fault was considered as low permeable and the S-fault as completely high permeable. For both models the permeability of the

X- and N-faults was characterized as high permeable within the reservoir and low permeable outside of it. The permeable parts of the X- and N-faults and the S-fault were attributed with a permeability relatively high to the reservoir´s permeability to ensure that fluid flow is not hindered by these faults.

Table 2 Solid Phase Properties

	Young´s modulus [MPa]	**Source**	**Poisson´s ratio**	**Source**
Caprock	22500	Dios et al. (2017)	0.3	assumed
Reservoir	45000	Dios et al. (2017)	0.3	assumed
Base	49400	Hangx et al. (2009)	0.3	assumed
Top Unit	22500	assumed	0.3	assumed
Keuper	8100	Yan-Lin &Wen (2014)	0.3	assumed
Low Permeable Fault	22500	assumed	0.3	assumed
High Permeable Fault	22500	assumed	0.3	assumed
	Permeability [m^2]	**Source**	**Porosity**	**Source**
Caprock	$1 \cdot 10^{-18}$	Davila et al. (2016)	0.037	calc. from Alcalde et al. (2014)
Reservoir	$9.27 \cdot 10^{-15}$ m^2 (for M2)	Average value of reservoir in M1	0.14	calc. from Alcalde et al. (2014)
Base	$3.50 \cdot 10^{-19}$	Le Gallo & de Dios (2018)	0.01	calc. from Alcalde et al. (2014)
Top Unit	$1 \cdot 10^{-18}$	assumed	0.047	calc. from Alcalde et al. (2014)
Keuper	$1 \cdot 10^{-19}$	Liu et al. (2016)	0.01	assumed
Low Permeable Fault	$1 \cdot 10^{-18}$	assumed	0.037	assumed
High Permeable Fault	$5 \cdot 10^{-15}$ (for M2) $8 \cdot 10^{-15}$ (for M1)	assumed	0.14	assumed

	Solid Density [kg/km^3]	**Source**
Caprock	2704.42	calc. from Alcalde et al. (2014)
Reservoir	2683.14	calc. from Alcalde et al. (2014)
Base	2753.33	calc. from Alcalde et al. (2014)
Top Unit	2632.85	calc. from Alcalde et al. (2014)

Keuper	2170	aqua-calc.com
Low Permeable Fault	2704.42	assumed
High Permeable Fault	2704.42	assumed

Table 3 Liquid- and Gas Phase Properties; These properties are the same for all units

	All Units	**Source**
Temperature [°C]	44.86	Dios et al. (2017)
Liquid Phase Density [kg/m^3]	1015.9981	ITTC 2011
Molecular Mass of H_2 [kg·mol]	0.002016	calc. from Periodic System
Viscosity H_2 [Mpa·s]	$9.2343 \cdot 10^{-12}$	engineeringtoolbox.com

4.2.2 Variable and Constant Permeability of the Reservoir

The variable permeability depending on the strain was attributed to the reservoir in model M1. The increase of pore pressure caused by injection leads to a decrease in effective stress that expands the medium and thus the fracture aperture increases, enhancing permeability as

$$\mathbf{k} = \mathbf{k}_{matrix} + \frac{b^3}{12a} \quad [5]$$

$$b = b_o + \Delta b \quad [6]$$

$$\Delta b = a\Delta\boldsymbol{\varepsilon} = a(\boldsymbol{\varepsilon} - \boldsymbol{\varepsilon}_o) \ \text{ for } \ \boldsymbol{\varepsilon} > \boldsymbol{\varepsilon}_o \quad [7]$$

k = *Total permeability*

k_{matrix} = *Matrix permeability without fractures*

b = *Total fracture aperture*

b_0 = *Initial fracture aperture*

Δb = *Change in fracture aperture*

a = *Spacing of fractures*

ε_0 = *Reference strain*

ε = *Added strain*

$\Delta\varepsilon$ = *Change in strain*

A spacing of fractures of 0.427 m was calculated from the mean fracture density per meter in dolomites and carbonates at *Hontomín* (Le Gallo & de Dios, 2018) and the average thickness of the reservoir at the HI and HA well. The same matrix permeability of $4.93 \cdot 10^{-16}$ m^2 was used than Le Gallo & de Dios (2018), de Dios et al. (2019) and Sohal et al (2021) used for their models. Though, at *Hontomín*, matrix permeability seems to be quite heterogeneous as laboratory scale analysis detected permeabilities ranging from $9 \cdot 10^{-19}$ m^2 to $5.9 \cdot 10^{-16}$ m^2 (de Dios et al., 2017). However, in a formation where permeability is dominated by fractures as it is the case in the *Hontomín* reservoir, the exact knowledge of matrix permeability is not crucial.

The initial aperture of fractures b_0 is fairly uncertain for the reservoir at *Hontomín* and was therefore assumed. It was chosen so that the resulting initial permeability equalled approximately four times the matrix permeability ($b_0 = 2 \cdot 10^{-5}$ m). The maximum aperture of the fractures (b_{max}) was given a value ($5 \cdot 10^{-5}$ m), so that resulting permeabilities lied approximately in the range of permeabilities that de Dios et al. (2017) detected. However, the true values of both b_0 and b_{max} remain uncertain. Nevertheless, they could be seen as theoretical values, useful for calculating the strain-dependent permeabilities and approximating realistic values that were detected by de Dios et al (2017). All used parameters for representing the strain-dependent permeability are summarized in Table 4.

There is a certain anisotropy in terms of permeability at *Hontomín*. The fracture network into N-S direction seems to be more permeable than the fracture network in E-W direction (Le Gallo & de Dios, 2018). Though this anisotropy was not implemented into the models, because the seismic profile on which the model is based on is oriented SW-NE, meaning that the anisotropy cannot be properly seen in the profile.

The constant permeability for the model M2 was chosen from the average increased permeability that was reached at the end of the injection in blocks 1 to 5 in model M1. The end of the injection was chosen, as it was expected that the most liquid pressure increase and thus fault instability would be present at this time. Given that the fault slip could define the limit of the storage capacity, the permeability at this phase was expected to represent the best value for comparing the storage capacity between both models. The average permeability was approximated by exporting several cross-sections of permeability values along the area with increased permeability of model M1 with a vertical distance of 15 m. The arithmetic mean of these values was calculated ($9.27 \cdot 10^{-15}$ m^2). The permeability values of the faults were not included in this calculation as their permeability is constant in model M1.

Table 4 All parameters for modelling the strain-depending permeability

		Source
Matrix Permeability [mD]	0.5	Le Gallo & de Dios (2018); de Dios et al. (2019); Sohal et al. (2021)
Initial Aperture [m]	$2 \cdot 10^{-5}$	assumed
Maximum Aperture [m]	$5 \cdot 10^{-5}$	assumed
Spacing of Fractures [m]	0.427	calc. from Le Gallo & de Dios (2018)
Reference Porosity	0.14	calc. from Alcalde et al. (2014)
Minimum Porosity	0.13	assumed

4.3 Initial Conditions

The initial conditions were the same for all models. The initial stress state corresponds to a transpressional stress regime, where the vertical stress (S_v) equals the horizontal stress along the z-direction of the model (S_H). The horizontal stress in the x-direction (S_h) is the smallest principal stress:

$$S_v = S_H > S_h \quad [8]$$

The vertical stress is a result of the load from the overburden. It was calculated at the top and the bottom of the models. For this purpose, the densities and thicknesses of the overburden on top and of the units inside of the model (Alcalde et al., 2014) were used, respectively. The calculated stresses were 28.49 MPa at the top and 40.49 MPa at the bottom of the model. These stresses were interpolated vertically over the model, resulting in a gradient of around 2 MPa/100 m. S_h was calculated just by multiplying S_V by 0.65. This was assumed to be a representative relation between both stresses. At the bottom, western and eastern parts of the model, boundaries with no possible displacement were prescribed. On top of the model, a vertical stress of 28.49 MPa, representing the load of the overburden, was applied. Displacement was only allowed to take place at this border, as in reality, the contact between ground surface and atmosphere lies in this direction which allows an expansion of the rocks. At all other borders, displacement was not allowed, as the surrounding rocks restrain the geologic units to expand in their direction.

Also, the liquid pressure was defined at the top and bottom of the models and interpolated in between. It was assumed that the liquid pressure gradient at *Hontomín* is 1 MPa per 100 meters depth, resulting in a liquid pressure of 11.73 MPa at the top and 17.73 MPa at the bottom of the models. At the top of the models, a prescribed liquid pressure of 11.73 was applied.

4.4 Injection of Hydrogen

A given aquifer is presumably suited for one, maximum two injection cycles per year (Tarkowski, 2019). A UHS project with one cycle per year could thus involve 90 days of injection, 90 days of resting, 90 days of withdrawal and 90 days of resting again. For answering the scientific questions of this work the injection- and first resting phase are important given that the risk of fault slip or caprock fracturing is the highest at these phases. Therefore, just these two phases were modelled containing a time span of 90 days, respectively.

An appropriate injection rate that is directly related to the maximum amount of hydrogen that is possible to store was approximated by a trial and error technique for each of the two models. Several models with different injection rates were performed for both model types until an injection rate was found where the resulting liquid pressure did not surpass the caprock fracture threshold (an increase of 7 MPa) inside of this sealing unit and the mobilized friction of all faults was not surpassing 0.6. Appropriate injection rates for both model types, that are presented in the results, could be found. At the first 0.1 days during the injection phase hydrogen was injected by increasing the rate until reaching its appropriate value. During the remaining 89.9 days, a constant injection rate with the appropriate value was realized. At the resting phase of 90 days, no further hydrogen was injected.

However, also in both models with different permeabilities the same amount of H_2 was stored to make it possible to compare the results of the models to each other (e.g. M1 and $M2_{low}$ because in $M2_{lowe}$ not the maximum storable amount of H_2 is stored). This amount was oriented on the maximum storable amount of the reservoir that had less storage capacity (e.g. M1). After that, the appropriate amount of H_2 was stored in the other model (e.g. $M2_{high}$) so that the different storage capacities could be compared between the models.

Model convergence over the whole time was obtained by finding appropriate mesh size, time steps and parameters for the solution strategy. All these parameters are listed in tables 5,6 and 7 in the appendix and explained in more detail in the user´s guide of CODE_BRIGHT.

4.5 Fault Stability Analysis

Fault stability analysis was carried out for both models at all faults. Possible instability on faults was assumed to be detected by calculating the mobilized friction (relation between tangential stress and normal stress at a fault) at each fault. If the mobilized friction surpassed 0.6, the fault was considered to be at risk for slipping. Mobilized friction can be calculated from liquid pressure (P_L), S_h, S_V and tangential stress (S_{Vh}). These values were exported from GiD in two different ways. First, P_L, S_h, S_V and S_{Vh} were exported along faults just at the end of the injection- (day 90) and at the end of the resting phase (day 180). This was done that way because fault slip potential was assumed to be highest at these times. Second, P_L, S_h, S_V and SV_h were exported at just one position of each fault but for the whole modelled time, to ensure that potential fault slip could be detected over the whole time. The position for calculating the mobilized friction over time was located approximately where the highest liquid pressure increase and thus instability at each fault occured, respectively. It was assumed that both techniques together complement each other and should be able to detect potential fault slip.

The calculation was done by using the effective stresses (subtracting P_L from S_h and S_V).

The normal stress and tangential stress acting on each fault could be calculated as

$$\sigma_n = \frac{(\sigma_x{}' + \sigma_y{}')}{2} + \frac{(\sigma_y{}' - \sigma_x{}')}{2}\cos(2\theta) + S_{Vh}\sin(2\theta) \qquad [9]$$

$$\tau = \frac{(\sigma_y{}' - \sigma_x{}')}{2}\sin(2\theta) + S_{Vh}\cos(2\theta) \qquad [10]$$

σ'_x = effective horizontal stress

σ'_y = *effective vertical stress*

θ = *Dip angle of fault*

σ'_n = *effective normal stress on fault*

τ = *tangential stress on fault*

The relation between both represents the mobilized friction:

$$\phi = \tau / \sigma_n \qquad [11]$$

Furthermore, Mohr circles at each fault were created to understand the mechanisms behind the change of mobilized friction during the UHS and further, to detect possible differences between the models. The Mohr circle describes the general stress state at a given point. Its diameter is defined by the difference between the least principal stress (in our case the horizontal stress) and the largest principal stress (in our case the vertical stress) (Fig. 12). The tangential stress and normal stress acting on a plane like a fault can be determined at the intersection between Mohr Circle and a line originating from the centre point of the circle with twice the dip angle of the plane. If the intersection lies behind the failure envelope (tangential stress / normal stress = 0.6 in our case), the fault is unstable. Pore pressure- and stress changes lead the Mohr circle to a more stable or unstable state.

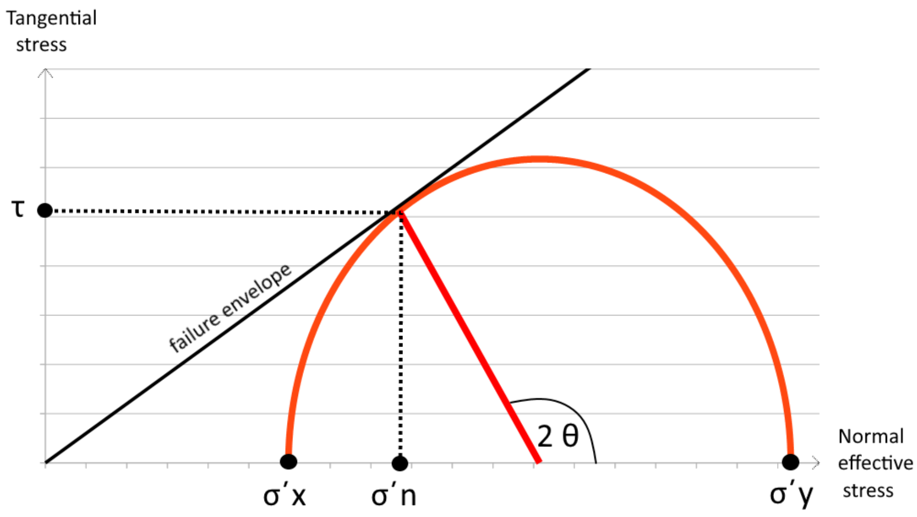

Fig. 12 Schematic representation of a Mohr circle in our reservoir: σ´x = effective horizontal stress, σ´y = effective vertical stress, θ = Dip angle of fault, σ´n = effective normal stress on fault, τ = tangential stress on fault; Note that the effective stresses are presented as liquid pressure is subtracted from the total stresses; the dotted lines indicate the tangential stress and normal effective stress acting on a given fault with the dip angle θ. This fault is just stable. If σ´x would decrease or σ´y increase the Mohr circle would grow and the fault would become unstable.

5 Results and Discussion

The modelling results revealed the effect of the permeability type on the storage capacity and also on general differences between the different storage types. As fault stability that could limit the reservoir's storage capacity depends on the stresses and liquid pressure, these results will also be discussed. Also, plume spreading will be presented as it correlates with liquid pressure spreading. Furthermore, the heterogeneous permeability increase in model M1 will also be elaborated on as it is considered a driving force to the different results between the two models.

5.1 Plume Characteristics

After the modelled H_2 injection, the plume size was similar in both models. It lay around 105 x 30 m in model M1 (fractured reservoir with strain-dependent permeability) and 104 x 33 m in model $M2_{low}$ (porous reservoir with constant permeability) at the end of the injection (day 90) and around 131 x 30 m in model M1 (Fig. 13) and 129 x 33 m in model $M2_{low}$ at the end of the resting phase (day 180). The hydrogen plume accumulated slightly asymmetrically beneath the caprock in both models (Fig. 7 and 8). It did spread around 10 m less in the direction where the low permeable E-fault lied (NE). The caprock in both models worked as a suitable seal as no gas leaked through it.
At both times during the end of injection and at the end of the resting phase the gas pressure, gas density and gas saturation within the plume were slightly higher in model M1. The difference of these parameters between the models increased during the UHS (Difference of gas pressure 0.07 MPa at day 90, 0.33 MPa at day 180; Difference of gas density 0.05 kg/m^3 at day 90, 0.25 kg/m^3 day 180; Difference of gas saturation 0.05 at day 90, 0.07 at day 180). These differences could arise from the different pressure dissipation in both models. In a model with heterogeneous and strain-dependent permeability like in model M1 pressure dissipation could be more difficult, resulting in higher gas pressure, gas density and gas saturation in the plume. Our results agree with the previous research of Sohal et al. (2021), which found a relatively high gas saturation for heterogeneous models compared to the homogenous model.

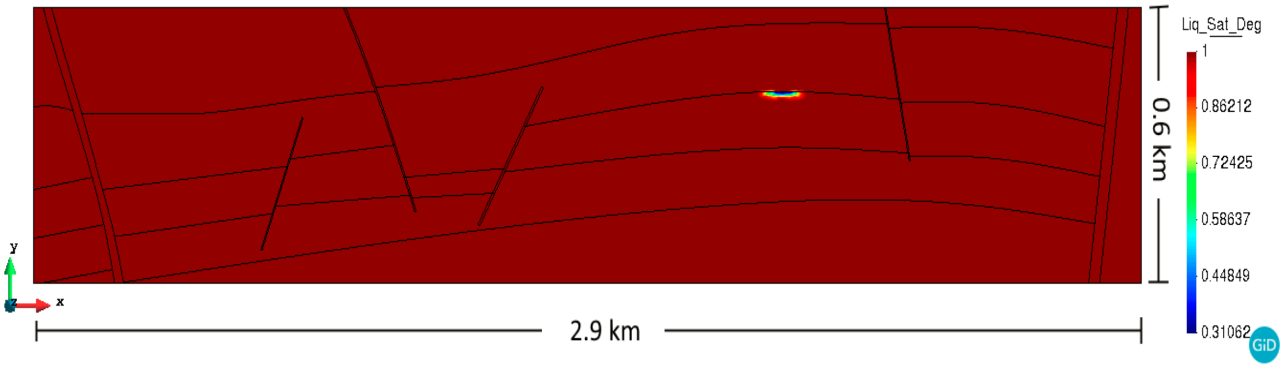

Fig. 13 H_2 plume spreading and gas/liquid saturation degree; end of resting phase model M1

5.2 Liquid Pressure & Permeability

Liquid pressure lied during the whole UHS beneath the 22 MPa, which de Dios et al. (2017) recommended as an upper limit to prevent induced seismicity. It was mainly affected inside the reservoir (Fig. 14 & 15). Liquid pressure increased in both models until the end of injection (Max.: 18.86 MPa in M1 & 18.59 MPa in $M2_{low}$) mainly in blocks 1 to 3 and then dropped slightly inside of the reservoir (Max.: 18.6 MPa in M1 & 18.2 MPa in $M2_{low}$) in these blocks during the resting phase. At the end of the injection, it mainly continued to increase in blocks 4 to 6 to around 17 MPa. Thus, main liquid pressure increases were shifted from blocks 1 to 3 to blocks 4 to 6 during the UHS. The maximum liquid pressure inside the reservoir accumulated during the injection at the bottom of the reservoir and during the resting phase at the low permeable E-fault. The pressure accumulation at the E-fault could have led to the asymmetrical plume spreading, as the higher overpressure in this direction (NE) pushed the plume into the SW, as already observed similarly by Vilarrasa et al. (2016).

During the UHS, pressure increase spread horizontally over the whole reservoir. Compared between the models, it appeared around 0.33 MPa higher in model M1 in the parts closer to the injection well, namely the NE and central part of the model. However, in the SW, liquid pressure was around 0.45 MPa higher in model $M2_{low}$ than in model M1 (Fig. 16 a). Yet, liquid pressure increase was around 2 to 3 MPa lower in the SW of both models compared to their central part and the NE (Fig. 16 b). Furthermore, liquid pressure increase dropped in the SW of X-2 compared to the NE in both models. This is eventually because the strong offset in the reservoir between blocks 2 and 3 worked as a semi barrier for liquid pressure spreading. The area where liquid pressure in model M1 was higher than in model $M2_{low}$ extended horizontally during the UHS. At the end of the injection, liquid pressure was higher in model M1 in blocks 1 to 3 and at the end of the resting phase liquid pressure was higher in model M1 in blocks 1 to 4 and lower in blocks 5 and 6.

In both models pressure increased inside of the high permeable S-fault, though this increase was stronger in model $M2_{low}$ (Max.: 18.2 MPa in M1 and 18.9 MPa in $M2_{low}$). This is as in model $M2_{low}$ liquid pressure rose in the early beginning of the UHS inside the whole reservoir. In model M1, on the other hand, liquid pressure increase during the injection was more restricted to blocks 1 to 4. Only during the resting phase, when liquid pressure in blocks 1 to 3 decreased, it increased in blocks 5 and 6 and could reach the S-fault.

The liquid pressure increase correlated with the increase in permeability in model M1. At the beginning of the UHS, the reservoir in model M1 had an initial permeability of $4.93 \cdot 10^{-16}$ m^2 that represented the permeability with the initial fracture aperture. Then, permeability started to increase around the injection well (Fig. 17), representing the opening of the fractures. At the end of the injection, it was mostly increased in blocks 1 to 3 (around $1.2 \cdot 10^{-14} m^2$). The low permeable E-fault in the NE lead to a relatively fast and high liquid pressure and thus permeability increase. Therefore, permeability was higher in the NE than in the SW. Later, at the end of the resting phase, permeability values dropped somewhat inside blocks 1 to 3 (around $1 \cdot 10^{-14} m^2$) but increased further in blocks 4 to 6 (around $1 \cdot 10^{-15} m^2$ to $5 \cdot 10^{-15} m^2$).

The different behaviour in liquid pressure spreading between the models arose from the different permeabilities. While in the reservoir with constant permeability (M2) pressure dissipation could occur relatively homogeneously as permeability was the same in all directions, in the reservoir with strain-dependent permeability (M1), pressure dissipation could have been hindered by the heterogeneous permeability distribution that restricts pressure dissipation in the reservoir. The areas in model M1 with relatively low initial permeability could work as a semi barrier for fluid flow and thus pressure dissipation. Therefore, liquid pressure in model M1 was more accumulated in the area with increased permeability (e.g. blocks 1 to 3 at the end of injection) and thus higher than in model $M2_{low}$.

This is the case, although the permeabilities in blocks 1 and 2 were higher in model M1 than the constant permeability of model $M2_{low}$ ($9.26 \cdot 10^{-15} m^2$). This shows that the findings by Sohal et al. (2021), who mentioned that pressure increase is inversely correlated to permeability, cannot be applied to our model M1. While this is true for their models with arbitrary constant permeability distribution, our results show that the arrangement of the heterogeneous permeability is also essential. If the permeability is strain-dependent, which means it decreases with increasing distance from the injection well, both liquid pressure and permeability can be higher around the injection point (M1) than in a reservoir with constant but lower permeability at the well ($M2_{low}$).

However, our results agree mainly with the finding of Sohal et al. (2021) that states that more pressure increase occurs in the heterogeneous models. Indeed, in model M1 liquid pressure was at the beginning of the UHS higher close to the injection point and over time also at most parts of the reservoir. Also, its absolute increase was higher than in model $M2_{low}$. However, in model $M2_{low}$ liquid pressure increased more at locations relatively far distant from the injection well. Though, not so much as pressure increased at the injection well of both models. As Sohal et al. (2021) measured the liquid pressure only at the injection well, this effect is probably not measured in their work.

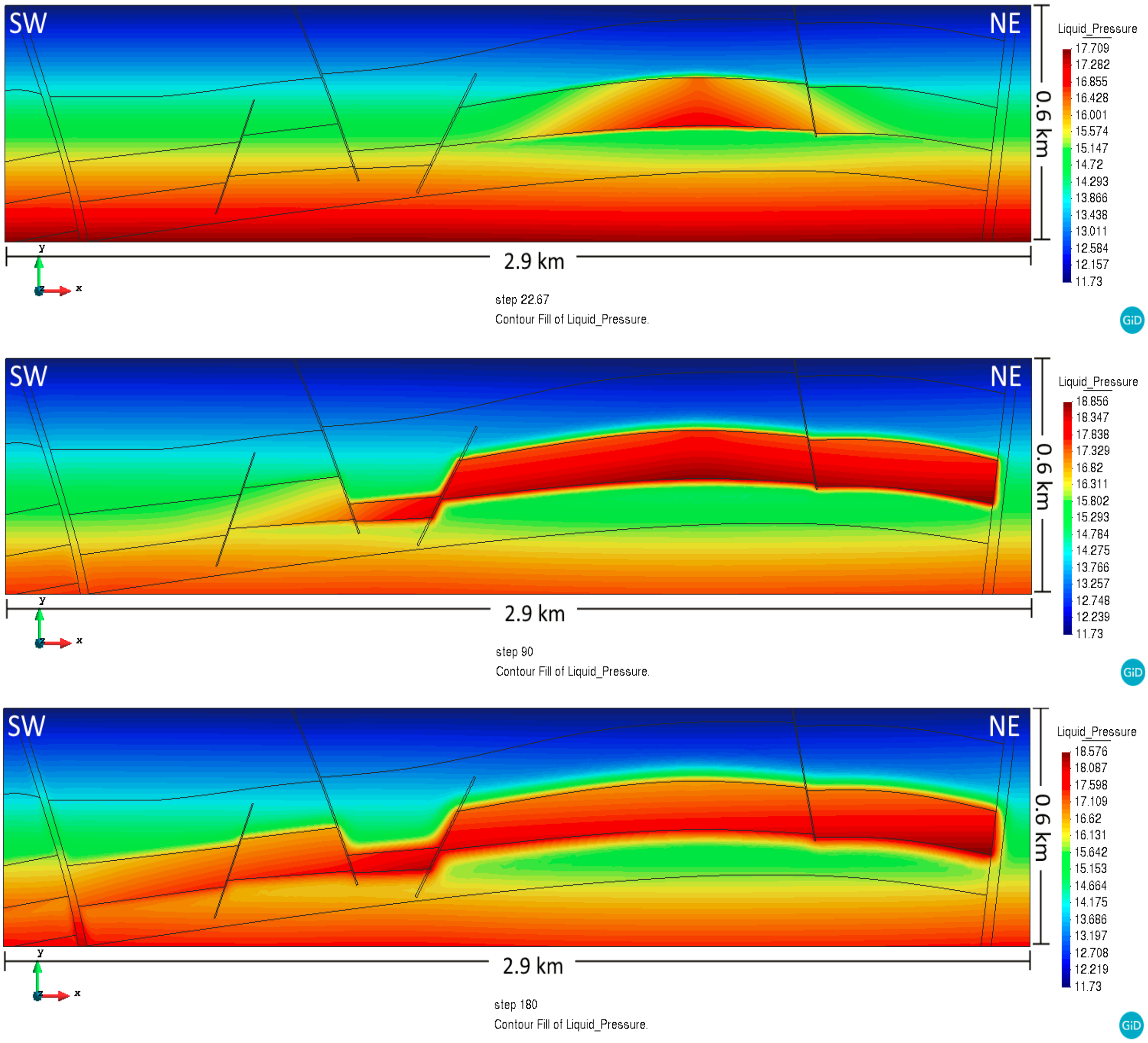

Fig. 14 Liquid pressure increase [MPa] during UHS model M1; from top to bottom: during injection (day 22), at the end of injection day (90) & at the end of the resting phase (day 180)

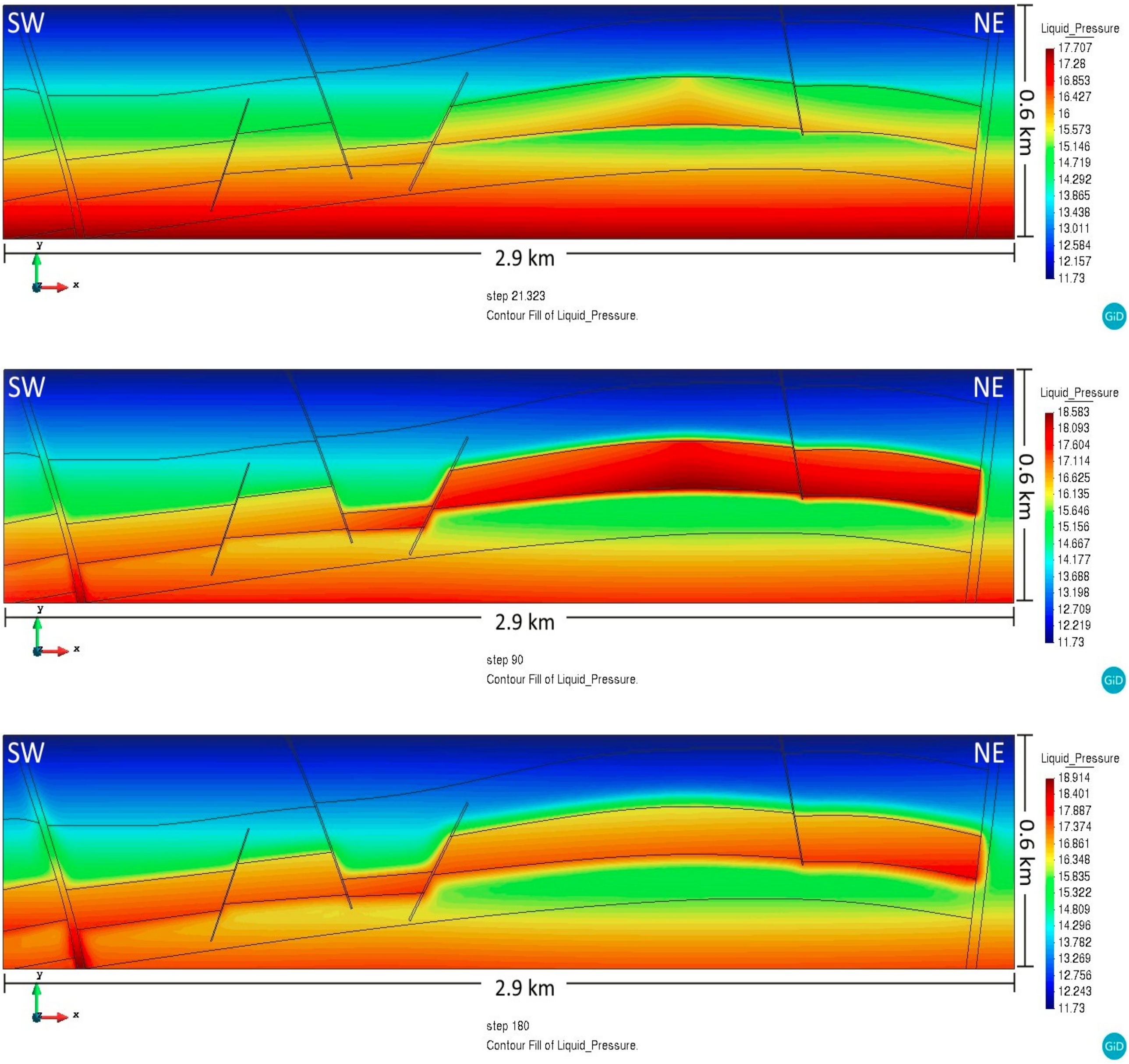

Fig. 15 Liquid pressure increase [MPa] during UHS model M2$_{low}$; from top to bottom: during injection (day 22), at the end of injection day (90) & at the end of the resting phase (day 180)

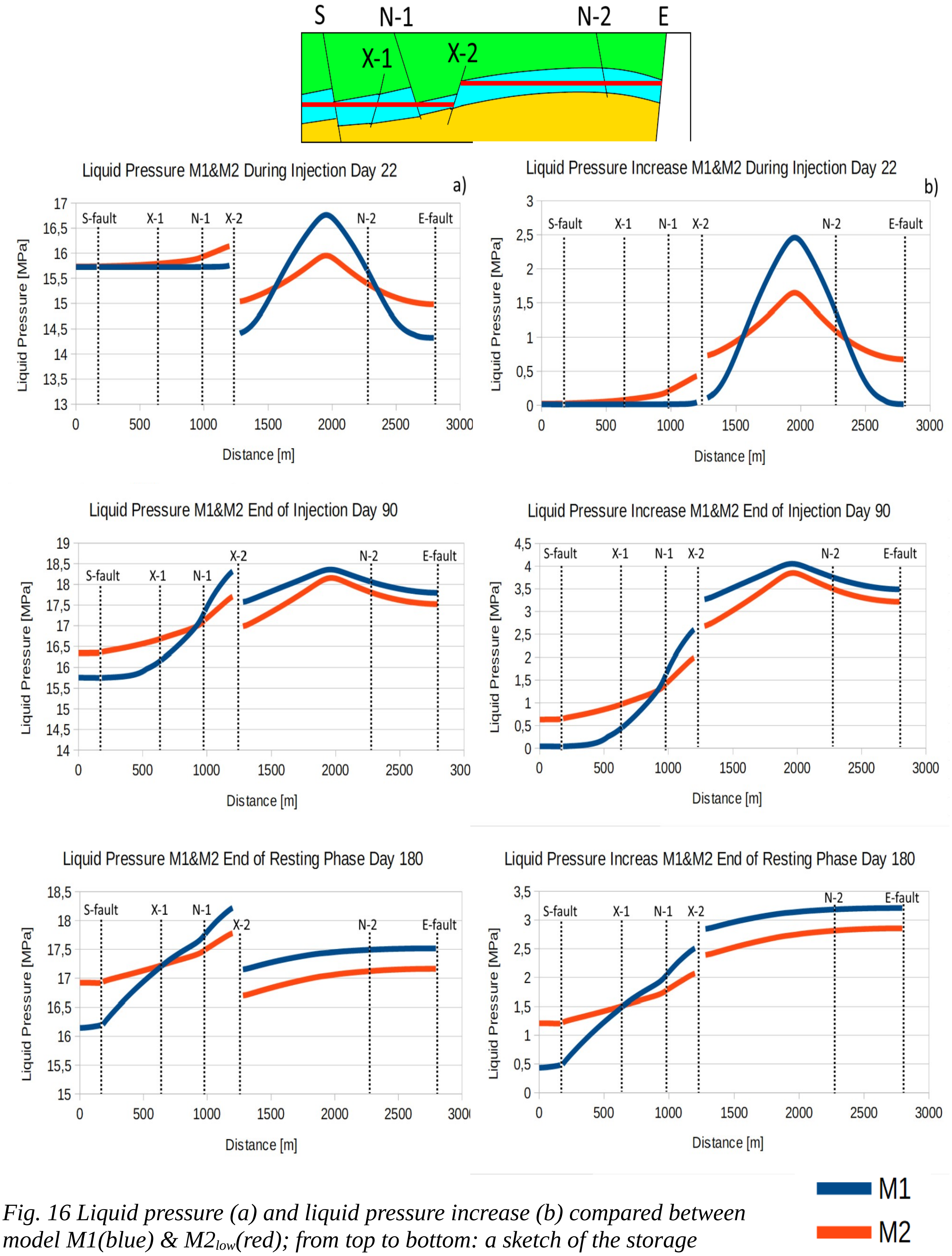

Fig. 16 Liquid pressure (a) and liquid pressure increase (b) compared between model M1(blue) & $M2_{low}$(red); from top to bottom: a sketch of the storage structure and the line where liquid pressure was exported, liquid pressure and liquid pressure increase during injection (day 22), at the end of injection (day 90) & at the end of the resting phase (day 180). Note that fault X-2 marks a strong offset in the reservoir; therefore, liquid pressure is relatively high in the SW of X-2

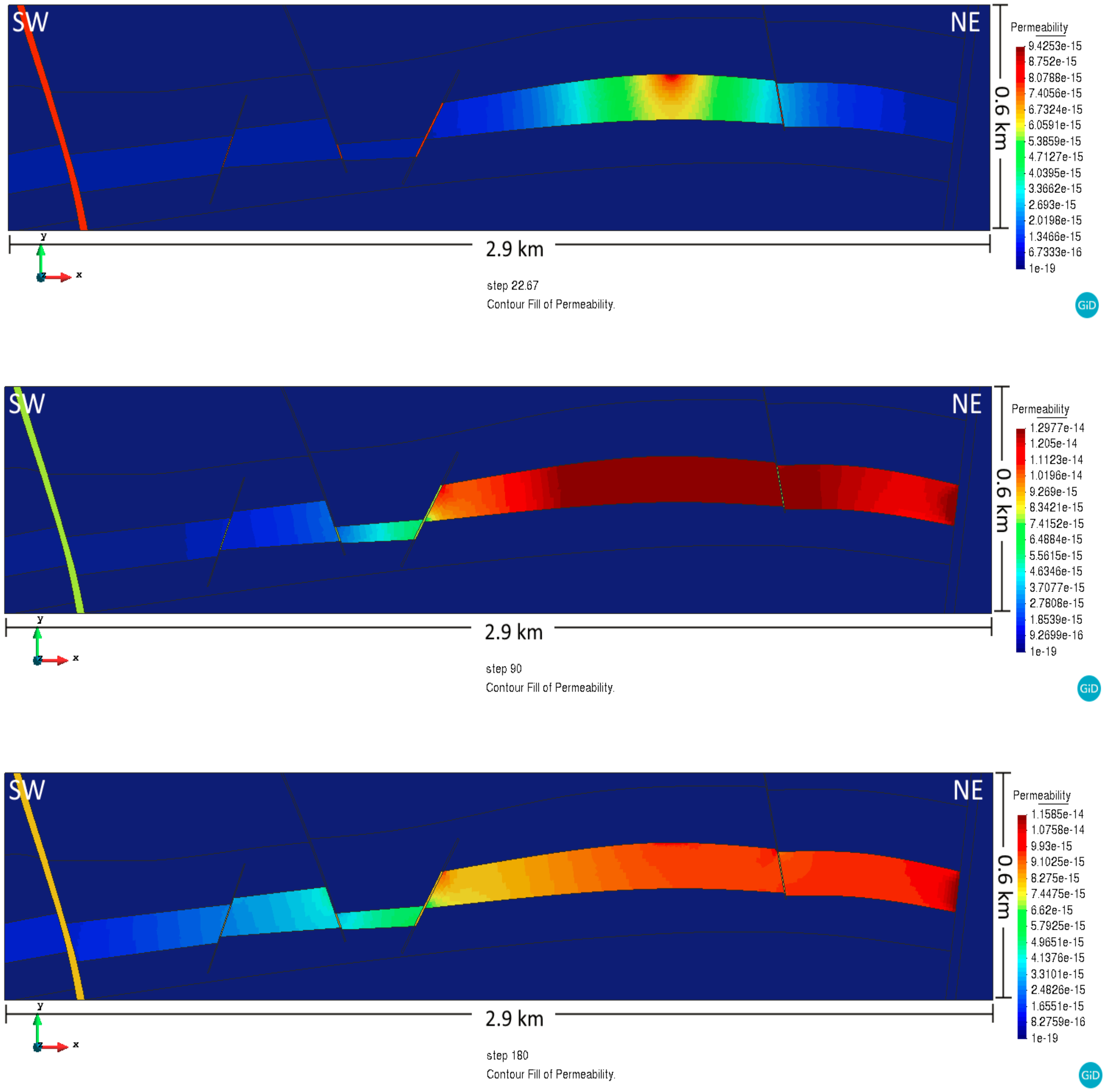

Fig. 17 Permeability [m^2] increase during the UHS in model M1. From top to bottom: During the injection (day 22), at the end of injection (day 90) & at the end of the resting phase (day 180). Note permeability increases radial around the injection well; later permeability is mainly increased in blocks 1 & 2. Later permeability decreases slightly but permeability increase extends over the whole reservoir.

5.3 Caprock Stability & Displacement

During the UHS maximum, liquid pressure increase inside the caprock was quite high (~3.5 MPa) in both models. However, its maximum value lay well beneath the fracturing threshold of the unit (7 MPa increase) during the whole simulation and thus, tensile failure of the rock was inhibited. Also, shear failure due to the extension of the reservoir seemed not to be a risk as both the maximum vertical and horizontal displacements of the caprock and also of the whole model were just around 8.6 (model $M2_{low}$) to 9.1 (model M1) and 3.2 (model $M2_{low}$) to 3.4 (model M1) millimetres, respectively (Fig. 18 and 19).

However, vertical displacement in model M1 was not higher in the whole model. In model M1, vertical displacement was higher relative to model $M2_{low}$ approximately from block 1 to the half of block 4. In the SW of the model at the half of block 4 to block 6 vertical displacement was around 1 mm higher in model $M2_{low}$. This behaviour correlated with the liquid pressure increase that also showed a tendency to be higher in blocks 1 to 4 in model M1 and higher in the SW of model $M2_{low}$. This correlation arose as liquid pressure has an influence on displacement. Liquid pressure increase led to an expansion of the reservoir and thus to the rise in total horizontal- and vertical stress that is partly transformed to a horizontal or vertical displacement, respectively.

Thereby, total vertical stress increase should have been lower than total horizontal stress increase, as vertical displacement is higher than horizontal displacement in both models. That should have been because the upper boundary of the models was the only boundary where displacement was allowed. As explained earlier, this was made to represent the atmosphere above the ground surface where an expansion of solid material is not restricted. The horizontal displacement, on the other hand, is restricted by the surrounding rocks. The small horizontal displacement in the models should thus have occurred by compression of rocks and liquid inside of the model and not by displacement of the boundaries.

Interestingly, the baserock beneath blocks 1 to 3 got slightly compressed (~2 mm) during the UHS whereas, this unit experienced extension (~1mm) beneath blocks 4 to 6 in both models (Fig. 20). The compression of the baserock beneath blocks 1 to 3 can be explained by the extension of the reservoir. Though, the extension of the baserock beneath blocks 4 to 6 could arise from more complex processes. As blocks 2 and 3 had a strong offset connected by the fault X-2, the offset also formed a kind of semi barrier. This strong offset could have slightly hindered liquid pressure dissipation. Therefore, more pressure accumulated inside blocks 1 and 2, which are undergoing a substantial expansion. This could have led to horizontal compaction of the blocks in the SW of X-2.

As horizontal displacement was not allowed at the SW boundary of the model, these blocks moved instead upwards. Therefore, the baserock beneath these blocks extended slightly.

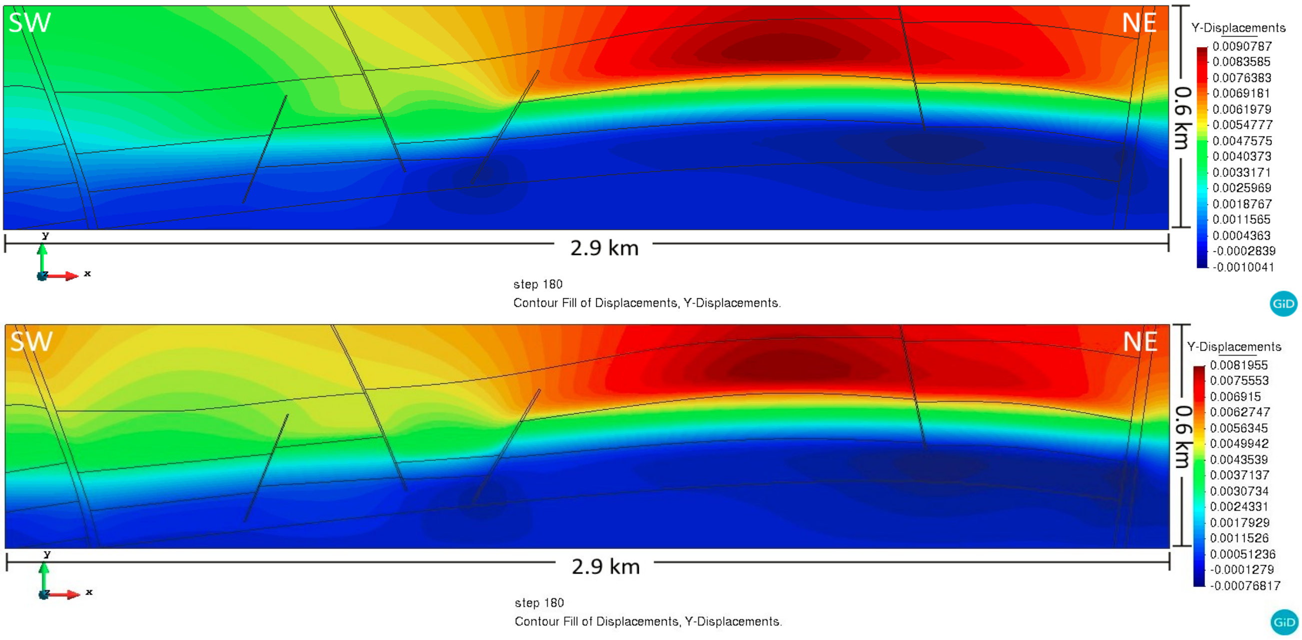

Fig.18 Vertical displacement [m] at the end of the resting phase of model M1 (upper image) & model M2$_{low}$ (lower image); Note that displacement above the reservoir is higher in model M1 in the central part and the NE but higher in model M2$_{low}$ in the SW. Beneath blocks 1-3, the baserock got compressed (negative displacement values), beneath blocks 4-6, the basreock underwent extension (positive displacement values)

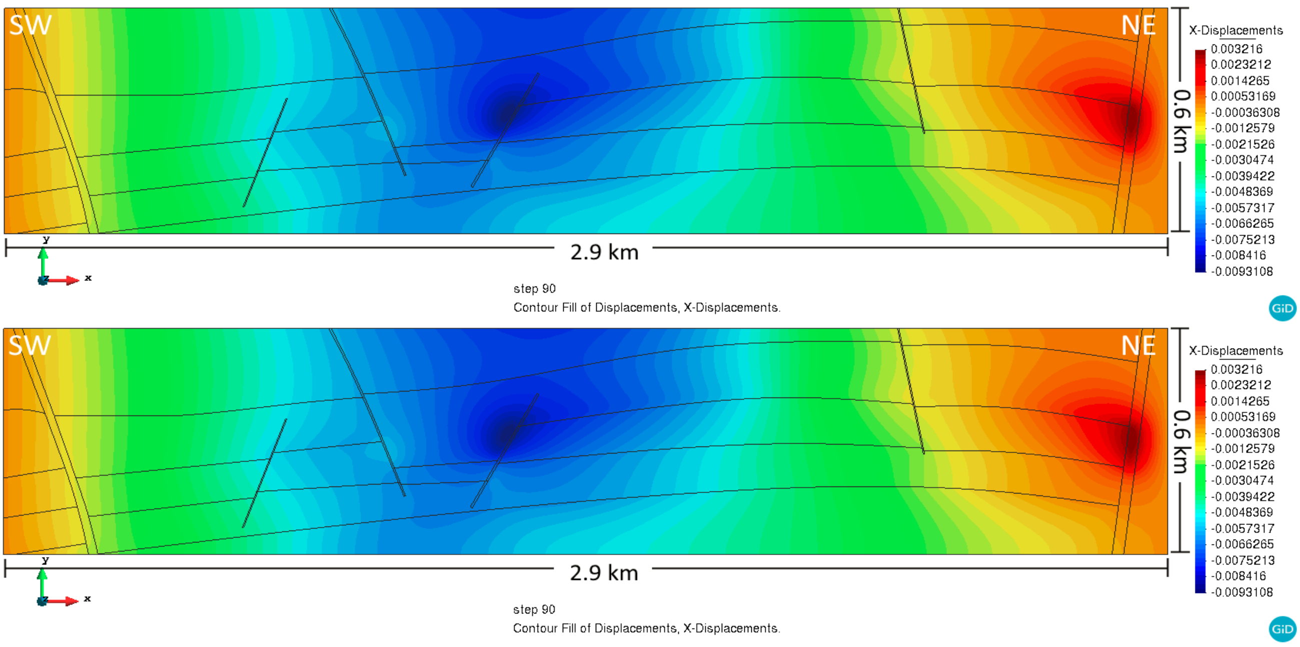

Fig.19 Horizontal displacement [m] at the end of the injection of model M1 (upper image) & model M2$_{low}$ (lower image); Note maximum horizontal displacement exists at the upper part of X-2 and the middle part of the E-fault.

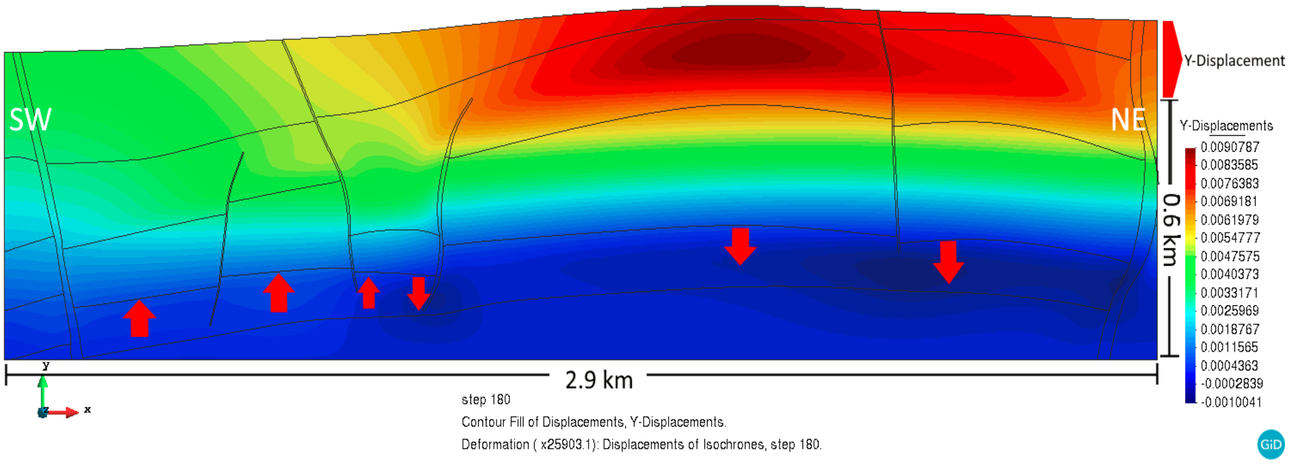

Fig. 20 Vertical displacement [m] 25903 times stronger than in reality at the end of the resting phase of model M1; Red arrows inside of the image indicate vertical displacement of the baserock, the red arrow at the right side of the image indicates vertical displacement of the whole storage structure; Note that beneath blocks 1-3 the baserock got compressed (negative displacement values), beneath blocks 4-6 the basreock underwent extension (positive displacement values)

5.4 Stress Differences between Models

As the faults in our models are approximately vertical, the total horizontal stress tended to stabilize these faults whereas, the total vertical stress tended to destabilize them. During the UHS total vertical stress increased less inside of the faults than total horizontal stress in both models. Total vertical stress increase lay approximately about 0.2 to 0.8 MPa in model M1 and around 0.3 to 0.6 MPa in model $M2_{low}$. Thereby, the amount of increase was mostly depending on the fault. Total horizontal stress instead, increased roughly around 0.4 to 1.8 MPa in model M1 and around 0.8 to 1.8 MPa in model $M2_{low}$. Thereby, total horizontal stress rise decreased with increasing distance to the well, in particular in model M1. Having a higher total horizontal stress rise results presumably from the earlier mentioned higher vertical- rather than horizontal displacement, thus accumulating less total vertical stress.

The area of total horizontal stresses increase correlated with the area of liquid pressure increase during the UHS. It differed between the models on average around 0.14 MPa at both the end of the injection and the end of the resting phase, tending to be higher in model M1 in blocks 1 to 4.

Surprisingly, total vertical stress in the reservoir but outside the faults was not much affected during the UHS in both models. Its maximum increase lied around 0.2 located at the E-fault but it mainly increased less than 0.05 MPa in the rest of the reservoir. Therefore, total vertical stresses along the reservoir were almost the same in both models during the UHS. The mean difference of total vertical stress between the model was around 0.01 MPa.

Even though total vertical- and horizontal stress increased during the UHS, the effective vertical- and horizontal stress, resulting by subtracting the liquid pressure from total stresses, decreased, above all inside the reservoir. This can be explained by the increase in liquid pressure that was significantly stronger than the total vertical- and horizontal stress increase. Furthermore, differences between the models in liquid pressure were approximately three times higher (~0.37 MPa) than differences of total horizontal stresses and thirty-seven times higher than differences of total vertical stresses. Therefore, liquid pressure is considered the most important parameter to explain potential differences in fault stability in our models.

5.5 Fault Stability

The fault stability analysis revealed that the most affected faults in both models were the faults close to the injection well, namely the E-fault, N-2 and X-2 (Fig. 21 and 22). Their stability decreased significantly during the UHS, represented by an increase in mobilized friction (ratio between tangential- and normal effective stress). The general difference of all faults between the two models was the amount of increase in mobilized friction, which tended to be higher in model M1. The mobilized friction of X-2 in both models was most close to the critical value of 0.6, whereas the mobilized friction of all the other faults was significantly lower than 0.6 during the UHS (Fig. 9). The maximum increase in mobilized friction at X-2 was the highest (M1 = 0.1; $M2_{low}$ = 0.07). Furthermore, the initial mobilized friction at X-2 was relatively high, having a value of around 0.5. The E-fault and the fault N-2 (Fig. 27) did also have a relatively high maximum increase in mobilized friction (M1: E-fault = 0.053, N-2 = 0.073; $M2_{low}$: E-fault = 0.047, N-2 = 0.065). However, their initial value lay roughly around 0.2 (E-fault) and 0.26 (N-2). The mobilized friction of the E-fault, N-2, X-2 and N-1 were mostly affected where the faults were in contact with the reservoir. In the parts of the faults that lay inside of the caprock or baserock, mobilized friction at the end of injection and the end of the resting phase lay closer to its initial value. At the S-fault, however, the part mostly affected in terms of stability lay at the low part of the fault located inside of the baserock (Mob. Fric. Increase: M1 = 0.011; $M2_{low}$ = 0.044). The fault X-1 in both models and the S-fault in model M1 formed the least destabilized faults of all. Its maximum increase in mobilized friction lay around 0.01. As the parts in contact with the reservoir were for most faults mostly affected by the UHS, the results of these parts will be mainly shown and discussed.

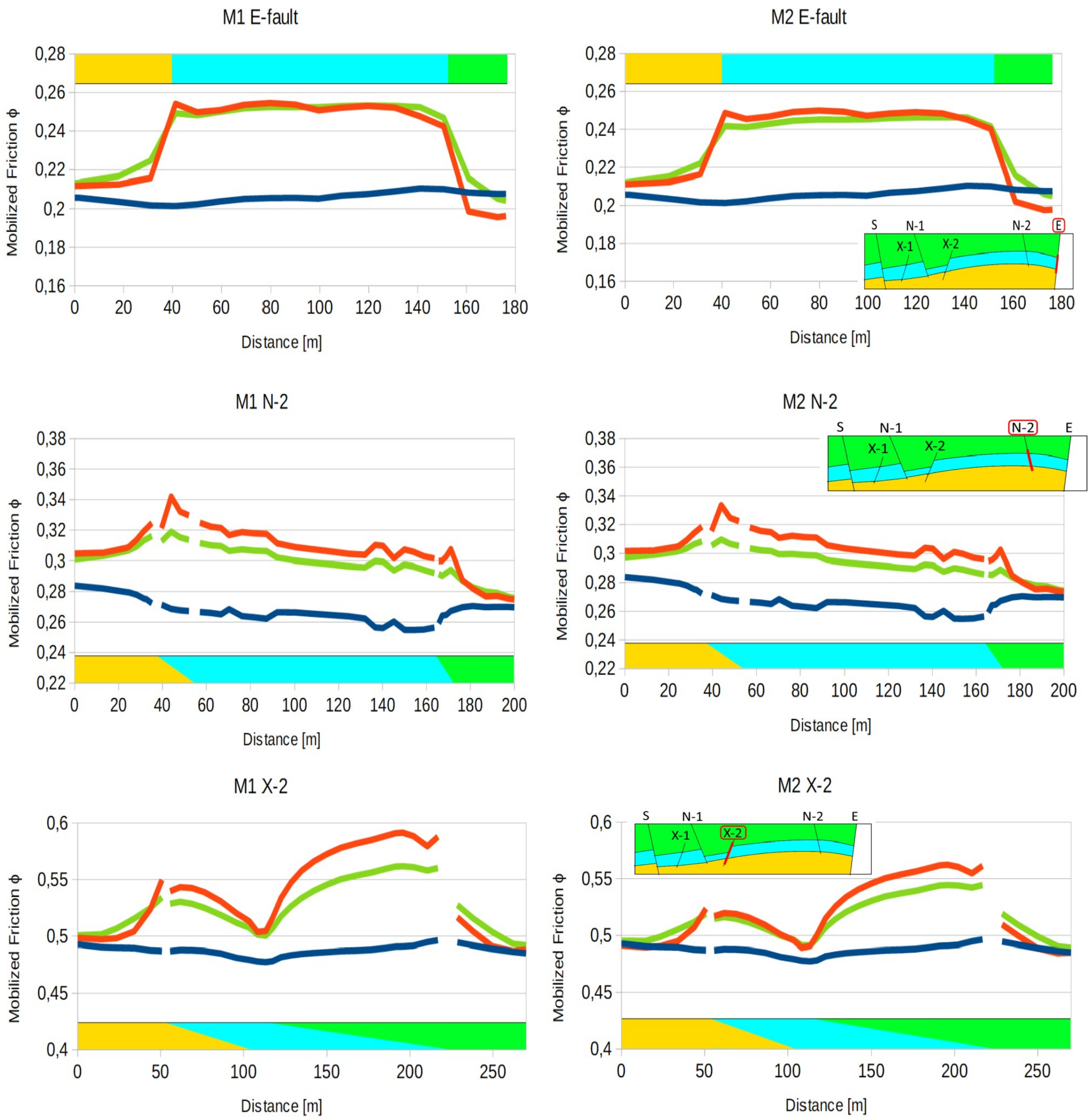

Fig.21 Mobilized friction along E-fault, N-2 and X-2 from both models M1 and M2$_{low}$ three different times: The initial time before the UHS (blue), the end of the injection (red) & the end of the resting phase (green). The location of the mobilized friction inside of the fault is indicated with the colours yellow (basement), turquoise (reservoir) and green (caprock). A small sketch of the storage structure helps to find the location.

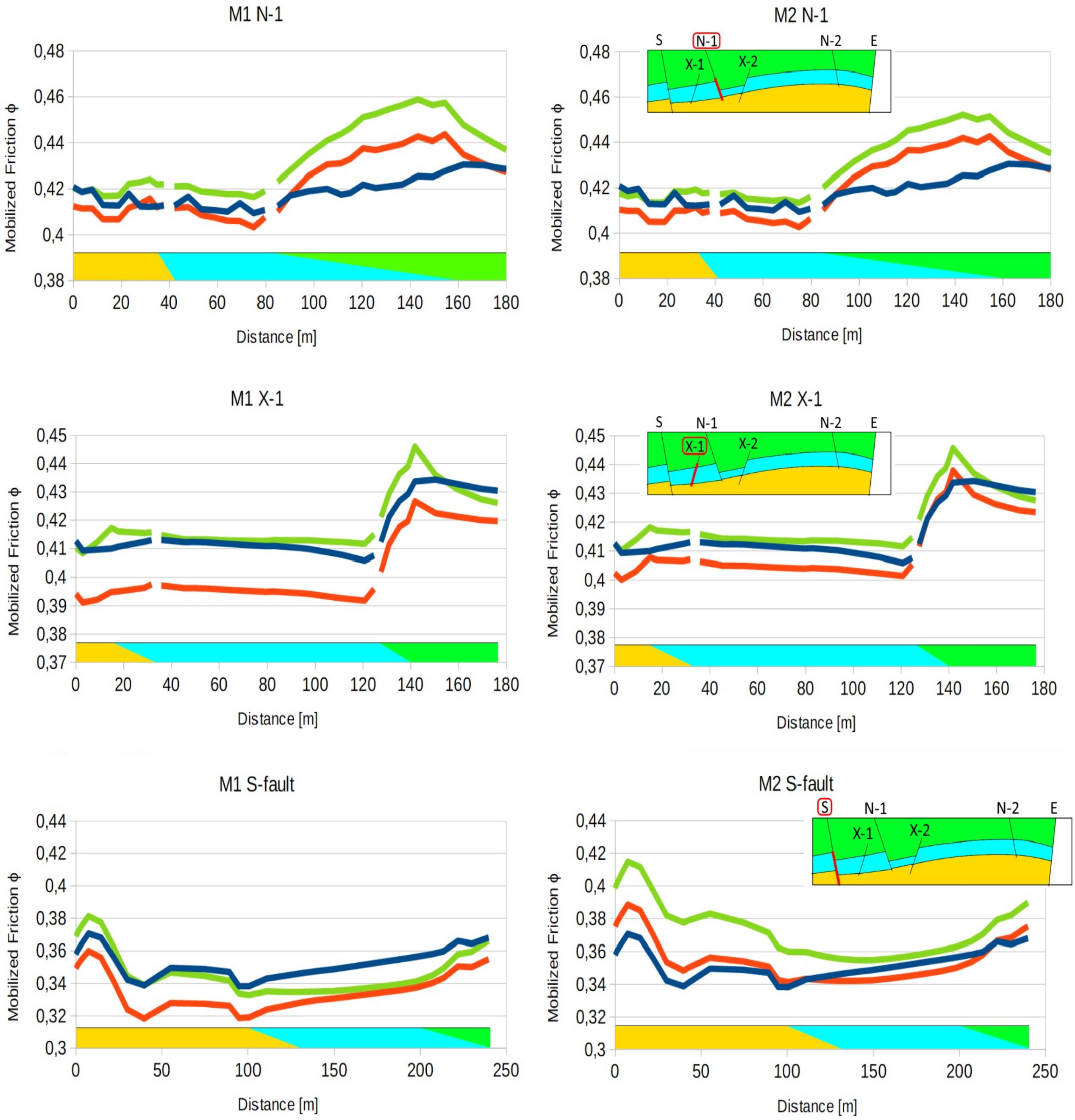

Fig.22 Mobilized friction along N-1, X-1 and the S-fault from both models M1 and M2$_{low}$ three different times: The initial time before the UHS (blue), the end of the injection (red) & the end of the resting phase (green). The location of the mobilized friction inside of the fault is indicated with the colours yellow (basement), turquoise (reservoir) and green (caprock). A small sketch of the storage structure helps to find the location.

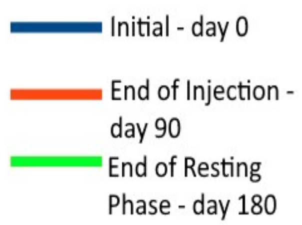

With the help of the Mohr circles at the different faults, the relation between the various stresses became clear. The Mohr circles at all faults besides the S-fault in both models at the fault location in contact with the reservoir showed all the same pattern, a relatively strong decrease in effective vertical- (N-2: 2.6 MPa in M1 & 2.4 MPa in $M2_{low}$) and a less strong decrease of effective horizontal stress (N-2: 1.9 MPa in M1 & 1.7 MPa in $M2_{low}$) (Fig. 23 & 24). As explained earlier, this occurred as horizontal stress could accumulate better as there was not much horizontal displacement. However, the vertical stress was transformed in our models mainly to a vertical displacement. Hence, effective vertical stress decreased stronger at the faults. The different reductions of both the effective horizontal- and vertical stress led to a shrinking of the Mohr circles, resulting in lower tangential stress in general. This again led to more stabilization. At the same time, the decreasing effective horizontal stress resulted in lower normal stress on the faults and consequently, more destabilization. The different ratios between the faults' normal- and tangential stress resulted in different stability. As the decrease in normal stress on most faults was significantly higher than the decrease in tangential stress, most faults got destabilized inside the reservoir. The reduction in tangential stress was indeed so low (N-2: 0.13 MPa in M1 & $M2_{low}$) relative to the stronger decrease in effective normal stress (N-2: 1.91 MPa in M1 & 1.75 MPa in M1) that its stabilizing effect played a minor role.

The decrease in normal stress arose from the liquid pressure increase mainly present inside the reservoir. As liquid pressure in model M1 was higher in the NE and central part of the model effective horizontal stress and thus normal stress at the faults decreased here stronger. At the same time as vertical displacement was stronger in model M1 in the NE and central part of the model also effective vertical stress decrease and thus tangential decrease at the faults was higher here. However, as explained before, normal stress decrease was remarkably higher than tangential stress decrease. Therefore, faults in model M1 in the NE and central part were more destabilized than in model $M2_{low}$.

In the SW of the models, the differences tended to be the other way around (Fig. 25 & 26). Liquid pressure in the SW was higher in model $M2_{low}$,which resulted in more horizontal stress and thus normal stress decrease at the faults ($M2_{low}$: S-fault in contact with reservoir: ~0.5 MPa; S-fault in baserock ~0.9 MPa) that led to a stronger destabilization of the S-fault in this area than in model M1 (M1: S-fault in contact with reservoir: ~0.1 MPa normal stress increase; S-fault in baserock ~0.2 MPa normal stress decrease).

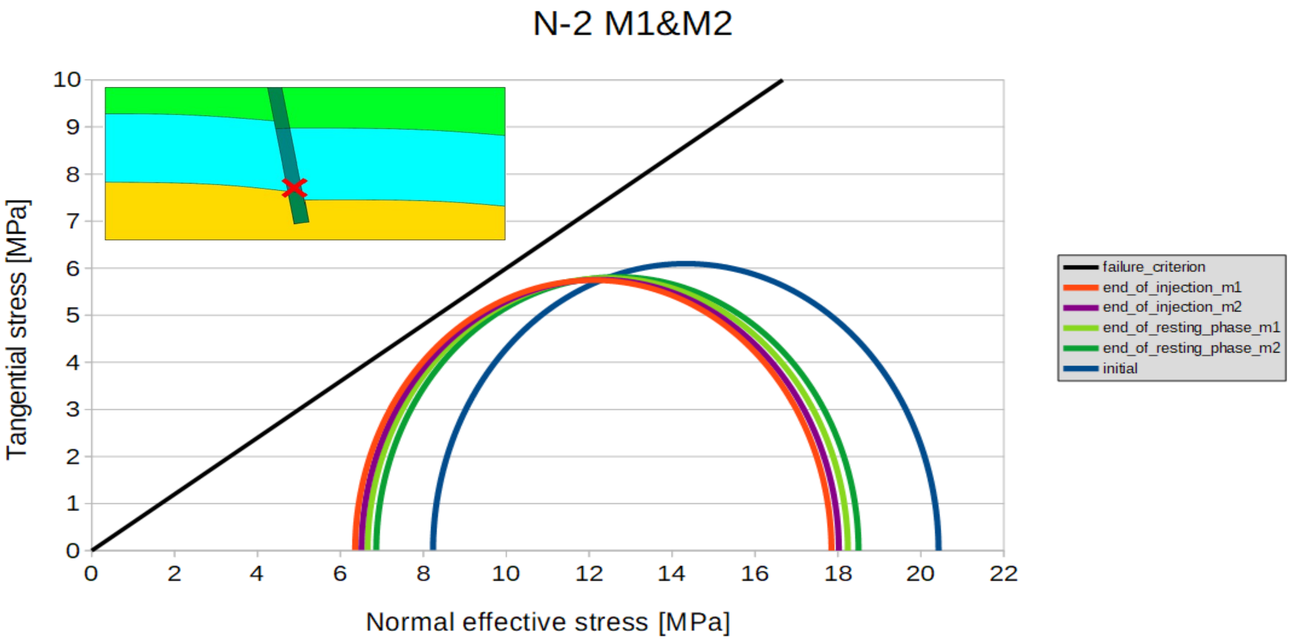

Fig. 23 Comparison between the Mohr circles of model M1 & M2$_{low}$ at fault N-2 (central part of the model). Effective normal stress is lower at the Mohr circle of model M1. Mohr circle at the end of injection of model M1 (red) & M2low (purple), at the end of the resting phase model M1 (light green) & M2low (dark green), initial Mohr circle (blue).

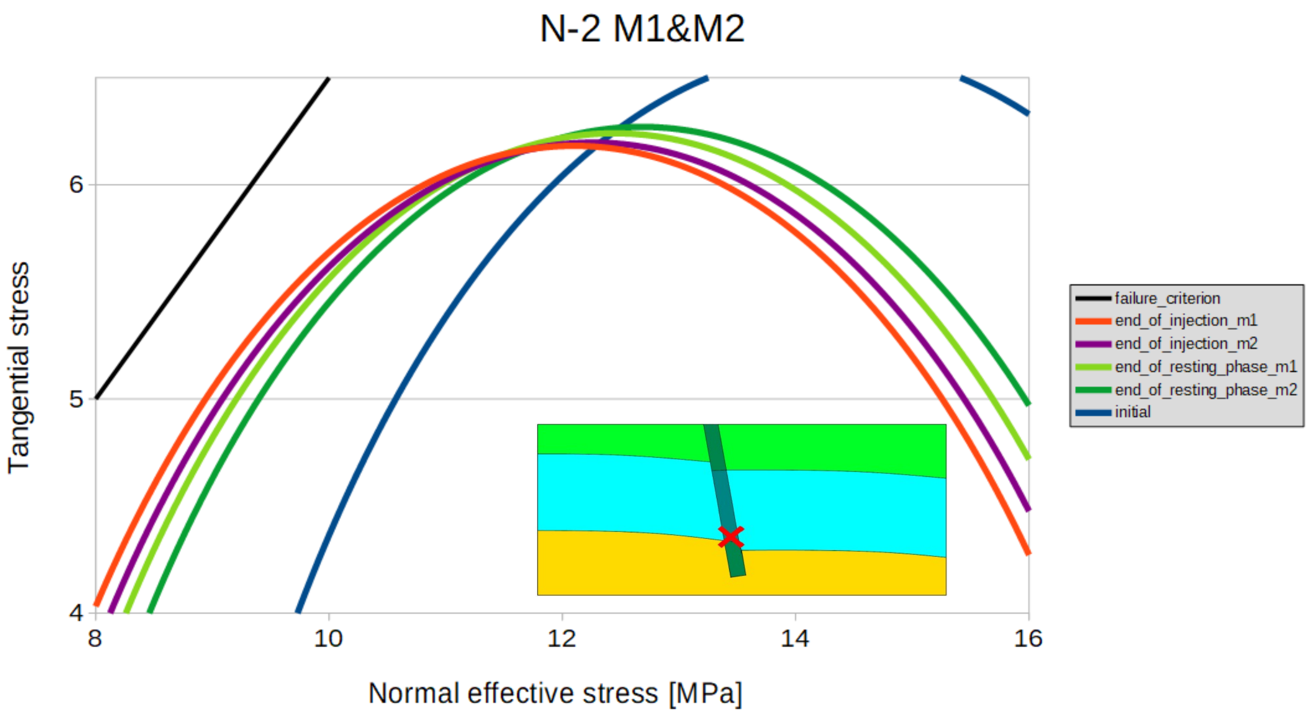

Fig. 24 Comparison between the Mohr circles of model M1 & M2$_{low}$ at fault N-2 (central part of the model), zoomed. Tangential stress is lower at the Mohr circle of model M1. Mohr circle at the end of injection of model M1 (red) & M2low (purple), at the end of the resting phase model M1 (light green) & M2low (dark green), initial Mohr circle (blue).

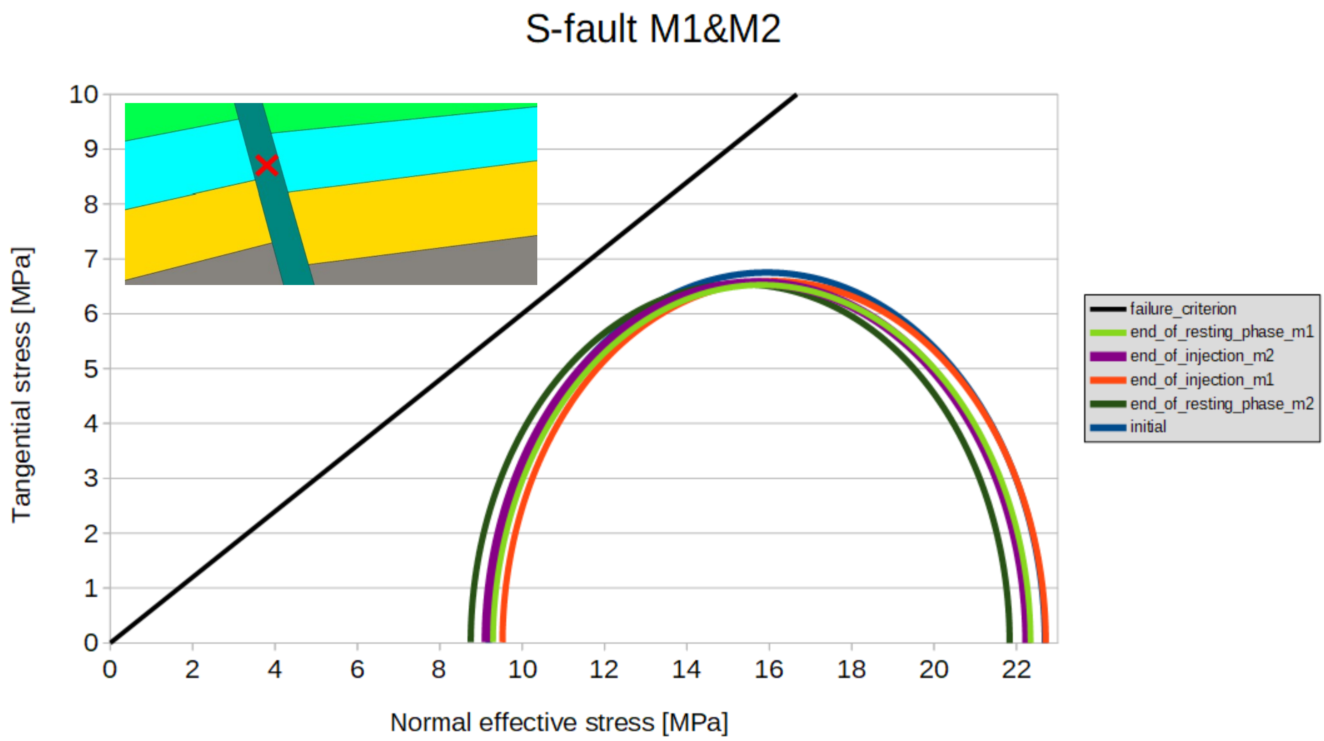

Fig. 25 Comparison between the Mohr circles of model M1 & M2$_{low}$ at the S-fault (SW of the model). Effective normal stress is lower at the Mohr circle of model M2low. Mohr circle at the end of injection of model M1 (red) & M2low (purple), at the end of the resting phase model M1 (light green) & M2 low(dark green), initial Mohr circle (blue).

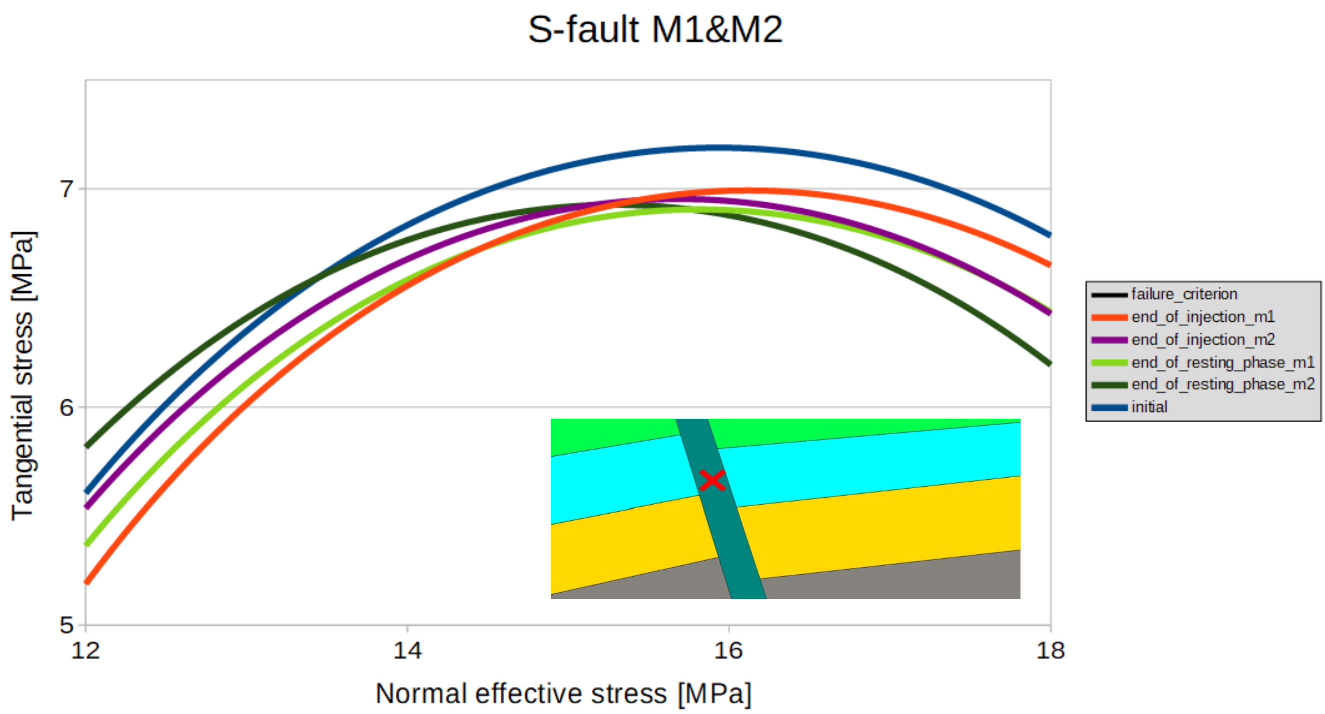

Fig. 26 Comparison between the Mohr circles of model M1 & M2$_{low}$ at the S-fault (SW of the model), zoomed. Tangential stress tends to be lower at the Mohr circle of model M2low. Mohr circle at the end of injection of model M1 (red) & M2low (purple), at the end of the resting phase model M1 (light green) & M2low (dark green), initial Mohr circle (blue).

The effective vertical stress of the E-fault, N-2 and X-2 inside the baserock increased usually slightly or did not decrease. At the same time, effective horizontal stress decreased slightly. Therefore, the tangential stress tended to increase slightly (E-fault: 0.02 MPa; N-2: 0.04 MPa & X-2: 0.04 MPa). This should have resulted from the compaction of the base unit beneath blocks 1 to 3. At X-2 and N-1 inside the baserock instead, tangential stresses decreased around 0.12 and 0.03, respectively. This is probably as the baserock in the SW of the model beneath blocks 4 to 6 was undergoing extension. Tangential stresses were slightly higher in model M1 beneath blocks 1 to 3, probably as the baserock got slightly more compressed in model M1 (~0.23 mm). However, as the stability of these parts of the faults in the basement is not much affected by the UHS, this difference between the models does not contribute to a different storage capacity.

The same is true for the parts of the fault inside of the caprock, as their mobilized frictions were relatively low. However, the Mohr circles at these faults inside the caprock behaved usually similar to the Mohr circles inside the reservoir. Their vertical- and horizontal stress decreased, as well as the tangential stress. Though, compared to the parts of the fault inside the reservoir they did approach failure envelope significantly less.

Over time, the mobilized friction increased during the injection at the E-fault, N-2 and X-2 in both models and at the S-fault in model $M2_{low}$ (Fig. 27 and 28). During the resting phase, mobilized friction dropped only at the fault X-2, N-2 and the E-fault in both models; at N-1, X-1 and the S-fault, it continued or started to rise during this phase. The shift of liquid pressure increase between the injection and resting phase from blocks 1 to 3 to blocks 4 to 6 was most likely responsible for these results. As liquid pressure increased during the injection mainly in blocks 1 to 3 faults got more unstable in these blocks. Given that, later at the resting phase, pressure dropped in blocks 1 to 3 but mainly increased in blocks 4 to 6, instability in blocks 1 to 3 decreased at the faults but increased further at blocks 4 to 6.

Furthermore, there was a shift in time when the mobilized friction of the faults began to rise. In model M1, mobilized friction increase occurred at the E-fault, N-2, X-2 and at the S-fault somewhat later than in model $M2_{low}$, depending on the fault's position relative to the injection well. The farther away from the well, the later the increase in mobilized friction occurred. The later increase in mobilized friction in model M1 can be explained as the liquid pressure was more restricted to an area as in model $M2_{low}$ because of the strain-dependent permeability in model M1 that was approximately radially decreasing from the well. In the reservoir with homogenous permeability though, liquid pressure could spread relatively fast over the whole reservoir, resulting in an early increase in mobilized friction at the faults.

However, at N-1, mobilized friction began to rise earlier in model M1 (~day 60), while at X-

1 it rose at the same time in both models (~ day 100), although liquid pressure reached these faults earlier in model $M2_{low}$. This is because in model $M2_{low}$ during the injection the relation between tangential and normal stress stayed approximately the same at faults N-1 and X-2. In contrast to that, this relation changed in model M1 at these faults as liquid pressure was higher in model M1 and therefore effective horizontal stress decreased more. Therefore, an increase in mobilized friction could be seen at these faults in model M1 but not in model $M2_{low}$ during injection.

Howsoever, the time for the maximum mobilized friction of all faults did not differ between the models (Time for max. mob. frict.: N-2 day 95; X-2 day 95; E-fault day 100; S-fault, X-1 and N1 day 180). This means that most instability at the faults is expected at the same time in both reservoir types, although the time when instability increase occurred differed.

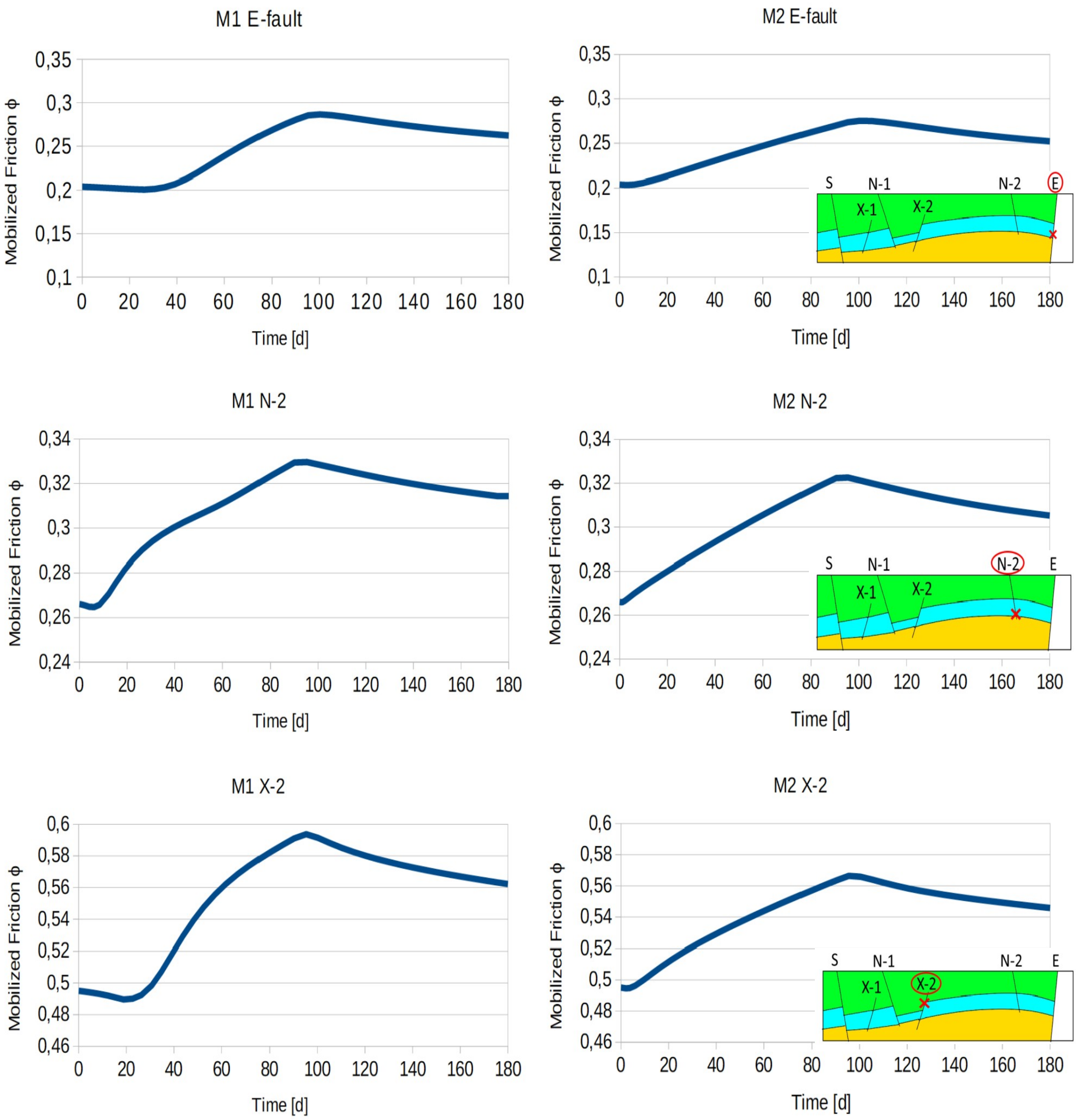

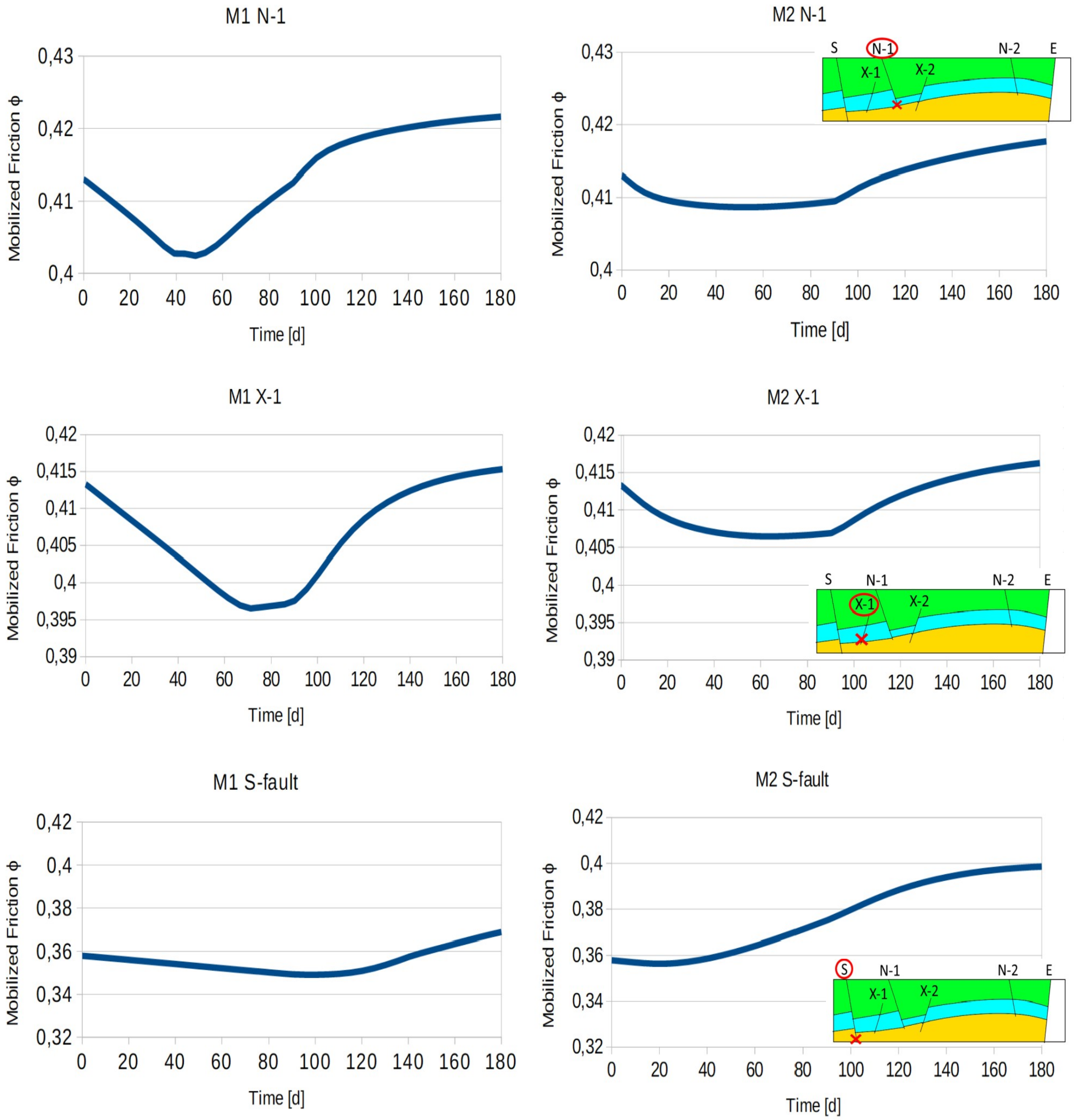

Fig.27 Mobilized friction over time at one location of each fault from both models M1 and $M2_{low}$. A small sketch of the storage structure helps to find the location.

The fault X-1 in both models and the S-fault in model M1 were the least affected faults during the UHS (Fig. 9 & 14). These faults and also N-1 at some parts got slightly more stabilized during the injection (~ 0.01). In the resting phase, X-2 in both models and the S-fault in model $M2_{low}$ reached a similar or lower mobilized friction to its initial value at most of the parts of the faults.

With the help of a Mohr circle at X-1, the relationship between tangential and normal stresses acting on the fault became clear (Fig. 28). During the injection tangential stress decreased (0.14 MPa) and effective normal stress slightly increased (0.06 MPa), which resulted in a more stabilized fault. During the resting phase, both effective normal- and tangential stress decreased by around 0.5 MPa and 0.2 MPa, respectively, which resulted in a similar stability as at the initial.

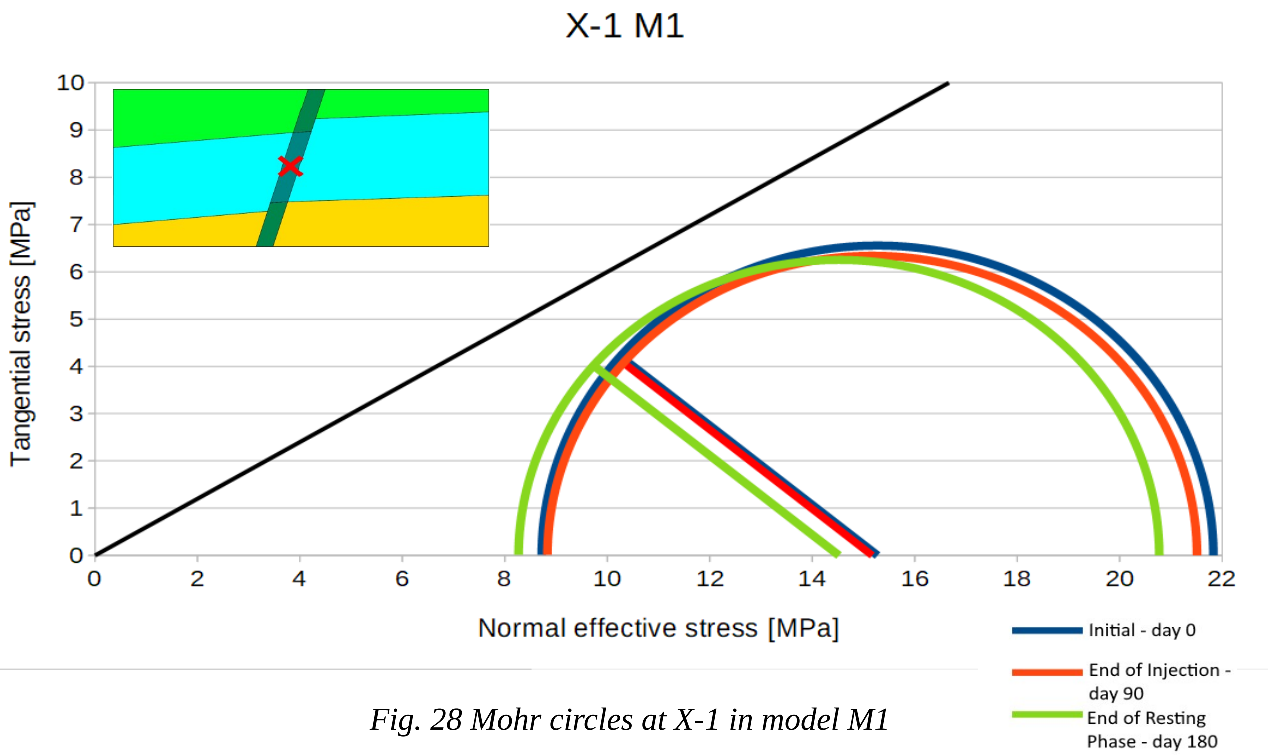

Fig. 28 Mohr circles at X-1 in model M1

Interestingly, the fault X-2 became more stable or unstable in both models relative to its initial state, depending on the location at the fault (Fig. 21, 29 and 30). In both models, the maximum mobilized friction (M1: 0.59; $M2_{low}$: 0.56) and thus maximum instability at X-2 was reached around the end of injection and in the upper part of the permeable part of the fault just before the transition to its low permeable part (Fig. 21). In the lower permeable part of the fault located in block 3, however, the fault was experiencing significantly less increase in mobilized friction during the UHS (lower part: 0.02 ($M2_{low}$) & 0.04 (M1); upper part: 0.06 ($M2_{low}$) & 0.09(M1)). As in all other faults, parts inside the reservoir at both parts of X-2, a strong decrease in effective vertical- and a less strong decrease of effective horizontal stress was present (Fig. 29 and 30). As explained earlier, this generally occurs as horizontal stress can accumulate better than vertical stress when there is less horizontal- than vertical displacement. However, the resulting decrease in tangential- and normal stress at the fault occurred to a different ratio at the different parts of the fault. At the upper part of X-2, the effective horizontal stress and thus normal stress acting on the fault decreased around 1 MPa more (Fig. 29) and the tangential stress decreased around 0.1 MPa less than in the lower part. As the shrinking in effective horizontal stress was relatively strong at the upper part of X-2, the Mohr circle moved relatively intensely to the failure envelope. The tangential stress decreased more at the upper part of X-2 probably as there was more vertical displacement (Fig. 18). The strong decrease in effective horizontal stress that was mainly responsible for the strong decrease in stability instead occurred probably as there was a stronger horizontal displacement compared to the lower position of the fault. The reason for the stronger horizontal displacement at the upper part of X-2 is a phenomenon occurring at faults with an offset that was observed by Vilarrasa et al. (2016) similarly. During an UGS the reservoir expands due to overpressure. Thereby, the caprock that is less stiff than the reservoir gets relatively strongly compressed, resulting in a horizontal displacement of the unit and a relatively strong decrease of effective horizontal stress and thus normal stress at the fault. This again results in a more destabilized fault. Therefore, at the location of X-2 between caprock and reservoir, the mobilized friction was the highest. The strong compression of the caprock could also be seen in the results of horizontal displacement at X-2 (Fig. 19)

At the small reservoir-reservoir interface, though, both sites of the fault were surrounded by stiff reservoir rock that accumulated more horizontal stress. Therefore, the fault did get less unstable. Also, at the reservoir-baserock interface, destabilization was not so strong, probably as the baserock was slightly stiffer than the reservoir and as liquid pressure increased less here.

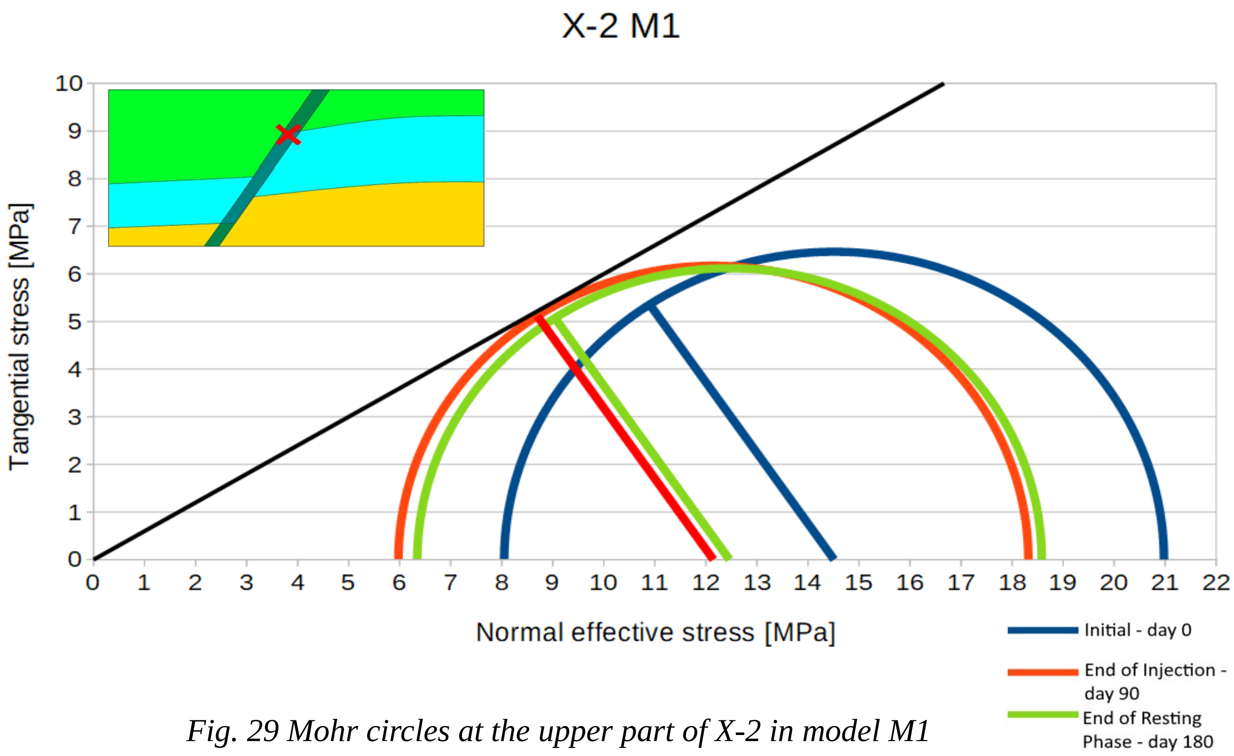

Fig. 29 Mohr circles at the upper part of X-2 in model M1

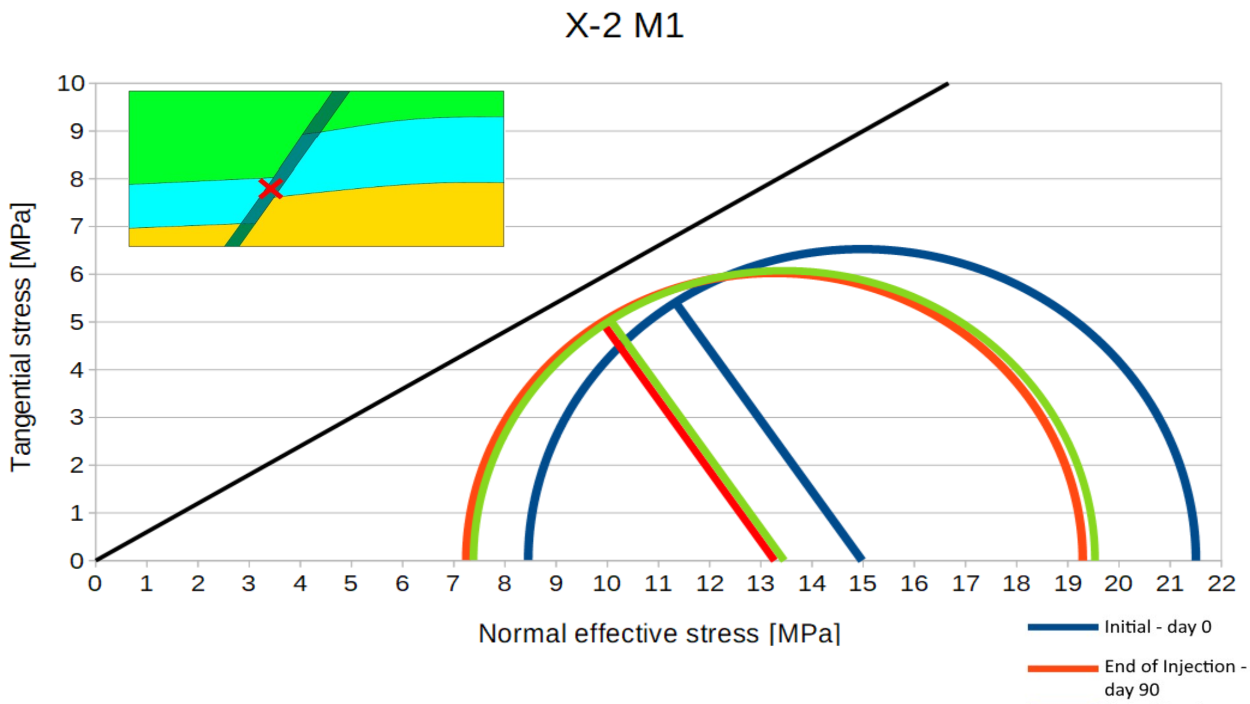

Fig. 30 Mohr circle at the lower part of X-2 in model M1

Also, at the fault N-1 in both models, it could be seen that at the upper part of the fault's location between reservoir and caprock the mobilized friction increased more than in other parts (Fig. 22, 31 and 32). This occurred probably because of the same reason, the caprock deformed relatively strongly in horizontal direction because of its low stiffness, which led to less horizontal stress accumulation thus more destabilization. Thus the finding of Vilarrasa et al. (2016) could be confirmed, in a storage structure with a relatively plastic caprock and strong offsets, the hanging wall of a fault located at an offset is more in danger of slipping than the foot wall of the fault.

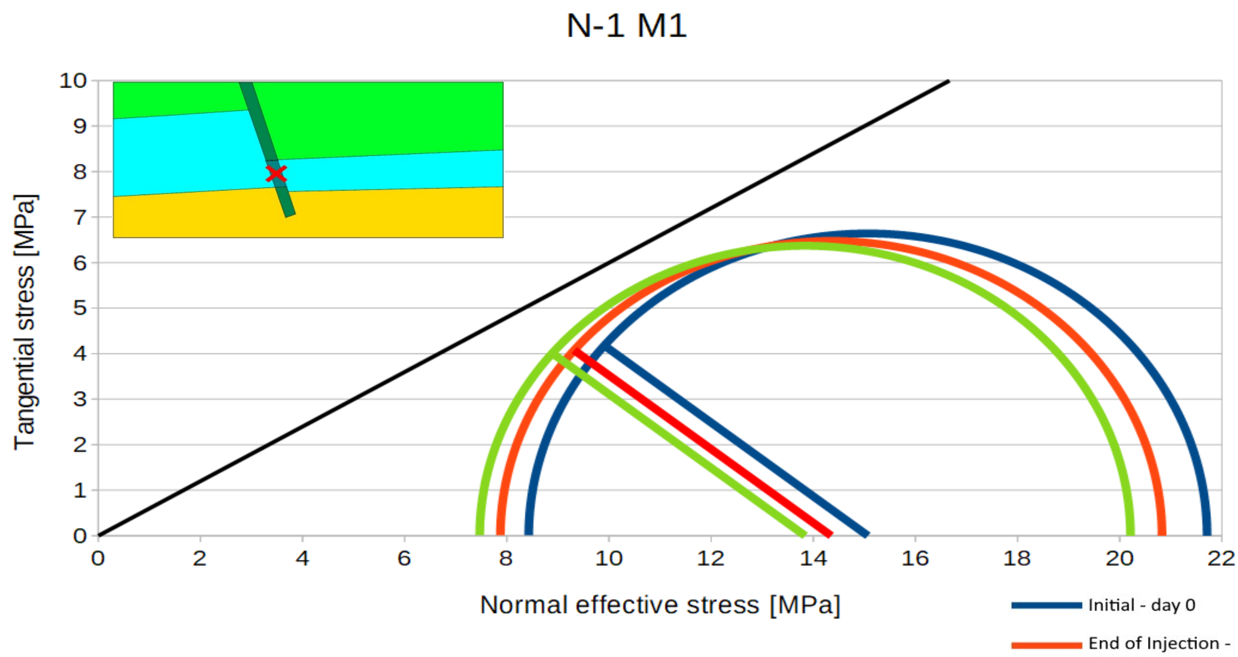

Fig. 31 Mohr circles at the upper part of N-1 in model M1

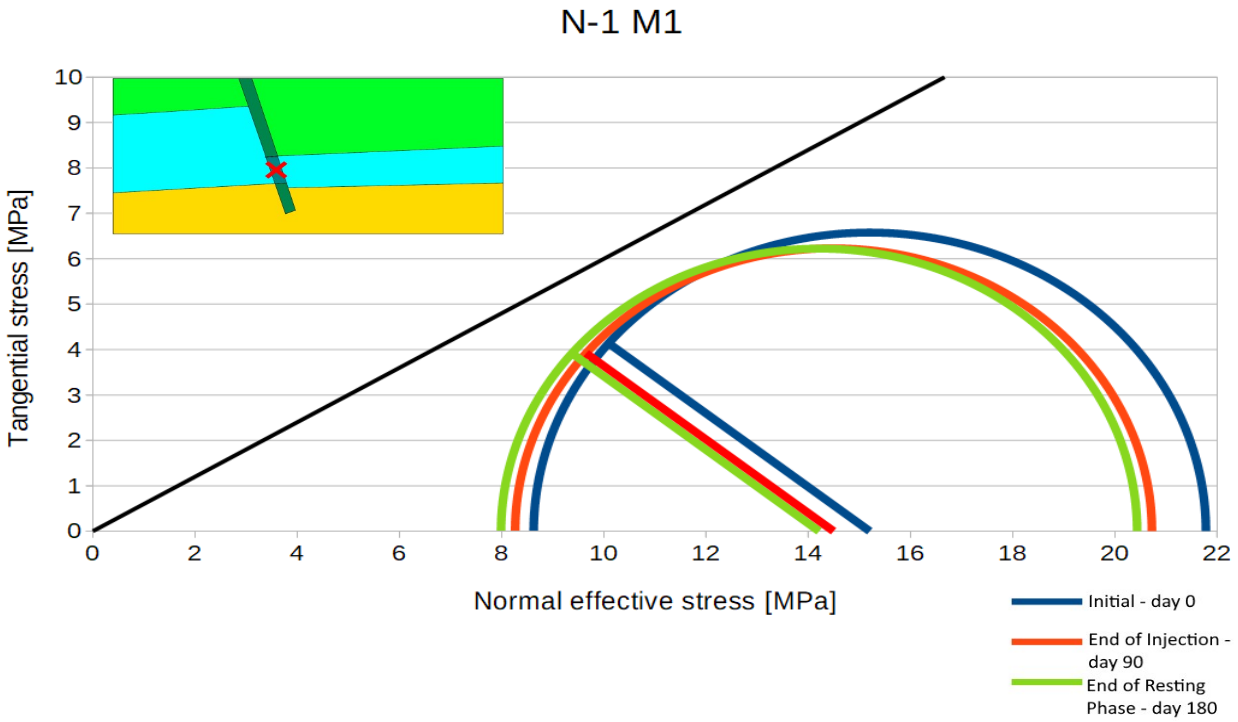

Fig. 32 Mohr circles at the lower part of N-1 in model M1

By comparing the Mohr circles of X-2 (Fig. 29) and the E-fault (Fig. 33), it became clear that both circles were close to the failure envelope although their mobilized frictions of the faults differed significantly. This is because of their different dip angles. X-2 has a dip angle (62°) where the resulting normal- and tangential stresses brought the fault close to the failure envelope. If the angle would be smaller or higher, the fault would be more stable. Instead, the E-fault instead had a relatively high dip angle (82.5°) which resulted in a relatively low tangential- to normal force ratio.

Interestingly, the decrease in normal stress at X-2, E-fault and also N-2 (Fig. 34) was not too different on the location where their maximum mobilized friction was present. The decrease of normal stress was 2.2 MPa at X-2, 2.05 MPa at N-2 and 1.9 MPa at the E-fault at the end of injection although, dip angle (X-2 = 62°; N-2 = 79°; E = 82.8°), distance to the injection well (X-2 = ~717 m; N-2 = ~316 m; E = ~828 m) and transmissivity (X-2 and N-2 = high permeable (3.5E^{-15} m^2); E = low permeable (1E^{-18} m^2)) between the faults differed strongly. Vilarrasa et al. (2016) and Wu et al. (2021) state that the majority of the instability tends to occur on low permeable faults. This could explain why the E-fault had a similar decrease in normal stress as X-2 and N-2, although its position was further distant from the injection well and its dip angle was higher. The high dip angle and position at the strong offset at the relatively elastic caprock of X-2 and the close position to the well of N-2 instead can explain why these faults had a similar decrease in normal stress although they are permeable. Both previous paragraphs underline that not just the type of permeability but also the characteristics of the faults can have a huge influence on the storage capacity of a reservoir. Furthermore, the current stress state is important for fault slip. As at *Hontomín* an active extensional N-S trending field is present (Pérez-López et al., 2020) X-2 and the E-fault would be more probable to slip.

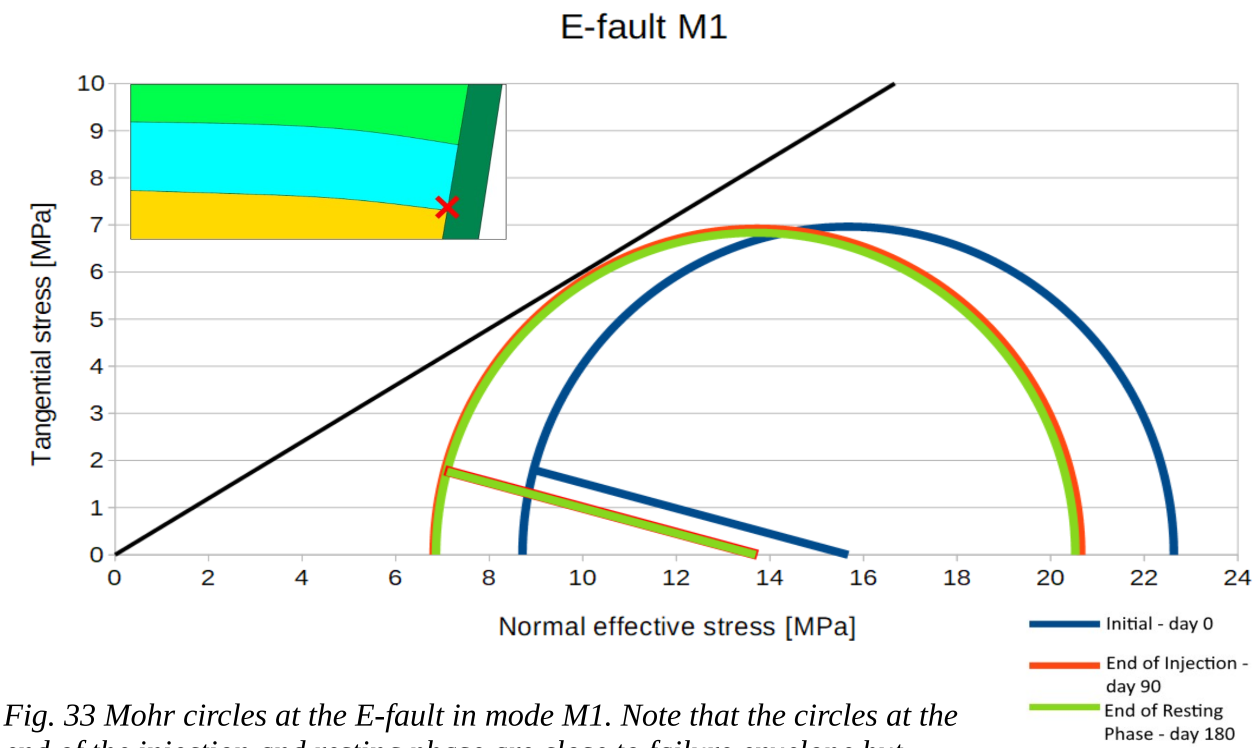

Fig. 33 Mohr circles at the E-fault in mode M1. Note that the circles at the end of the injection and resting phase are close to failure envelope but the E-fault (lines inside the circles) is relatively far away from failure envelope.

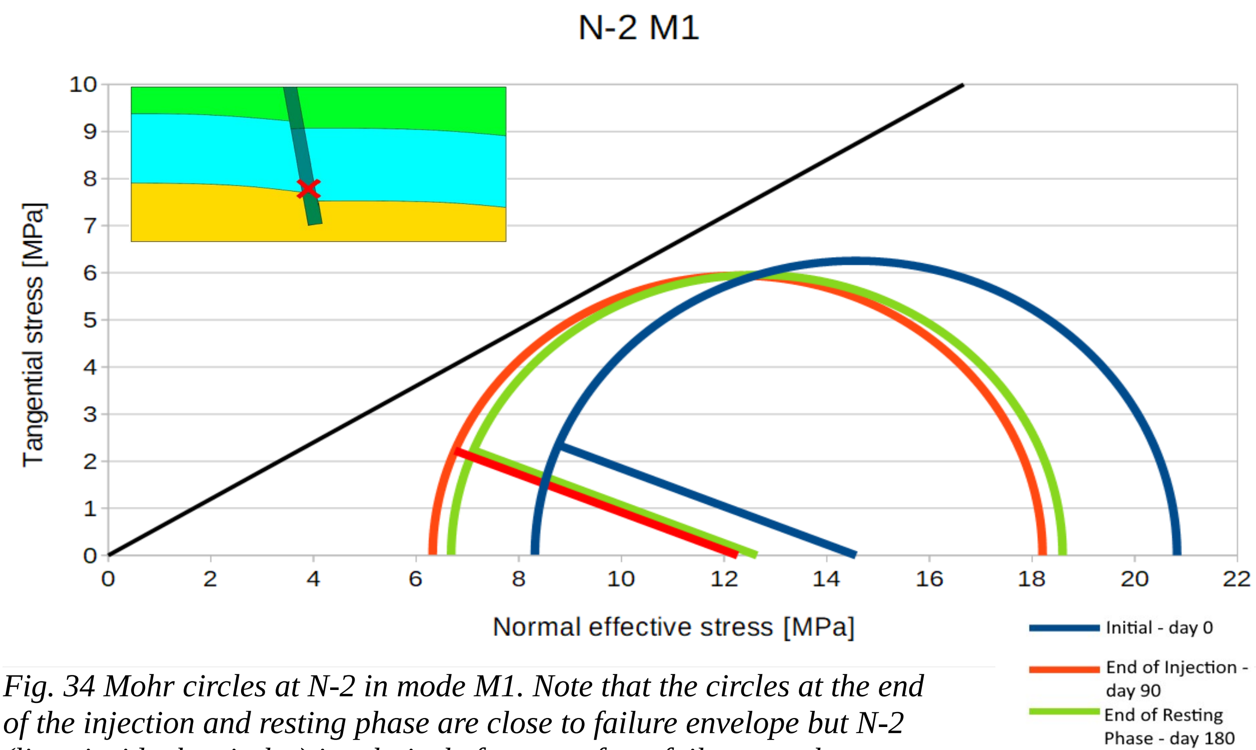

Fig. 34 Mohr circles at N-2 in mode M1. Note that the circles at the end of the injection and resting phase are close to failure envelope but N-2 (lines inside the circles) is relatively far away from failure envelope.

Even though liquid pressure increase tended to be less strong in model $M2_{low}$, its effect covered a greater area than in model M1 and could therefore reach the S-fault in a higher amount (Max: M1 = 18.2 MPa & $M2_{low}$ = 18.9 MPa). Thus, this fault was relatively strongly destabilized in model $M2_{low}$ (Max mob. fric. Increase = 0.04) but was significantly less affected in model M1 (Max mob. fric. Increase = 0.01) and even became, besides its lower part, slightly more stable (Fig. 22 and 27). In the lower part of the S-fault, the majority of instability occurred in both models as most liquid pressure increases took place there that reduced the normal force acting on the fault in both models (Fig. 35 & 36). However, this reduction was stronger in model $M2_{low}$ (M1: 0.2 MPa; $M2_{low}$: 0.9 MPa) as liquid pressure rose more during UHS in this model. Additionally, in model $M2_{low}$, the tangential force increased (0.1 MPa), which leads to further destabilization.

The importance of the difference in instability of the S-fault between the models becomes clear in the reservoir at *Hontomín*. As the S-fault is probably permeable (Ogaya et al., 2014), induced stress changes could more easily travel down to the basement, inducing deep seismicity (Fan et al., 2019). However, as the stability of X-2 was the limiting factor to the storage capacity of H_2 in our models and the S-fault was under the limit of fault slip during the whole simulation in both models, the stability of the S-fault did play a minor role. Furthermore, the nowadays tectonic field studies (Pérez-López et al., 2020) indicate that the S-fault would be stable at *Hontomín*.

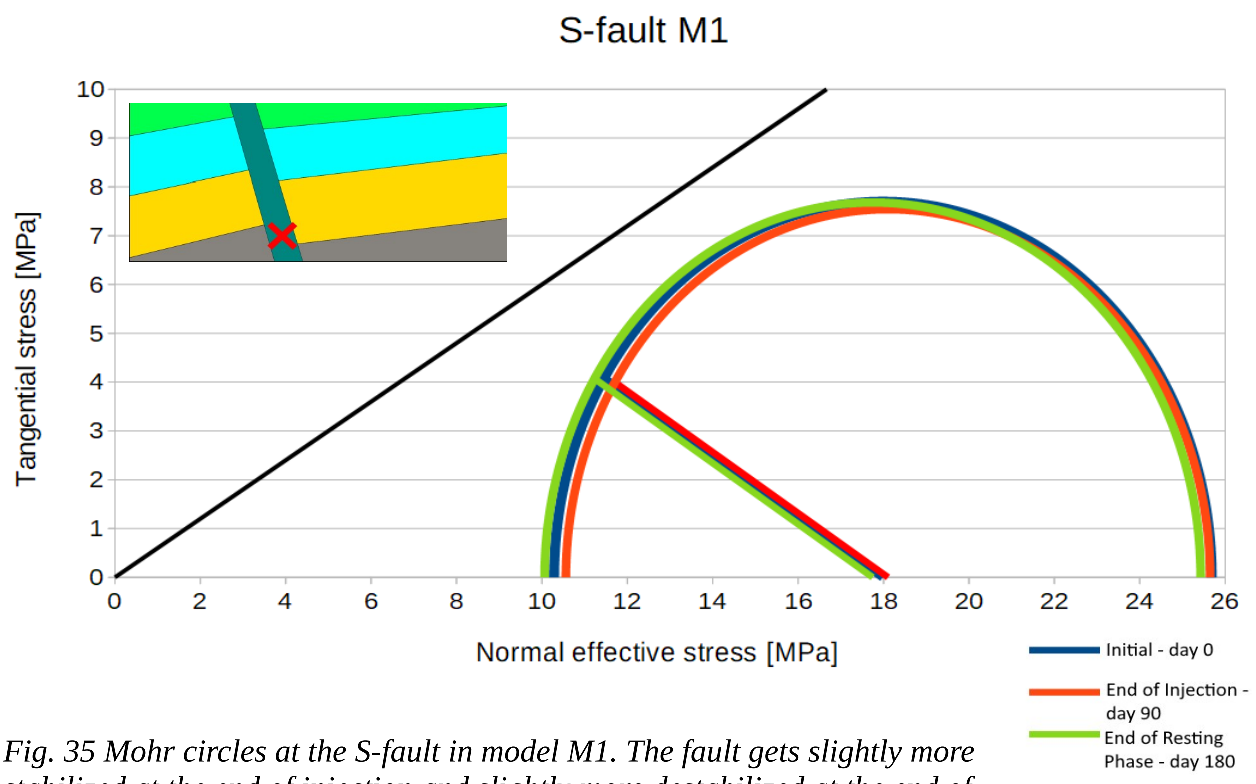

Fig. 35 Mohr circles at the S-fault in model M1. The fault gets slightly more stabilized at the end of injection and slightly more destabilized at the end of the resting phase.

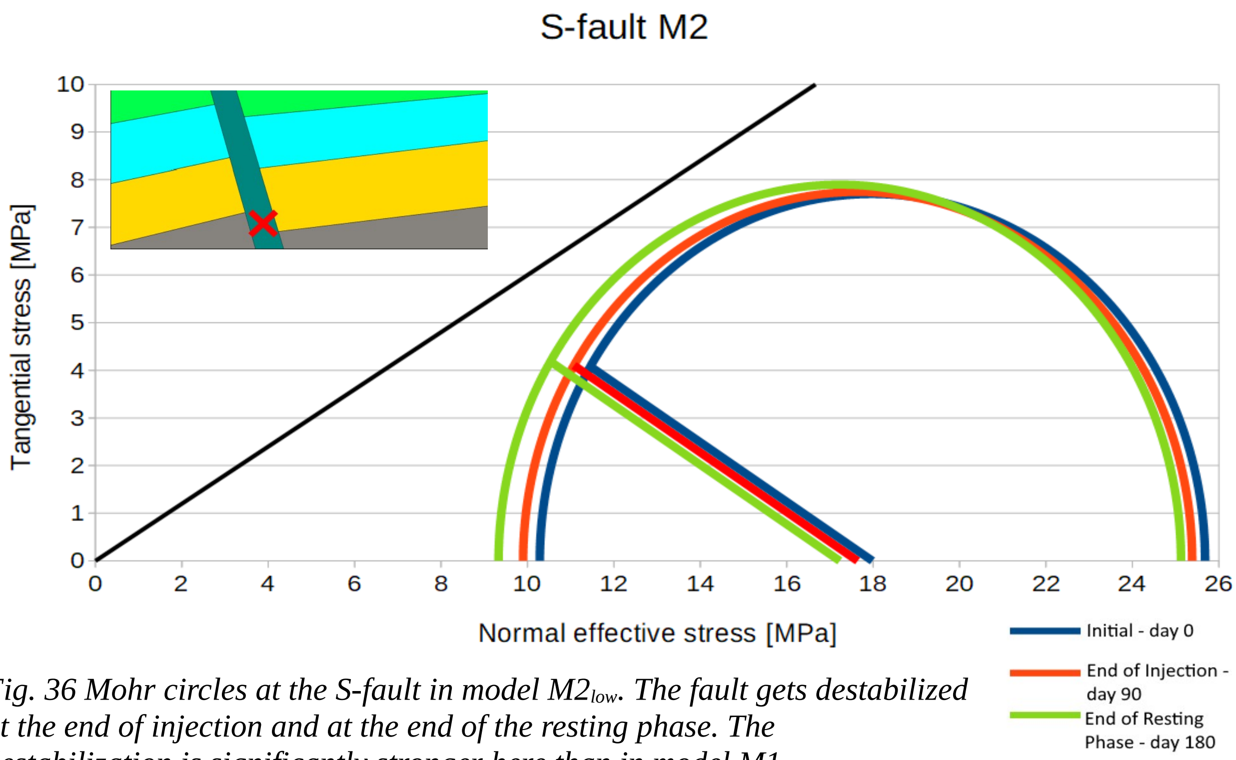

Fig. 36 Mohr circles at the S-fault in model M2$_{low}$. The fault gets destabilized at the end of injection and at the end of the resting phase. The destabilization is significantly stronger here than in model M1.

To summarise this, while in a reservoir with strain-dependent permeability during the UHS faults are more destabilized that lie relatively close to the injection well, in a reservoir with constant permeability faults far away from the injection point tend to be more at risk to be destabilized. However, liquid pressure and thus instability increase are the strongest close to the injection point in both reservoirs but stronger in the reservoir with strain-dependent permeability (Fig. 6). This means that faults close to the injection point are more at risk of fault slip in both reservoir types but more in a reservoir with strain-dependent permeability. Therefore, it is assumed that in a reservoir with variable permeability faults are generally more likely to undergo more instability increase than a reservoir with constant permeability. This means that the storage capacity of reservoirs with variable permeability usually should be smaller if no relatively far distant permeable fault that is critically stressed or is reaching to the basement is present.

5.6 Storage Capacity of Both Reservoir Types

With the geomechanical modelling it was possible to reveal the upper limit of the storage capacity of both models, M1 and $M2_{high}$. The model with strain-dependent permeability M1 has a smaller storage capacity than the model with constant permeability $M2_{high}$, as deduced from the fault stability analysis. According to the results, the injection rate for model M1 to ensure a safe UHS over a year was 0.00013 kg/s/m for a period of 90 days of injection. This is equivalent to 1010.88 tonnes ($5 \cdot 10^8$ mol) of total gas and 505.44 tonnes ($2.5 \cdot 10^8$ mol) of H_2 considering a 1km long horizontal well and 50% cushion gas. Assuming that a 4% hydrogen gets lost due to diffusion and solution (Carden & Paterson, 1979), 485.22 tonnes ($\sim 2.34 \cdot 10^8$ mol) of H_2 should still be possible to be withdrawn. However, in model $M2_{high}$, a significantly higher amount of H_2 was possible to store safely before reaching approximately the same maximum instability at the fault X-2 as in model M1. The injection rate for model $M2_{high}$ to ensure a safe UHS over a year was 0.00019 kg/s/m for a period of 90 days of injection. This represents a 46.15% higher injection rate than in model M1 and 1477.44 of total gas ($\sim 7.3 \cdot 10^8$ mol) considering a 1km long horizontal well. After subtracting the cushion gas (50%) (738,72 tonnes) and losses due to diffusion and solution (4%) 709.17 tonnes ($\sim 3.5 \cdot 10^8$ mol) of gas should be possible to withdraw.

As more H_2 was possible to be stored, also the gas plume spread in model $M2_{high}$ to a greater extent consisting of 107 x 38 m size at the end of the injection and 142 x 40 m at the end of the resting phase. The gas saturation of the plume in $M2_{high}$ is very similar to the saturation in model $M2_{low}$. Instead, the gas pressure was with 19.2 MPa at the end of injection and with 17.6 MPa at the end of the resting phase from 0.8 to 1.4 MPa higher as in model M1 and $M2_{low}$, respectively. Also, liquid pressure was remarkably higher in model $M2_{high.}$ Its maximum value lay around 19.9 MPa at the end of injection and 19.4 MPa at the end of the resting phase and was therefore 0.9 to 1.3 MPa higher as in model M1 and $M2_{low}$. (Fig. 37)

Despite these differences, the fault X-2 was still the limiting factor in model $M2_{high}$. The mobilized friction of all other faults was still significantly beneath 0.6. Furthermore, caprock fracturing was also in model $M2_{high}$ beneath the caprock fracturing limit although the increase in liquid pressure was relatively high (~5 MPa). Maximum horizontal- and vertical displacement (4mm and 11mm) lay somewhat higher than in model M1 and $M2_{low}$ but shear failure should have been still inhibited.

However, by comparing $M2_{high}$ with M1 it became clear that while the maximum mobilized friction was approximately the same at X-2 it was around 0.02 higher in model $M2_{high}$ at both N-2 and the E-fault. Also, the Mohr circle of N-2 (Fig. 38) was closer to failure envelope in model $M2_{high}$ than in model M1. That is most probably because that X-2 was compared to N-2 located relatively far away from the injection point. Therefore, an increase in injection rate should have been more noticed at N-2. The low permeability of the E-fault, on the other hand, and the strong liquid pressure increase in model $M2_{high}$ instead should have led to the stronger increase in destabilization although, the E-fault is farther away from the injection well as X-2. The Mohr circles at the E-fault and X-2 showed that the general destabilization at the E-fault is even stronger than at X-2 as it surpassed the failure envelope (Fig. 39). Only the high angle of the E-fault ensured that the fault did not slip.

Thus, if the E-fault would have a lower angle, it could be the limiting fault for the maximum amount of storable H_2 in model $M2_{high}$. As this fault seems to be stronger affected by an increase in injection rate of H_2 than X-2 this would mean that, if the E-fault would be the limiting factor, the differences in storable H_2 between model M1 and $M2_{high}$ would be somewhat less great. This would also be true if the limit of caprock fracturing would be lower. This underlines that the result that in a reservoir with constant permeability, the amount of storable H_2 is 1.46 times higher than the storable amount of H_2 in a reservoir with variable permeability cannot be generalized. This result is true in specific for our models. However, it is shown that in a reservoir with constant permeability, the storage capacity is probably higher than in a reservoir with strain-dependent permeability if not a far distant fault like the S-fault is the limiting factor. Furthermore, our results underline that the storable amount of H_2 can be not just slightly but much extensive in a reservoir with constant permeability.

It is also assumed that the case that a reservoir with strain-dependent permeability is better suited for an UHS than a reservoir with constant permeability is not very probable. In this case, all faults relatively close to the injection well should not be at risk of slip during the whole UHS, whereas a far distant fault should be critically stressed so that a low increase in liquid pressure could lead the fault to slip. This could be possible if the close faults would be permeable and would be more or less vertical, whereas the far distant fault could be low permeable and would have a relatively steep angle that brings the fault more easily to failure.

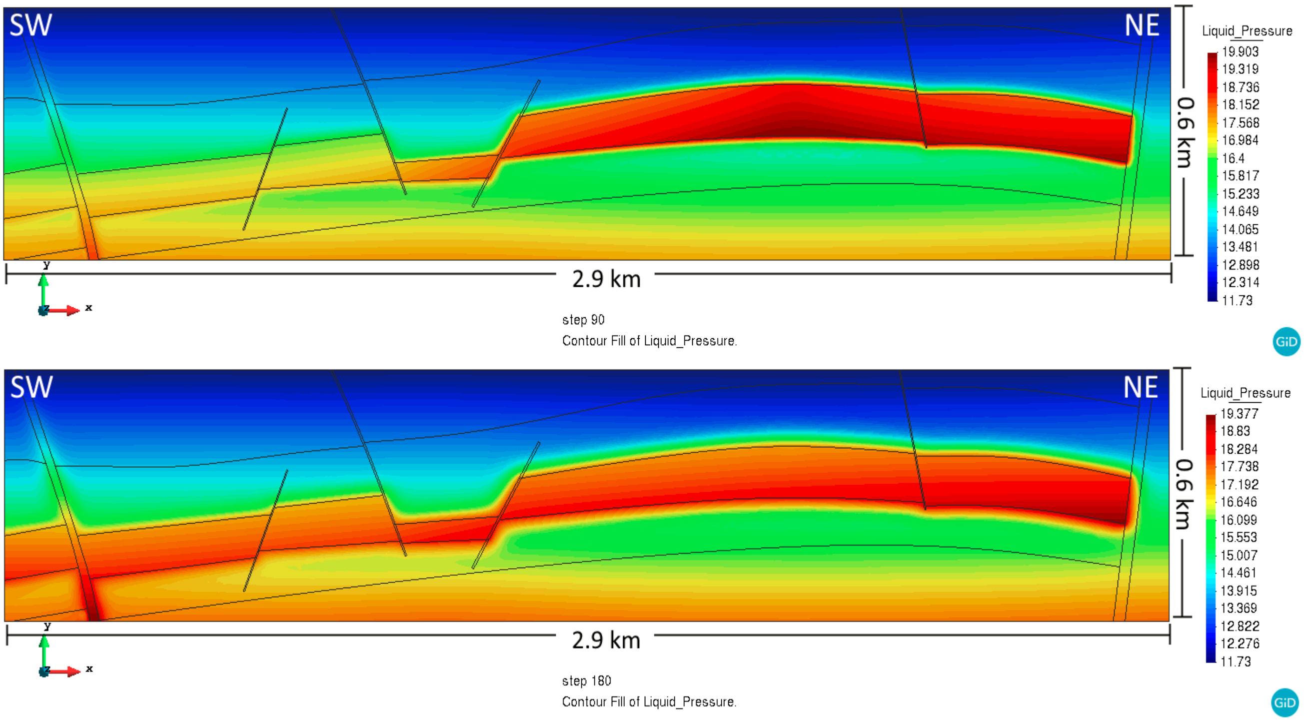

Fig. 37 Liquid pressure [MPa] in model M2$_{high}$ at the end of injection (day 90) upper image & the end of the resting phase (day 180) lower image.

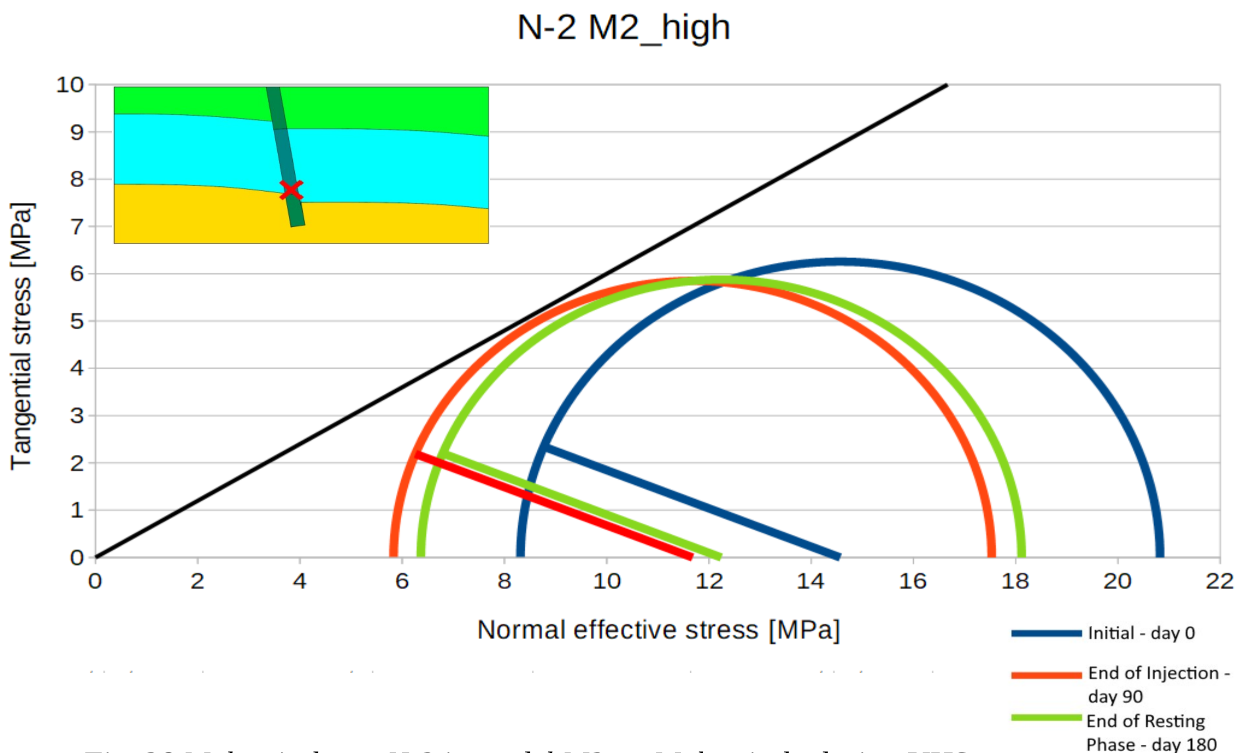

Fig. 38 Mohr circles at N-2 in model M2$_{high}$. Mohr circle during UHS is significantly closer to failure envelop as in model M1.

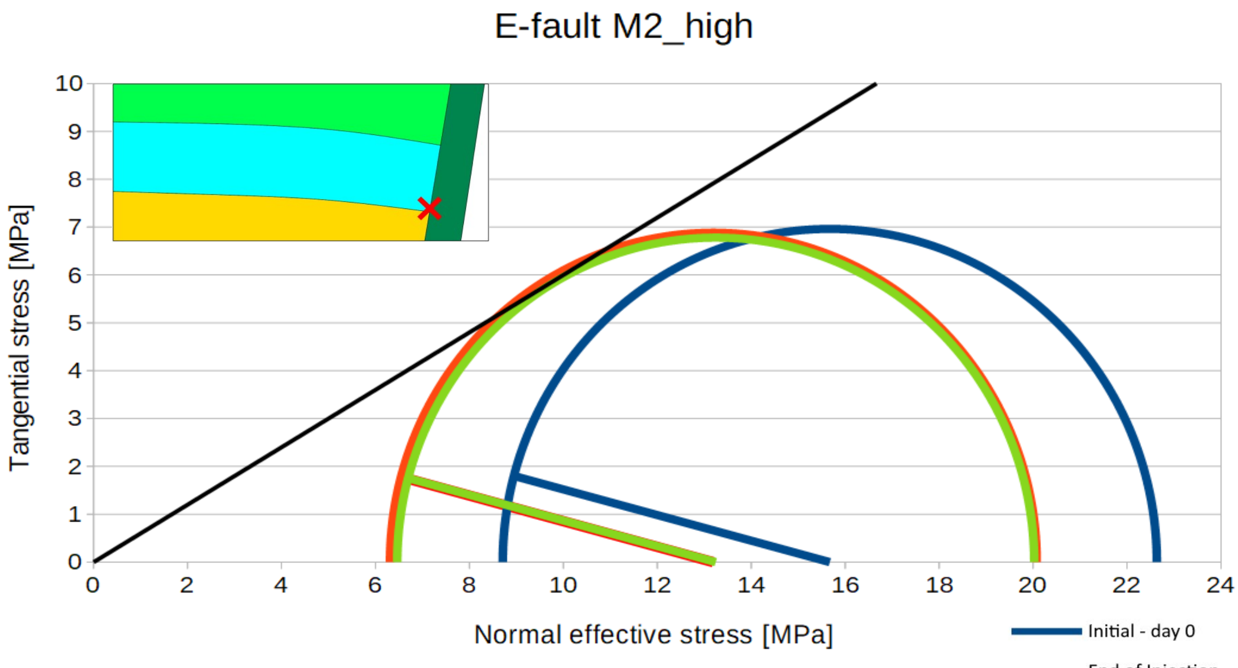

Fig. 39 Mohr circles at the E-fault in model M2$_{high}$. Mohr circle during UHS is significantly closer to failure envelop as in model M1. At the end of injection, the circle even surpasses failure envelope.

5.7 Comparison to Previous Models

In our models, the pressure increase inside the gas plume was comparable to that in de Dios et al. (2019). However, pressure increase in the reservoir and outside of the gas plume was remarkably higher in our models (~4-5 MPa) compared to the work of de Dios et al. (2019) that just detected a pressure increase of around 0.5 MP. This could be explained because de Dios et al. (2019) modelled an injection of a significantly lower amount of CO_2 (58 to 168 tonnes / $1.3 \cdot 10^6$ to $3.8 \cdot 10^6$ mol). However, also the pressure increase in our models was significantly higher than in the models of Sohal et al. (2021) which merely detected a pressure increase of around 0.3 MPa, although the amount of injected CO_2 in their study (300,000 tonnes CO_2 / ~ $6.8 \cdot 10^9$ mol) is significantly higher than the amount of injected gas we used (~ 1011-1477 tonnes H_2 / ~ $2.34 \cdot 10^8$-$3.5 \cdot 10^8$ mol). It is also surprising that their pressure increase was still somewhat lower than the pressure increase in the models of de Dios et al. (2019), where way less CO_2 was injected.

The main reason for the differences in the models is probably not just the different amounts of injected gas but the different representations of the reservoir. The total permeability in our model M1 was represented as a combination of matrix- and fracture permeability, and lied around $9.27 \cdot 10^{-15}$ m^2 during the UHS operation and the total permeability in model M2 was just represented with a constant matrix permeability of $9.27 \cdot 10^{-15}$ m^2. However, the fractures and matrix were represented in two different units in the models of de Dios et al. (2019) and Sohal et al. (2021). While the matrix permeability in Sohal et al. (2021) was the same we used for calculating the total permeability in our model M1, the fracture permeability was significantly higher ($2.37 \cdot 10^{-13}$ to $3.55 \cdot 10^{-13}$ m^2) than the total permeability in both our models. The fractures were thus more able to dissipate the pressure in the models of Sohal et al. (2021). De Dios et al. (2019) instead used similar values for fracture permeability as our total permeability, but the amount of injected gas was substantially lower. These two differences in the models of Sohal et al. (2021) and de Dios et al. (2019) could explain the different pressure increase observed in the reservoir. However, it is still remarkable that the pressure inside the gas plume in our work was similar to that reported in de Dios et al. (2019), but the liquid pressure outside the plume was significantly higher in our model.

Finally, our work showed that it was important to include the set of N- and X-faults detected by Alcalde et al. (2014), which were not included by Sohal et al. (2021) and de Dios et al. (2019), as the X-2 fault limited the storage capacity of the reservoir. Furthermore, the difference in results between our models underlines that it can make a significant difference if a constant or a strain-dependent permeability is included in a numerical model of a UHS in terms of liquid pressure, fault stability and storage capacity. This should be considered in future modelling work when a reservoir is aimed to be modelled in the most realistic way to have a good approximation for its storage capacity and risk of fault slip and caprock fracturing.

5.8 Model & Work limitations

It has to be considered that the reservoir in our model M1 was represented in a simplistic way. As it is not three-dimensional and does not include a spatially separated dual-permeability medium. Furthermore, the stress state was assumed and the character of the elastic fractures was just approximated as good as possible with the existing data. Also, the strong heterogeneity probably present at *Hontomín* (de Dios et al., 2017) was not possible to include. In addition, solubility and diffusivity under reservoir conditions for H_2 had to be approximated as they remain unknown. Therefore, our model M1 cannot finally resolve the question of wether *Hontomín* is suited for an UHS. Under our assumed and approximated circumstances, *Hontomín* could be used successfully as a small UHS structure. However, there still exists a great uncertainty for that. Though, our work showed that the reservoirs presented in our models inspired by the reservoir of *Hontomín* are in terms of geomechanical safeness suitable for a small UHS though, the reservoir with constant permeability is better suited.

The effect of the permeability type of the reservoir on storage capacity could be answered for our specific models that gave a good first hint on the relationship between both parameters in general. For further work it would be interesting to investigate this relation systematically changing the distance of the storage capacity limiting fault to the injection well, the dip angle of the present faults or their permeability systematically. It would also be interesting to discover the circumstances under which the storage capacity of a reservoir with constant permeability could be less than the storage capacity of a strain-dependent reservoir because of the presence of a far distant critically stressed fault.

Further models could include the strengths of our model and the model of de Dios et al. (2019) and Sohal et al. (2021). Such a model would be three-dimensional, representing the reservoir as spatially separated dual permeability medium (matrix & fractures), integrating the strain-dependent character of the fractures and including all detected faults and geomechanical coupling to enable a fault stability analysis.

6 Conclusion

The transformation of the energy sector to a more sustainable clean energy production is a key topic to combat climate change. Energy storage will be a key element in the future of renewable energy systems and will therefore become a topic of major importance. *Green hydrogen* produced from electrolysis of water seems to be a suitable energy carrier. However, as huge amounts of hydrogen will need to be stored in a cleaner energy industry, different storage possibilities have to be investigated. Underground hydrogen storage (UHS) of *green hydrogen* in geologic units seems to be a promising option to challenge this task. Though, this option is still in its infancy and a lot of aspects still remain unknown. Therefore, all different types of UHS structures, including their limitations, advantages and disadvantages, have to be investigated before deploying UHS technologies.

This work dealt with modelling an UHS operation in a carbonate aquifer. The main goal of this investigation was to find out the effect of the permeability type (constant vs. strain-dependent permeability) on the storage capacity of the reservoir formation. Therefore, two hydro-mechanical, numerical two-dimensional models were performed, differing in type of permeability (M1 = strain-dependent permeability; M2 = constant permeability). The models were inspired by the architecture and characteristics of the CO_2 pilot storage plant at Hontomìn (Spain). There, fluid flow in the naturally fractured reservoir is dominated by a fracture network whose permeability is strain-dependent. A consequent fault stability analysis was carried out and the amount of H_2 that was injected was chosen so that fault slip and fracturing of the caprock is inhibited.

Our work shows that the permeability type (strain-dependent vs. constant) can significantly affect the storage capacity of a reservoir during an UHS. In our specific models, the amount of H_2 that could be stored safely was around 46% higher in the reservoir with constant permeability (M2) than in the same reservoir but with strain-dependent permeability (M1). The strain-dependency of the permeability led to a relatively high permeability close to the injection and in the NE of the reservoir and a relatively low one far away from it, in this case decreasing mainly to the SW. The high increase in permeability in the NE occured because the low permeable E-fault led to relatively fast liquid pressure and thus permeability increase. The low permeability in the SW of model M1 worked as a semi barrier for fluid flow. Consequently, liquid pressure increased more in the central part and the NE of model M1 compared to model $M2_{low}$. The higher liquid pressure in model M1 led to a stronger decrease in the effective normal stress acting on the faults. Hence, this caused a stronger destabilization of these faults. This, in turn, resulted in a lower storativity of H_2 for model

M1 compared to model M2 as the risk of fault slip at X-2 was the limiting factor for the storage capacity in both models.

Thus, our hypothesis that there is no significant effect of the permeability type on storage capacity, resulting in both reservoir types having a similar storativity, needs to be rejected: a strong increase in liquid pressure was not compensated by an increased permeability in the strain-dependent reservoir of model M1. Therefore, the finding of Sohal et al. (2021), that pressure increase is inversely proportional to permeability in a reservoir with constant permeability cannot be applied to our model M1. Instead, permeability increased more around the injection well in model M1 than the constant permeability value of model M2, even though liquid pressure was higher in model M1.

At the same time, liquid pressure could spread more easily in model M2 as the constant permeability did not work as a barrier. Therefore, liquid pressure increased more in the SW of model $M2_{low}$ at far distant faults like the permeable S-fault than in model M1. This again resulted in a higher destabilization of the S-fault in model $M2_{low}$. Thus, while in a reservoir with strain-dependent permeability faults close to the injection point are under higher likelihood of slip, in a reservoir with constant permeability faults *far* away from the injection well are under higher likelihood of slip.

However, as liquid pressure rise decreased with increasing distance from the well, destabilization of the S-fault was lower than at the faults close to the well in both models. Thus, faults in a fractured reservoir with strain-dependent permeability should usually be more at risk to slip than in a porous reservoir with constant permeability. Furthermore, liquid pressure was higher in the caprock of model M1. This means that no matter if caprock fracturing or fault slip relatively close to the well is the limiting factor for the amount of storable H_2, a fractured reservoir has a lower storage capacity than a porous one.

Though, in a rare case, a lower storage capacity could be possible in a porous reservoir compared to a fractured reservoir. This could be the case when all faults close to the injection well are stable during the UHS but a far distant fault is critically stressed. The higher amount of liquid pressure at locations far away from the well in a porous reservoir could lead more easily to a slip of the far distant fault.

Thus, our conclusions cannot be generalized without exceptions but show that fractured reservoirs tend to have a lower storage capacity than porous ones. And further, that this capacity can significantly differ between the two reservoir types. However, how much the storage capacity differs between both reservoir types is site-specific and depends on the distance between the storage capacity limiting fault to the well. The closer this fault is, the more similar the storage capacity between both reservoir types.

Further modelling is needed to be done to determine the range of different storage capacities the two reservoir types could have. Within this future modelling, different settings (e.g. distance of storage capacity-limiting fault, caprock fracturing limit) should be compared systematically to each other to measure the effect of these settings on the storage capacity. Also, the model could be improved by being three-dimensional and having a spatial separation between fractures and matrix to represent the structure more realistically.

Our work showed that it is important to include all known faults as they can significantly limit the storage capacity. Furthermore, the large difference in storage capacity between both models underlines the strong sensibility of the permeability type on storage capacity. This sensibility should be taken into account for future modelling.

Another notable difference between our two models was their vertical displacement during the UHS. In general, model M1 had a slightly larger vertical displacement because of the higher liquid pressure in the reservoir. This larger vertical displacement led to a higher decrease in tangential stress. However, as the changes in tangential stress during the UHS were so low compared to the changes in normal stress, they played a minor role in the difference in fault stability between the two reservoir types.

A small advantage of the reservoir with strain-dependent permeability is the higher gas saturation of the gas plume. As liquid pressure and gas pressure are more hindered to spread because of the character of permeability distribution, the gas plume was around 4% more saturated with gas in model M1 than in model $M2_{low}$. This facilitates pumping out a high amount of gas during the withdrawn phase.

According to our results, both reservoir types also show some similarities during an UHS. Most instability at almost all faults occurred inside the reservoir, where liquid pressure increased the most in both models. The Mohr circle analysis detected that the reason for the change of mobilized friction during the UHS is the same for both reservoir types. In both models, a relatively strong decrease in effective horizontal stress and a stronger decrease in effective vertical stress took place inside the reservoir. Furthermore, the time when instability at each fault reached its maximum took place at the same time in both models. Maximum instability was reached just after the end of injection for faults close to the well and at the end of the resting phase for distant faults. This was because liquid pressure increased first around the injection well in the central part and NE and later diffused towards the SW. However, it is assumed that this behaviour originates from the site-specific geometry of the reservoir (e.g. strong offset at X-2). Also, the asymmetric plume spreading in SW direction is driven by the low-permeable E-fault in the NE, as already observed by Vilarrasa et al. (2016).

The fault X-2 was quite steep (dip angle of 62°) and was therefore already relatively strongly destabilized at the beginning of the UHS in both models. Additionally, as the fault was located at the largest offset of the reservoir and the caprock was relatively deformable, less horizontal and thus normal stress could accumulate at the upper part of the fault, as the caprock got relatively strong horizontally compressed. This resulted in a strong destabilization of the fault as Vilarassa et al. (2016) already observed, which could be proven again in this work. This result underlines that not only the permeability type of the reservoir but also the geometry (e.g., offset of the reservoir and dip angle of faults) and the stiffens of the caprock can have a huge influence on the storage capacity of an UHS. Furthermore, hints that the storage site at *Hontomín* is eventually not very well suited for an UHS because of the existence of a large offset in the reservoir. Yet, it is necessary to point out that too many parameters were estimated or approximated in the modelling. Therefore, the storage structure of *Hontomín* might not have been represented accurately to be realistic.

Aside from that, too many questions regarding an UHS in a saline aquifer remain unanswered- for instance how much cushion gas is needed and how much H_2 could be biodegraded by bacteria. However, *if* a UHS is planned in a saline aquifer, we recommend using one with a constant permeability, e.g., a porous reservoir, as our work indicates that the storage capacity should be generally higher than in a fractured one. Though, in terms of the urgency to combat climate change, we think it is essential to consider all possible options for a UHS and are open to adapt our recommendations if new study results advocate so.

Finally, to get an idea about how much storage potential the two storage structures according to our results have, the results from a calculation from Sáinz-García (2017) are presented here. The author calculated that the annual surplus energy of all windmills in *Castilla y León*, a leading region for wind power generation in Spain, could be converted into around 7247 tons of H_2. According to our results, a strain-dependent reservoir as at *Hontomín* could store just around 6.7 % of the surplus energy from windmills in *Castilla y León*. Instead, 9.8 % of this amount could be stored in the same reservoir but with constant permeability instead. Thus, both reservoir types would play a minor role in the UHS of this region but could still contribute a small part to reduce energy-related emissions. Therefore, this small step should be worth as it brings us closer to a future with less greenhouse gases. By this one day, we could rephrase the words of the Secretary-General of the United Nations António Guterres by saying, “At last, we are moving faster than climate change does".

7 Bibliography

Alcalde, J., Martí, D., Calahorrano, A., Marzan, I., Ayarza, P., Carbonell, R., Juhlin, C., & Pérez-Estaún, A. (2013). Active seismic characterization experiments of the Hontomín research facility for geological storage of CO2, Spain. International Journal of Greenhouse Gas Control, 19, 785–795. https://doi.org/10.1016/j.ijggc.2013.01.039

Alcalde, Juan, Marzán, I., Saura, E., Martí, D., Ayarza, P., Juhlin, C., Pérez-Estaún, A., & Carbonell, R. (2014). 3D geological characterization of the Hontomín CO2 storage site, Spain: Multidisciplinary approach from seismic, well-log and regional data. Tectonophysics, 627, 6–25. https://doi.org/10.1016/j.tecto.2014.04.025

Allen, M., Dube, O. P., Solecki, W., Aragón-Durand, F., Cramer, W., Humphreys, S., ... & Mulugetta, Y. (2018). Global warming of 1.5° C. An IPCC Special Report on the impacts of global warming of 1.5° C above pre-industrial levels and related global greenhouse gas emission pathways, in the context of strengthening the global response to the threat of climate change, sustainable development, and efforts to eradicate poverty. Sustainable Development, and Efforts to Eradicate Poverty.

Amid, A., Mignard, D., & Wilkinson, M. (2016). Seasonal storage of hydrogen in a depleted natural gas reservoir. International Journal of Hydrogen Energy, 41(12), 5549–5558. https://doi.org/10.1016/j.ijhydene.2016.02.036

Andersson, J., & Grönkvist, S. (2019). Large-scale storage of hydrogen. International Journal of Hydrogen Energy, 44(23), 11901–11919. https://doi.org/10.1016/j.ijhydene.2019.03.063

Andrés, J., Alcalde, J., Ayarza, P., Saura, E., Marzán, I., Martí, D., Catalán, J. R. M., Carbonell, R., Pérez-Estaún, A., Garića-Lobón, J. L., & Rubio, F. M. (2016). Basement structure of the Hontomín CO2storage site (Spain) determined by integration of microgravity and 3-D seismic data. Solid Earth, 7(3), 827–841. https://doi.org/10.5194/se-7-827-2016

Bachu, S. (2000). Sequestration of CO2 in geological media: Criteria and approach for site selection in response to climate change. Energy Conversion and Management, 41(9), 953–970. https://doi.org/10.1016/S0196-8904(99)00149-1

Bachu, S. (2015). Review of CO2 storage efficiency in deep saline aquifers. International Journal of Greenhouse Gas Control, 40, 188–202. https://doi.org/10.1016/j.ijggc.2015.01.007

Barton, C., Moos, D., & Tezuka, K. (2009). Geomechanical wellbore imaging: Implications for reservoir fracture permeability. AAPG Bulletin, 93(11), 1551–1569. https://doi.org/10.1306/06180909030

Birkholzer, J. T., Zhou, Q., & Tsang, C. F. (2009). Large-scale impact of CO2 storage in deep saline aquifers: A sensitivity study on pressure response in stratified systems. International Journal of

Greenhouse Gas Control, 3(2), 181–194. https://doi.org/10.1016/j.ijggc.2008.08.002

Carden, P. O., & Paterson, L. (1979). Physical, chemical and energy aspects of underground hydrogen storage. International Journal of Hydrogen Energy, 4(6), 559-569.

Hsieh, P. A., & Bredehoeft, J. D. (1981). A reservoir analysis of the Denver earthquakes A case of induced seismicity. 86, 903–920.

Cesca, S., Grigoli, F., Heimann, S., González, Á., Buforn, E., Maghsoudi, S., Blanch, E., & Dahm, T. (2014). The 2013 September-October seismic sequence offshore Spain: A case of seismicity triggered by gas injection? Geophysical Journal International, 198(2), 941–953. https://doi.org/10.1093/gji/ggu172

Crotogino, F., Donadei, S., Bünger, U., & Landinger, H. (2010). Large-Scale Hydrogen Underground Storage for Securing Future Energy Supplies. 18th World Hydrogen Energy Conference 2010 - WHEC 2010 Parallel Sessions Book 4: Storage Systems / Policy Perspectives, Initiatives and Co-Operations, 78, 10. https://core.ac.uk/download/pdf/34994534.pdf

Dávila, G., Luquot, L., Soler, J. M., & Cama, J. (2016). Interaction between a fractured marl caprock and CO2-rich sulfate solution under supercritical CO2 conditions. International Journal of Greenhouse Gas Control, 48, 105-119.

de Dios, J. C., Delgado, M. A., Martínez, C., Ramos, A., Álvarez, I., Marín, J. A., & Salvador, I. (2017). Hydraulic characterization of fractured carbonates for CO2 geological storage: Experiences and lessons learned in Hontomín Technology Development Plant. International Journal of Greenhouse Gas Control, 58, 185–200. https://doi.org/10.1016/j.ijggc.2017.01.008

de Dios, J. C., Le Gallo, Y., & Marín, J. A. (2019). Innovative CO2 injection strategies in carbonates and advanced modeling for numerical investigation. Fluids, 4(1). https://doi.org/10.3390/fluids4010052

de Dios, J. C., Mishra, S., & Poletto, F. (2021). CO2 Injection in the Network of Carbonate Fractures.

Deichmann, N., & Giardini, D. (2009). Earthquakes Induced by the stimulation of an enhanced geothermal system below Basel (Switzerland). Seismological Research Letters, 80(5), 784–798. https://doi.org/10.1785/gssrl.80.5.784

Ellsworth, W. L. (2013). Injection-Induced Earthquakes. 341(July), 1–8.

European Commission (2013). The future role and challenges of Energy Storage. DG ENER Working Paper, 2013.

Falzolgher, F., & Altieri, G. (2005). Underground storage of natural gas. Encyclopaedia of Hydrocarbons. Istituto Della Enciclopedia Italiana Fondata Da Giovanni Treccani. Marchesi Grafiche Editoriali S.p.A. 2005. 879-910

Fan, Z., Eichhubl, P., & Newell, P. (2019). Basement Fault Reactivation by Fluid Injection Into

Sedimentary Reservoirs: Poroelastic Effects. Journal of Geophysical Research: Solid Earth, 124(7), 7354–7369. https://doi.org/10.1029/2018JB017062

Fawzy, S., Osman, A. I., Doran, J., & Rooney, D. W. (2020). Strategies for mitigation of climate change: a review. Environmental Chemistry Letters, 18(6), 2069–2094. https://doi.org/10.1007/s10311-020-01059-w

Feldmann, F., Hagemann, B., Ganzer, L., & Panfilov, M. (2016). Numerical simulation of hydrodynamic and gas mixing processes in underground hydrogen storages. Environmental Earth Sciences, 75(16), 1–15. https://doi.org/10.1007/s12665-016-5948-z

Hangx, S., Spiers, C., & Peach, C. (2009). Energy Procedia The mechanical behavior of anhydrite and the effect of CO 2 injection. Energy Procedia, 1(1), 3485–3492. https://doi.org/10.1016/j.egypro.2009.02.140

Heide, D., Greiner, M., von Bremen, L., & Hoffmann, C. (2011). Reduced storage and balancing needs in a fully renewable European power system with excess wind and solar power generation. Renewable Energy, 36(9), 2515–2523. https://doi.org/10.1016/j.renene.2011.02.009

Heinemann, N., Alcalde, J., Miocic, J. M., Hangx, S. J. T., Kallmeyer, J., Ostertag-Henning, C., Hassanpouryouzband, A., Thaysen, E. M., Strobel, G. J., Schmidt-Hattenberger, C., Edlmann, K., Wilkinson, M., Bentham, M., Stuart Haszeldine, R., Carbonell, R., & Rudloff, A. (2021). Enabling large-scale hydrogen storage in porous media – the scientific challenges. Energy & Environmental Science. https://doi.org/10.1039/d0ee03536j

IEA (2019). The Future of Hydrogen. Seizing today´s opportunities. Report prepared by the IEA fot the G20, Japan.

Jaeger, J. C., Cook, N. G., & Zimmerman, R. (2009). Fundamentals of rock mechanics. Fourth Revised Edition. John Wiley & Sons.

Keranen, K. M., Savage, H. M., Abers, G. A., & Cochran, E. S. (2013). Potentially induced earthquakes in Oklahoma, USA: Links between wastewater injection and the 2011 Mw 5.7 earthquake sequence. Geology, 41(6), 699–702. https://doi.org/10.1130/G34045.1

King Hubbert, M., & Rubey, W. W. (1959). Role of Fluid Pressure in Mechanics of Overthrust Faulting. In *Geological Society of America Bulletin* (Vol. 70, Issue 2). https://doi.org/10.1130/0016-7606(1959)70[115:rofpim]2.0.co;2

Kruck, O., Crotogino, F., Prelicz, R., & Rudolph, T. (2013). Overview on all known underground storage technologies for hydrogen. Project HyUnder–Assessment of the Potential, the Actors and Relevant Business Cases for Large Scale and Seasonal Storage of Renewable Electricity by Hydrogen Underground Storage in Europe. Report D, 3.

Kovacs, T., Poulussen, D. F., & de Dios, C. (2015). Strategies for injection of CO2 into carbonate rocks at Hontomin. Global Carbon Capture and Storage Institute Ltd, Melbourne, Australia.

Le Gallo, Y., & de Dios, J. C. (2018). Geological model of a storage complex for a CO2 storage operation in a naturally-fractured carbonate formation. Geosciences (Switzerland), 8(9). https://doi.org/10.3390/geosciences8090354

Liu, W., Muhammad, N., Chen, J., Spiers, C. J., Peach, C. J., Deyi, J., & Li, Y. (2016). Investigation on the permeability characteristics of bedded salt rocks and the tightness of natural gas caverns in such formations. Journal of Natural Gas Science and Engineering. https://doi.org/10.1016/j.jngse.2016.07.072

Lord, A. S. (2009). Overview of geologic storage of natural gas with an emphasis on assessing the feasibility of storing hydrogen. 28. http://www.osti.gov/servlets/purl/975258-OsnNqC/

Metz, B., Davidson, O., De Coninck, H. C., Loos, M., & Meyer, L. (2005). IPCC special report on carbon dioxide capture and storage. Cambridge: Cambridge University Press.

Ogaya, X., Alcalde, J., Marzán, I., Ledo, J., Queralt, P., Marcuello, A., Martí, D., Saura, E., Carbonell, R., & Benjumea, B. (2016). Joint interpretation of magnetotelluric, seismic, and well-log data in Hontomín (Spain). Solid Earth, 7(3), 943–958. https://doi.org/10.5194/se-7-943-2016

Ogaya, X., Queralt, P., Ledo, J., Marcuello, Á., & Jones, A. G. (2014). Geoelectrical baseline model of the subsurface of the Hontomín site (Spain) for CO2 geological storage in a deep saline aquifer: A 3D magnetotelluric characterisation. International Journal of Greenhouse Gas Control, 27, 120–138. https://doi.org/10.1016/j.ijggc.2014.04.030

Olivella, S., Carrera, J., Gens, A., & Alonso, E. E. (1994). Nonisothermal Multiphase Flow of Brine and Gas Through Saline Media. 271–293.

Olivella, S., Gens, A., Carrera, J., & Alonso, E. E. (1996). Numerical formulation for a simulator (CODE _ BRIGHT) for the coupled analysis of saline media. 13(7), 87–112.

Ortiz, G., Kovacs, T., Poulussen, D. F., & De Dios, C. (2015) Hontomin reservoir characterisation test. Global Carbon Capture and Storage Institute Ltd, Melbourne, Australia.

Panfilov, M. (2016). Underground and pipeline hydrogen storage. In Compendium of Hydrogen Energy. Elsevier Ltd. https://doi.org/10.1016/b978-1-78242-362-1.00004-3

Panfilov, M. (2010). Underground Storage of Hydrogen: In Situ Self-Organisation and Methane Generation. Transport in Porous Media, 85(3), 841–865. https://doi.org/10.1007/s11242-010-9595-7

Paterson, L. (1983). The implications of fingering in underground hydrogen storage. International Journal of Hydrogen Energy, 8(1), 53–59. https://doi.org/10.1016/0360-3199(83)90035-6

Pérez-López, R., Mediato, J. F., Rodríguez-Pascua, M. A., Giner-Robles, J. L., Ramos, A., Martín-Velázquez, S., Martínez-Orío, R., & Fernández-Canteli, P. (2020). An active tectonic field for CO2 storage management: The Hontomín onshore case study (Spain). Solid Earth, 11(2), 719–739. https://doi.org/10.5194/se-11-719-2020

Pfeiffer, W. T., al Hagrey, S. A., Köhn, D., Rabbel, W., & Bauer, S. (2016). Porous media hydrogen storage at a synthetic, heterogeneous field site: numerical simulation of storage operation and geophysical monitoring. Environmental Earth Sciences, 75(16). https://doi.org/10.1007/s12665-016-5958-x

Plaat, H. (2009). Underground gas storage: Why and how. Geological Society Special Publication, 313, 25–37. https://doi.org/10.1144/SP313.4

Ruiz-Barajas, S., Sharma, N., Convertito, V., Zollo, A., & Benito, B. (2017). Temporal evolution of a seismic sequence induced by a gas injection in the Eastern coast of Spain. Scientific Reports, 7(1), 1–15. https://doi.org/10.1038/s41598-017-02773-2

Sáinz-García, A. (2017). Dynamics of underground gas storage. Insights from numerical models for carbon dioxide and hydrogen. 1–136. https://tel.archives-ouvertes.fr/tel-01703296

Shi, J. Q., Durucan, S., Korre, A., Ringrose, P., & Mathieson, A. (2019). History matching and pressure analysis with stress-dependent permeability using the In Salah CO2 storage case study. International Journal of Greenhouse Gas Control, 91(October), 102844. https://doi.org/10.1016/j.ijggc.2019.102844

Sohal, M. A., Le, Y., Audigane, P., Dios, J. C. De, & Rigby, S. P. (2021). International Journal of Greenhouse Gas Control Effect of geological heterogeneities on reservoir storage capacity and migration of CO 2 plume in a deep saline fractured carbonate aquifer. 108(March).

Steffen, W., Rockström, J., Richardson, K., Lenton, T. M., Folke, C., Liverman, D., Summerhayes, C. P., Barnosky, A. D., Cornell, S. E., Crucifix, M., Donges, J. F., Fetzer, I., Lade, S. J., Scheffer, M., Winkelmann, R., & Schellnhuber, H. J. (2018). Trajectories of the Earth System in the Anthropocene. Proceedings of the National Academy of Sciences of the United States of America, 115(33), 8252–8259. https://doi.org/10.1073/pnas.1810141115

Suckale, J. (2009). Induced Seismicity in Hydrocarbon Fields. Advances in Geophysics, 51(C), 55–106. https://doi.org/10.1016/S0065-2687(09)05107-3

Sunjay, S. (2019). P-28 Geological Storage : Underground Gas Storage Geological Storage : Underground Gas Storage. June, 8. https://www.researchgate.net/publication/333531452_P-28_Geological_Storage_Underground_Gas_Storage

Szulczewski, M. L., Macminn, C. W., Herzog, H. J., & Juanes, R. (2012). Lifetime of carbon capture and storage as a climate-change mitigation technology. https://doi.org/10.1073/pnas.1115347109

Tarkowski, R. (2019). Underground hydrogen storage: Characteristics and prospects. Renewable and Sustainable Energy Reviews, 105(February 2017), 86–94. https://doi.org/10.1016/j.rser.2019.01.051

Tavani, S. (2012). Plate kinematics in the Cantabrian domain of the Pyrenean orogen. Solid Earth, 3(2), 265–292. https://doi.org/10.5194/se-3-265-2012

Tavani, S., Quintà, A., & Granado, P. (2011). Cenozoic right-lateral wrench tectonics in the Western Pyrenees (Spain): The Ubierna Fault System. Tectonophysics, 509(3–4), 238–253.

https://doi.org/10.1016/j.tecto.2011.06.013

Thaysen, E. M., McMahon, S., Strobel, G., Butler, I., Ngwenya, B., Wilkinson, M., Hassanpouryouzband, A., & McDermott, C. (2020). Estimating Microbial Hydrogen Consumption in Hydrogen Storage in Porous Media as a Basis for Site Selection. 1–61.

Oldenburg, C. M. (2012). The risk of induced seismicity: Is cap-rock integrity on shaky ground?. Earth Sciences Division, LBNL A recent. (n.d.). 1–4.

Tollefson, J. (2018). Clock ticking on climate action. Nature, 562(7726), 172–173. http://www.nature.com/articles/d41586-018-06876-2

Torabi, A., Johannessen, M. U., & Ellingsen, T. S. S. (2019). Fault Core Thickness : Insights from Siliciclastic and Carbonate Rocks. 2019.

ul Abedin, M. Z. (2015). Gas penetration or blocking processes in clay cap-rock of underground gas storage (UGS). https://doi.org/10.3997/2214-4609.201412495

van Renssen, S. (2020). The hydrogen solution? Nature Climate Change, 10(9), 799–801. https://doi.org/10.1038/s41558-020-0891-0

Vera, J. A., Ancochea, E., Barnolas, A., Bea, F., Calvo, J.P., Civis, J., De Vicente, G., Fernández-Gianotti, J., Garc.a-Cort.s, A., Pérez-Estaún, A., Pujalte, V., Rodríguez-Fernández, L.R., Sopeña, A., & Tejero, R. (2004) Introducción. Geología de España.

Verdon, J. P., & Stork, A. L. (2016). Carbon capture and storage, geomechanics and induced seismic activity. Journal of Rock Mechanics and Geotechnical Engineering, 8(6), 928–935. https://doi.org/10.1016/j.jrmge.2016.06.004

Vilarrasa, V., Bolster, D., Olivella, S., & Carrera, J. (2010). Coupled hydromechanical modeling of CO2 sequestration in deep saline aquifers. International Journal of Greenhouse Gas Control, 4(6), 910–919. https://doi.org/10.1016/j.ijggc.2010.06.006

Vilarrasa, V., & Carrera, J. (2015). Geologic carbon storage is unlikely to trigger large earthquakes and reactivate faults through which CO2 could leak. Proceedings of the National Academy of Sciences of the United States of America, 112(19), 5938–5943. https://doi.org/10.1073/pnas.1413284112

Vilarrasa, V., Carrera, J., Olivella, S., Rutqvist, J., & Laloui, L. (2019). Induced seismicity in geologic carbon storage. Solid Earth, 10(3), 871–892. https://doi.org/10.5194/se-10-871-2019

Vilarrasa, V., Makhnenko, R., & Gheibi, S. (2016). Geomechanical analysis of the influence of CO2 injection location on fault stability. Journal of Rock Mechanics and Geotechnical Engineering, 8(6), 805–818. https://doi.org/10.1016/j.jrmge.2016.06.006

Vilarrasa, V., Makhnenko, R. Y., & Laloui, L. (2017). Potential for Fault Reactivation Due to CO2 Injection in a Semi-Closed Saline Aquifer. Energy Procedia, 114(November 2016), 3282–3290. https://doi.org/10.1016/j.egypro.2017.03.1460

Vilarrasa, V., Silva, O., Carrera, J., & Olivella, S. (2013). Liquid CO2 injection for geological storage in deep saline aquifers. International Journal of Greenhouse Gas Control, 14, 84–96. https://doi.org/10.1016/j.ijggc.2013.01.015

ITTC Specialist Committee. (2011). ITTC–Recommended Procedures Fresh Water and Seawater Properties. IITC.

Wu, H., Vilarrasa, V., De Simone, S., Saaltink, M., & Parisio, F. (2021). Analytical Solution to Assess the Induced Seismicity Potential of Faults in Pressurized and Depleted Reservoirs. Journal of Geophysical Research: Solid Earth, 126(1). https://doi.org/10.1029/2020JB020436

Yamamoto, S., Miyoshi, S., Sato, S., & Suzuki, K. (2013). Study on geomechanical stability of the aquifer-caprock system during CO2 sequestration by coupled hydromechanical modeling. Energy Procedia, 37, 3989–3996. https://doi.org/10.1016/j.egypro.2013.06.298

Yan-Lin, Z., & Wen, W. (2014). Mechanical Properties of Bedded Rock Salt. 9347–9353.

Ziparo, C., Giannasi, A., Ulivi, L., & Zoppi, M. (2011). Raman spectroscopy study of molecular hydrogen solubility in water at high pressure. International Journal of Hydrogen Energy, 36(13), 7951–7955. https://doi.org/10.1016/j.ijhydene.2011.01.178

Zoback, M. D. (2007). Reservoir geomechanics. Cambridge university press.

Zoback, M. D., & Gorelick, S. M. (2012). Earthquake triggering and large-scale geologic storage of carbon dioxide. Proceedings of the National Academy of Sciences of the United States of America, 109(26), 10164–10168. https://doi.org/10.1073/pnas.1202473109

Further Sources

https://www.danaenergy.com/en/media-menu/dana-magazine/conversations/underground-gas-storage

https://ourworldindata.org/renewable-energy

http://naturalgas.org/naturalgas/storage/

https://www.aqua-calc.com/page/density-table/substance/salt

https://www.engineeringtoolbox.com/gases-absolute-dynamic-viscosity-d_1888.html

8 Appendix

Table 1 Derived fault thicknesses from the faults offset. Note the thickness of the S-fault was set to a similar value as the E-fault as both are probably deep faults reaching the basement. It was assumed that the small offset does not correlate with the thickness of the S-fault. At the fault inversion correction calculated thickness was just multiplied by 1.25 as due to fault inversion, the offset could have been bigger than today.

	Offset measured	Thickness calculated	Fault inversion correction	Thickness rounded
E-fault	377	17,51	26,27	26
N-2	21,5	1,53	1,92	2
X-2	80	4,69	5,86	6
N-1	50	3,15	3,93	4
X-1	30	2,04	2,55	3
S-fault	37	2,43	3,04	20

Table 5 Used parameters for model convergence

Epsilon	1
Theta	1
Time step control	6
Max Number of Iterations per time step	20
Solver type	Iterative Sparse + CGS
Max number of solver iterations	5000
Max abs solver error variable	$1 \cdot 10^{-9}$
Max abs solver error residual	0
Max rel solver error residual	0
Elemental relative permeability computed from	Average nodal degree of saturation
Max Abs Displacement [m]	$1 \cdot 10^{-5}$
Max Nod Bal Forces [MN]	$1 \cdot 10^{-9}$
Displacement Iter Corr [m]	1
Max Abs Pl [Mpa]	$1 \cdot 10^{-2}$
Max Nod Water Mass Bal [kg/s]	$1 \cdot 10^{-9}$
Pl Iter Corr [Mpa]	4
Max Abs Pg [Mpa]	$1 \cdot 10^{-2}$

Max Nod Air Mass Bal [kg/s]	$1 \cdot 10^{-9}$
Pg Iter Corr [Mpa]	4
Convergence criterion	On nodal correction or residual

Table 6 Used time steps for model convergence

Initial Time Step	0.001
Maximum Time Step	0.05

Table 7 Used mesh sizes for model convergence

Mesh Size Reservoir [m]	10
Mesh Size all other Units [m]	20